

**ON THE DYNAMICS OF RAYLEIGH-TAYLOR MIXING**

A Dissertation

by

PRAVEEN KUMAR RAMAPRABHU

Submitted to the Office of Graduate Studies of  
Texas A&M University  
in partial fulfillment of the requirements for the degree of

DOCTOR OF PHILOSOPHY

December 2003

Major Subject: Mechanical Engineering

**ON THE DYNAMICS OF RAYLEIGH-TAYLOR MIXING**

A Dissertation

by

PRAVEEN KUMAR RAMAPRABHU

Submitted to Texas A&M University  
in partial fulfillment of the requirements  
for the degree of

DOCTOR OF PHILOSOPHY

Approved as to style and content by:

---

Malcolm J. Andrews  
(Chair of Committee)

---

Junuthula N. Reddy  
(Member)

---

Sharath S. Girimaji  
(Member)

---

Denis Phares  
(Member)

---

Dennis L. O'Neal  
(Head of Department)

December 2003

Major Subject: Mechanical Engineering

**ABSTRACT**

On the Dynamics of Rayleigh-Taylor Mixing.

(December 2003)

Praveen Kumar Ramaprabhu, B.S., Anna University;

M.S., University of Houston

Chair of Advisory Committee: Dr. Malcolm J. Andrews

The self-similar evolution of a turbulent Rayleigh-Taylor (R-T) mix is investigated through experiments and numerical simulations. The experiments consisted of velocity and density measurements using thermocouples and Particle Image Velocimetry techniques. A novel experimental technique, termed PIV-S, to simultaneously measure both velocity and density fields was developed. These measurements provided data for turbulent correlations, power spectra, and energy balance analyses. The self-similarity of the flow is demonstrated through velocity profiles that collapse when normalized by an appropriate similarity variable and power spectra that evolve in a shape-preserving form. In the self-similar regime, vertical r.m.s. velocities dominate over the horizontal r.m.s. velocities with a ratio of 2:1. This anisotropy, also observed in the velocity spectra, extends to the Taylor scales. Buoyancy forcing does not alter the structure of the density spectra, which are seen to have an inertial range with a  $-5/3$  slope. A scaling analysis was performed to explain this behavior. Centerline velocity fluctuations drive the growth of the flow, and can hence be used to deduce the growth constant. The question of universality of this flow was addressed through 3D numerical simulations with carefully

designed initial conditions. With long wavelengths present in the initial conditions, the growth constant was found to depend logarithmically on the initial amplitudes. In the opposite limit, where long wavelengths are generated purely by the nonlinear interaction of shorter wavelengths, the growth constant assumed a universal lower bound value of 0.03. Small-scale features of the flow such as molecular mixing and kinetic energy dissipation were found independent of the initial conditions. Numerical simulations initialized with experimentally obtained velocity and density data were also performed. Calculations initialized with velocity data compared better with experimental results than those initialized with density data. Due to the presence of high-amplitude long wavelengths in the simulations, and assumptions about the isotropy of the initial velocity fluctuations, the late time growth differed from the experiments. More experiments that accurately capture the three-dimensional velocity field at the start are needed.

*To Professor K. Rajagopalan*

## ACKNOWLEDGEMENTS

I would like to thank my research advisor and committee chairman, Malcolm J. Andrews, for his advice, guidance and support during the course of this work. Also, many thanks to Guy Dimonte at the Los Alamos National Laboratory for his insights and guidance. I wish to acknowledge Wayne Kraft and Nick Mueschke for their help, and encouragement. I have enjoyed the many discussions I have had with them on and off the subject of Rayleigh-Taylor instabilities.

This work was funded by the Department of Energy, research grants # DE-FG013-99DP00276/A000 and DE-FG03-02NA00060.

## TABLE OF CONTENTS

	Page
ABSTRACT.....	iii
DEDICATION.....	v
ACKNOWLEDGEMENTS.....	vi
TABLE OF CONTENTS.....	vii
LIST OF FIGURES.....	ix
LIST OF TABLES .....	xvi
1. INTRODUCTION .....	1
1.1 Overview .....	1
1.2 Background .....	4
2. EXPERIMENTAL SETUP AND DIAGNOSTICS .....	17
2.1 Preliminaries .....	17
2.2 PIV System .....	21
2.3 Thermocouple System .....	23
3. SIMULTANEOUS MEASUREMENTS OF VELOCITY AND DENSITY FIELDS (THE PIV-S METHOD) .....	28
3.1 Preliminaries .....	28
3.2 Density Measurements .....	31
3.3 Velocity Measurements .....	40
3.4 Velocity-Density Correlations .....	44
3.5 Error Analysis .....	45
4. EXPERIMENTAL RESULTS .....	51
4.1 Preliminaries .....	51
4.2 Statistics .....	66
4.3 Spectra .....	76

	Page
4.4 Taylor Microscales .....	91
4.5 Energy Budget .....	95
5. NUMERICAL TECHNIQUE .....	99
5.1 Preliminaries .....	99
5.2 Estimation of Numerical Viscosity: Single-mode Calculations .....	103
5.3 Determination of $c_\infty$ : Single-mode Calculations .....	105
6. EFFECT OF INITIAL CONDITIONS ON R-T GROWTH .....	111
6.1 Introduction .....	111
6.2 Multi-mode Calculations.....	115
6.3 Effect of Initial Amplitudes .....	136
6.4 Mode Coupling .....	141
6.5 Effect of Spectral Index .....	145
7. NUMERICAL SIMULATIONS OF WATER CHANNEL EXPERIMENTS ...	153
7.1 Formulation of Initial Conditions .....	153
7.2 Density Perturbations .....	160
7.3 Velocity Perturbations .....	162
8. CONCLUSIONS .....	167
REFERENCES .....	172
APPENDIX A .....	182
APPENDIX B .....	186
APPENDIX C .....	191
APPENDIX D .....	200
APPENDIX E.....	203
VITA .....	206



## LIST OF FIGURES

FIGURE	Page
1.1 Stages of evolution of R-T instability .....	6
1.2 Planar Laser Induced Fluorescence (PLIF) images at (a) early and (b) late times of evolution of the R-T instability .....	7
2.1 Schematic of experimental setup .....	18
2.2 Mean velocity profiles at $x = 1$ cm (a) and $x = 2$ cm (b) .....	20
3.1 $f_1$ profiles at (a) $x = 2.5$ cm, and (b) $x = 35$ cm from PIV-S and thermocouple experiments (dotted line represents centerline of mix) .....	32
3.2 $B_0$ and $B_2$ profiles at (a) $x = 2.5$ cm, and (b) $x = 25$ cm from PIV-S and thermocouple experiments .....	35
3.3 $\theta$ across the mixing layer at (a) $x = 2.5$ cm, and (b) $x = 35$ cm from PIV-S and thermocouple experiments .....	37
3.4 Contour map of $B_0$ at $x = 2.5$ cm from the splitter plate .....	38
3.5 (a) and (b) Two successive particle images showing mushroom-shaped structures characteristic of R-T instability. Velocity vector field (c), and vorticity field (d) obtained by cross-correlating the image files of (a) and (b) .....	39
3.6 R.M.S. profiles of $u$ and $v$ velocity components at (a) $x = 2.5$ cm, and (b) $x = 35$ cm from PIV-S and PIV .....	43
3.7 Contour map of $v_{rms}/u_\infty$ at $x = 2.5$ cm .....	44
3.8 Profiles of, $\langle \rho'u' \rangle / \Delta\rho u_\infty$ and $\langle \rho'v' \rangle / \Delta\rho u_\infty$ at (a) $x \sim 2.5$ cm downstream, (b) $x \sim 35$ cm .....	46
3.9 % r.m.s. Error as a function of number of samples .....	47
3.10 Average intensity within an interrogation window as a function of the window size in pixels .....	50

FIGURE	Page
3.11 Molecular mix fraction $\theta$ as a function of the window size in pixels .....	50
4.1 Time evolution of scalar turbulence intensity and mix parameters measured at the centerline .....	55
4.2 p.d.f.s of centerline non-dimensional density at 3 different times .....	57
4.3 (a) Intermittency factor $\gamma_\omega$ (based on a vorticity threshold) and (b) Intermittency factor (based on the two-fluid parameter $B_2$ ) across the mix at $T = 1.21$ .....	58
4.4 p.d.f.s of vertical and horizontal velocities at three locations across the mix. (a) $\frac{v'}{v'_{max}} = 1$ , (b) $\frac{v'}{v'_{max}} = 0.5$ , (c) $\frac{v'}{v'_{max}} = 0.2$ corresponding to $y/H = 0, 0.13,$ and $0.2$ respectively ( $T = 1.21$ ) .....	61
4.5 Skewness (a) and Kurtosis (b) profiles across the mix at $T = 1.21$ .....	63
4.6 Centerline vertical and horizontal velocity r.m.s. as a function of non-dimensional time .....	65
4.7 (a). $\alpha = v' / 2A_t g t$ at the centerline plotted as a function of $T$ and (b) $l_m = v'^2 / 0.7^2 A_t g / 2$ in cm at the centerline plotted as a function of $T$ . Inset shows $l_m$ close to the splitter plate .....	68
4.8 (a) $u'$ profiles at different $T$ – locations. (b) $v'$ profiles at different $T$ -locations .....	70
4.9 (a) $u'$ profiles at different $T$ – locations expressed in self-similar units and (b) $v'$ profiles at different $T$ – locations expressed in self-similar units .....	72
4.10 Ratio of $v'/u'$ across the mix at $T = 1.21$ .....	73
4.11 Profiles of the anisotropy tensor across the mix at (a) $T = 0.07$ , and (b) $T = 1.21$ .....	74

FIGURE	Page
4.12 Density fluctuation spectrum (a) at $T = 0.034$ at the centerline. Dashed line represents $kH = 20$ . (b) Compensated fluctuation spectrum $k^4 E(k)$ . Solid line represents the horizontal .....	77
4.13 Frequency velocity spectra at $T = 0.07$ at the centerline. The dashed line represents $kH \sim 20$ .....	78
4.14 (a) Centerline density fluctuation spectrum $E(k)$ at $T = 1.008$ and compensated fluctuation spectra $k^m E(k)$ where (b) $m = 5/3$ , (c) $m = 3$ , and (d) $m = 5$ . Solid line represents the horizontal .....	79
4.15 (a) Centerline density fluctuation spectrum $E(k)$ at $T = 2.08$ and compensated fluctuation spectra $k^m E(k)$ where (b) $m = 5/3$ , (c) $m = 3$ , and (d) $m = 5$ . Solid line represents the horizontal .....	80
4.16 Frequency velocity spectra at the centerline at $T = 1.21$ (a) Raw spectra and (b) spectra smoothed using a window-averaging process .....	83
4.17 Spectra of total kinetic energy $E(k)$ , Production $P(k)$ , Dissipation $D(k)$ , and Transfer $T(k)$ at $T = 1.21$ at the centerline .....	84
4.18 Velocity field from fig. 3.5 (c) processed through iterative-PIV technique .....	86
4.19 Wavenumber velocity spectra at the centerline at (a) $T = 0.07$ and (b) $T = 1.21$ .....	88
4.20 Time evolution of exponential curve-fit index, $p$ for centerline temperature measurements .....	90
4.21 Spectra of $S/s(k)$ showing tendency toward isotropy at higher wavenumbers for the centerline velocity spectra .....	94
5.1 2D slice of computational domain used in numerical simulations: $\rho_1 = 1$ g/cc, and $\rho_2 = 3$ g/cc .....	102
5.2 (a) Bubble amplitude evolution from the single-mode calculations at different resolutions. (b) The non-dimensional exponential growth-rate as a function of the resolution .....	106

FIGURE	Page
5.3 Contour map of volume fraction $f_l(x,z)$ at $t = 0$ for the single-mode calculations .....	107
5.4 (a), (b) and (c) showing the evolution of single-mode perturbations at $A_t g t^2 = 0.1, 0.4,$ and $0.7$ m respectively. Shown are the iso-surfaces of $f_l=0.5$ .....	108
5.5 Evolution of bubble amplitude $h$ (m) plotted as a function of time (s) .....	108
5.6 Evolution of the terminal velocity $v_\infty$ (a) and the dimensionless constant $c_\infty$ (b) for a 3D R-T bubble at $A_t=0.001$ .....	110
6.1 Initial perturbations for simulation 6 in (a) physical and (b) wavenumber space. (c) Initial perturbations as a function of the mode number, $n$ . Dotted line elucidates the $k^{-2}$ structure .....	117
6.2 Initial perturbations for simulation 11 in (a) physical and (b) wavenumber space. (c) Initial perturbations as a function of the mode number, $n$ showing energy between $n = 16$ and $32$ .....	119
6.3 Evolution of bubble and spike amplitudes ( $h_b$ and $h_s$ ), and integral width $W$ for case 6 .....	121
6.4 Iso-surfaces of 1% of volume-fraction $f_l$ from simulation 11 at $A_t g t^2 = 1$ (a), 10 (b), and 19 (c) .....	125
6.5 Bubble fronts $Z_b(x,z)$ from simulation 6 at early-, mid- and late times ( $A_t g t^2 = 2, 8,$ and $16$ ) .....	126
6.6 Azimuthally averaged power spectra of bubble fronts $Z_b(x,z)$ from simulation 6 at early-, mid-, and late times ( $A_t g t^2 = 2, 8,$ and $16$ ) .....	127
6.7 (a) Test image of radius 20 pixels with a parabolic (b) intensity profile. (c) Autocorrelation contours of test image from (a) and the azimuthally averaged radial profile (d) showing a radius of 20 pixels .....	128
6.8 (a) Bubble front image $Z_b(x,z)$ from simulation 11 at $A_t g t^2 = 22$ . (b) Autocorrelation contours of the bubble front field from (a) and the azimuthally averaged radial profile (c) .....	130

FIGURE	Page
6.9 Vertical slice of density contours from simulation 6 at $A_1gt^2 = 17$ . The average bubble density and velocities are computed within the volume enclosed by the leading bubble tip and the dashed line .....	131
6.10 Histogram of Froude numbers from the 12 simulations .....	133
6.11 Effect of $k\langle h_{0k} \rangle$ : (a) Evolution of bubble amplitude, $h_b$ for cases 6,7, and 8 ( $k\langle h_{0k} \rangle = 0.0044, 0.0003, \text{ and } 3 \times 10^{-6}$ ) (b) Evolution of $\alpha_b$ for cases 6,7, and 8 ( $k\langle h_{0k} \rangle = 0.0044, 0.0003, \text{ and } 3 \times 10^{-6}$ ) .....	134
6.12 Effect of $k\langle h_{0k} \rangle$ : (a) Evolution of bubble wavelength, $\lambda_b$ for cases 6,7, and 8 ( $k\langle h_{0k} \rangle = 0.0044, 0.0003, \text{ and } 3 \times 10^{-6}$ ) scaled to $\lambda_p$ . (b) Evolution of $\beta_b$ for cases 6,7, and 8 ( $k\langle h_{0k} \rangle = 0.0044, 0.0003, \text{ and } 3 \times 10^{-6}$ ) .....	135
6.13 Effect of $k\langle h_{0k} \rangle$ : (a) Evolution of molecular mix fraction $\Theta$ for cases 6,7, and 8 ( $k\langle h_{0k} \rangle = 0.0044, 0.0003, \text{ and } 3 \times 10^{-6}$ ). (b) Evolution of $KE/\Delta P.E.$ for cases 6, 7, and 8 .....	140
6.14 Comparison of $\alpha_b$ from the model and DNS. Open circles show insensitivity of the mode-coupling cases to the initial amplitudes .....	142
6.15 Comparison of $\beta_b$ from the model and DNS. Open circles show insensitivity of the mode-coupling cases to the initial amplitudes .....	142
6.16 Molecular mix fraction $\Theta$ vs. $k\langle h_{0k} \rangle$ .....	144
6.17 Kinetic energy as a fraction of potential energy released vs. $k\langle h_{0k} \rangle$ .....	144
6.18 Effect of $p$ : (a) Evolution of bubble amplitude, $h_b$ for cases 6,9, and 10 ( $p = -2, 0, \text{ and } -1$ ). (b) Evolution of $\alpha_b$ for cases 6,9, and 10 ( $p = -2, 0, \text{ and } -1$ ) .....	146
6.19 Effect of $p$ (a) Evolution of $\lambda_b$ for cases 6,9, and 10 ( $p = -2, 0, \text{ and } -1$ ) scaled to $\lambda_p$ . (b) Evolution of $\beta_b$ for cases 6,9, and 10 ( $p = -2, 0, \text{ and } -1$ ) ....	147
6.20 $\alpha_b$ vs. $p$ for cases 6,9, and 10 ( $p = -2, 0, \text{ and } -1$ ) .....	149

FIGURE	Page
6.21 $\beta_b$ vs. $p$ for cases 6,9, and 10 ( $p = -2, 0,$ and $-1$ ) .....	149
6.22 (a). Contours of volume fraction $f_l$ on a horizontal plane at $y=0$ .(from case 11) at $A_t g t^2=22$ . (b) Azimuthally averaged power spectra of $f_l$ for the two mode-coupling cases 11 and 12 .....	151
6.23 Azimuthally averaged power spectra of $f_l$ from the initial amplitude study (a) and spectral index study (b) .....	152
7.1 Spectra of density initial conditions from the simulations (case 3) and the experiment (thermocouple measurements) .....	156
7.2 Spectra of velocity initial conditions from simulation 4 and the experiment (PIV measurements) .....	157
7.3 Contours of volume fraction $f_l$ from case 2 at $A_t g t^2 = 0$ (a) and $A_t g t^2=3$ (b) at the interface ( $y = 0$ ) .....	158
7.4 Evolution of amplitudes (of bubble) from cases 1,2, and 3 .....	159
7.5 Comparison of r.m.s. of vertical velocity fluctuations (a) and the growth constant $\alpha$ (b) from simulations initialized with density and the experiment .....	161
7.6 Comparison of r.m.s. of vertical velocity fluctuations (a) and the growth constant $\alpha$ (b) from simulation 4 and the experiment .....	163
7.7 Comparison of molecular mix fraction $\theta$ from simulation 4 and thermocouple measurements .....	165
A.1 (a) PIV image with no temperature difference and (b) PIV image with a $5^\circ$ temperature difference .....	184
A.2 (a) Stationary objected illuminated by laser sheet in an unstably stratified mixing layer. (b) Profiles of $u'$ along the dotted line in (a) .....	185
B.1 Comparison of $k$ - profiles from experiment and similarity analysis .....	190
B.2 Comparison of volume fraction profiles from experiment and similarity analysis .....	190

FIGURE	Page
C.1 Evolution of the integral mix-width $W$ from the numerical simulations as a function of (a) $Ag\tau^2$ , and (b) $Ag\tau^2/\lambda_p$ .....	194
C.2 Evolution of the bubble amplitude $h_b$ from the numerical simulations as a function of (a) $Ag\tau^2$ , and (b) $Ag\tau^2/\lambda_p$ .....	195
C.3 Evolution of the growth constant $\alpha_b$ from the numerical simulations as a function of (a) $Ag\tau^2$ , and (b) $Ag\tau^2/\lambda_p$ .....	196
C.4 Power spectra of density fluctuations from the numerical simulations at (a) $Ag\tau^2 = 5$ , and (b) $Ag\tau^2=22$ .....	198

## LIST OF TABLES

TABLE	Page
2.1 Reynolds number definitions for R-T flow .....	27
4.1 List of thermocouple and PIV/PIV-S experiments .....	52
6.1 List of simulations .....	116
6.2 The nonlinear transition time $A_i g t_k^2$ for the 12 simulations .....	123
6.3 Times at which mode-coupling begins for the 12 simulations .....	123
6.4 The effective Froude numbers from the simulations .....	132
6.5 Self-similar parameters $\alpha_b$ , and $\beta_b$ from the simulations .....	137
6.6 Molecular mixing parameter $\Theta$ and $K.E./\Delta P.E.$ from the simulations .....	139
7.1 List of simulations initialized with experimental conditions .....	154
C.1 List of RTI codes .....	191
C.2 Viscosities of the RT codes .....	193
C.3 Bubble growth constant $\alpha_b$ from the simulations .....	197



## 1. INTRODUCTION

### *1.1 Overview*

The self-similar evolution of a turbulent Rayleigh-Taylor (R-T) mix has been studied experimentally and through numerical simulations. The objectives of this study were to (a) understand the dynamics of the self-similar R-T mix through experiments, (b) numerically study the role played by initial conditions on the late-time growth of the flow, and (c) to perform numerical simulations using experimental initial conditions. This would allow numerical experiments under conditions that cannot be implemented experimentally. The experiments were conducted at the water channel facility at Texas A&M University (Snider and Andrews 1994), and involved density measurements, velocity measurements, and simultaneous measurements of both using a novel technique. These measurements have provided insight in to the nature of turbulent R-T mixing at low density differences. The simulations used a 3D, finite-volume code developed by Andrews (1995) that solved the Euler equations with an artificial numerical viscosity. The experimental and numerical methods used, and the major findings of this work are summarized below.

The velocity measurements were performed using the Particle Image Velocimetry (PIV) technique, while temperature fluctuations were measured using a thermocouple system. In this experiment, the density difference was achieved through a temperature difference in the fluid. Cold fluid enters above the hot in a closed channel to form an unstable

---

This dissertation follows the style and format of the *Journal of Fluid Mechanics*.

interface. This buoyancy driven mixing experiment allows for long data collection times, short transients, and is statistically steady. First, second, and third order statistics with spectra of velocity and temperature fields were collected. Analysis of the measurements has shed light on the structure of mixing as it develops to a self-similar regime in this flow. The onset of self-similarity is marked by the development of a self-preserving form of the temperature spectra, and the collapse of velocity profiles expressed in self-similar units. Vertical velocity fluctuations dominate horizontal velocity fluctuations in this experiment, with a ratio approaching 2:1 in the self-similar regime. This anisotropy extends to the Taylor microscales that undergo differential straining in the direction of gravity. Up to two decades of velocity spectra development, and four decades of temperature spectra, were captured from the experiment. The velocity spectra consist of an inertial range comprised of anisotropic vertical and horizontal velocity fluctuations, and a more isotropic dissipative range. Buoyancy forcing occurs across the spectrum of velocity and temperature scales, but was not found to affect the structure of the spectra, resulting in a  $-5/3$  slope, similar to other canonical turbulent flows. A scaling argument is presented to explain this observation. The net kinetic energy dissipation as the flow evolves from an initial state to a final self-similar state, was measured to be 49% of the accompanying loss in potential energy, in close agreement with values obtained from 3D numerical simulations.

Using 3D numerical simulations, a model for the role of initial conditions in R-T was verified. A finite-volume, Eulerian solver with Van Leer flux limiters was used with a

resolution of 128x128x256 grid points in the  $x$ -,  $z$ - and  $y$ -directions respectively, where  $y$ - is the direction of the gravity vector. The initial conditions were chosen to test the dependence of R-T growth constants on (i) the amplitude, (ii) spectral shapes, and (iii) coupling of wavelengths. In agreement with the model, the growth constant was found to depend logarithmically on the initial amplitudes (and the Froude number). In the opposite limit, where long wavelengths are generated purely by nonlinear interaction (mode-coupling), no such dependence on initial amplitudes was observed. Small-scale effects such as molecular mixing and kinetic energy dissipation showed little dependence on the structure of initial conditions.

Finally, simulations initialized with data obtained from our experiments were also performed. The box dimensions, density difference, and other parameters were chosen to match the experimental conditions. The experimental initial conditions recorded as single-point density and velocity data, were then projected on to a 2D-wavenumber space. Calculations were initialized with velocity fluctuations, and density fluctuations – the virtues and drawbacks of each method were explored. Furthermore, the effect of long wavelengths present in the experiment was also studied. The velocity and density statistics, spectra, the growth constant  $\alpha$ , and the molecular mix fraction  $\theta$  obtained from the simulations were compared with corresponding experimental values.

## 1.2 Background

Rayleigh-Taylor (R-T) instability is induced when a density gradient is accelerated, in the presence of infinitesimal perturbations, by a pressure gradient in the opposite direction such that  $\nabla p \bullet \nabla \rho < 0$  (Chandrasekhar 1961). If the initial density interface comprises a spectrum of velocity and/or density disturbances, then the pressure gradient drives the growth of the perturbation to form a mix region whose width grows in time. Development of the mix was divided by Youngs (1984) into three successive regimes: 1) initially an exponential growth of infinitesimal perturbations that correspond to linear stability analysis; 2) at about amplitudes one-half of the wavelength, the instability saturates and the perturbation speed grows at a constant rate; and 3) thereafter, longer wavelengths overtake due to their continuing exponential growth. Emmons, Chang & Watson (1960) coined the term '*bubble competition*' to describe this last regime. Eventually, through mode interaction and successive wavelength saturation, a self-

similar R-T mix layer is formed (figure 1.1). To illustrate the mixing process, figure 1.2 shows Planar Laser Induced Fluorescence (PLIF) photographs taken from the experiment described herein. The fluid is water, with the top layer at a temperature of 17°C and the bottom layer at 22°C, and the flow direction is from left to right. The temperature difference provides a corresponding small density difference due to thermal expansion. Inspection of the photographs reveals that at early times (figure 1.2(a)), two-dimensional, single-wavelength perturbations can be seen growing downstream. This is in contrast with late time complex vortical structures shown in figure 1.2(b), which show streaks of darker fluid trapped fully inside the lighter fluid. This can only occur if there is significant three-dimensionality that results in out-of plane fluid being entrained in to the plane of visualization. At these late times, single-wavelength perturbations have interacted and developed into larger scales in the process described by Youngs (1984). Nonlinearity at late time is evident from the presence of a wide range of scales not seen

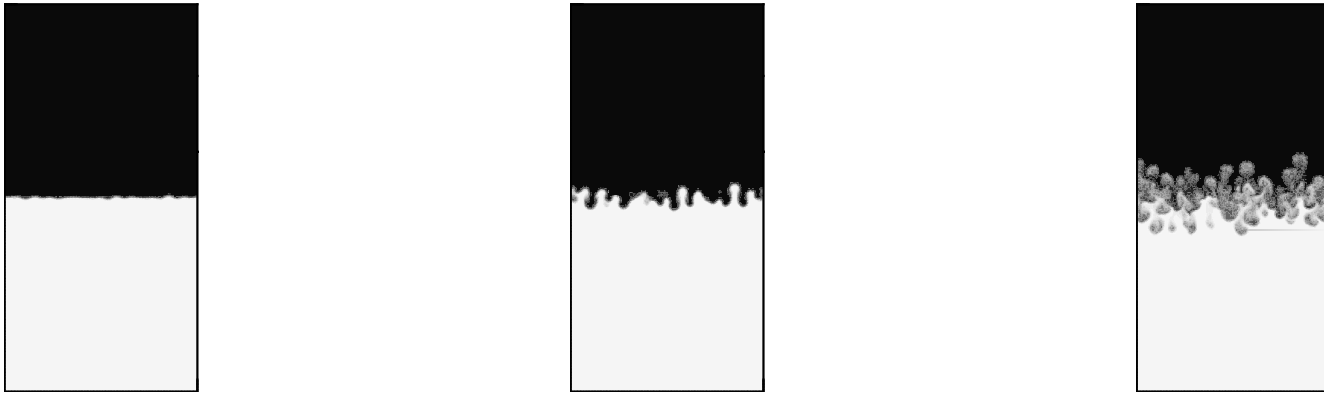
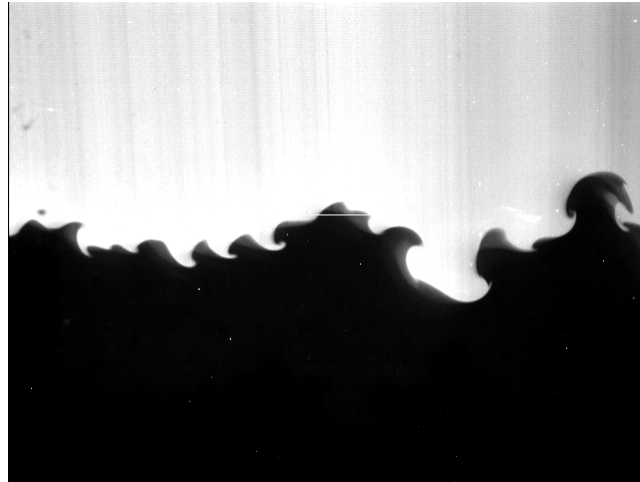


Figure 1.1 Stages of evolution of R-T instability.



(a)



(b)

Figure 1.2. Planar Laser Induced Fluorescence (PLIF) images at (a) early and (b) late times of evolution of the R-T instability.

in figure 1.2(a). The bubbles seen at late time are traveling downward with a terminal velocity defined below. The mushroom-shaped structures in figure 1.2(b) are typical of R-T mixing layers. Figure 1.2(b) also shows many secondary roll-up processes, especially on the large inverted mushroom, slightly left of the vertical centerline. Often these secondary roll-ups are driven by shear resulting in a localized Kelvin-Helmholtz (Waddell, Niederhaus, & Jacobs 2001) instability. We return to this mixing process for a detailed investigation in section 4.1.

Once at self-similarity, dimensional analysis (Youngs 1984) shows the half mix-width  $h$ , must grow quadratically with time according to:

$$h = \alpha A_t g t^2, \quad (1.2.1)$$

where  $A_t$ , the Atwood number is the governing parameter of the flow defined by  $A_t = (\rho_1 - \rho_2) / (\rho_1 + \rho_2)$ ,  $\rho_1$  and  $\rho_2$  are the cold and hot water densities employed in the present work,  $g$  is the acceleration due to gravity, and  $\alpha$  is a constant. For large  $A_t \rightarrow 1$  (as  $\rho_1 / \rho_2 \rightarrow \infty$ ), the mix is no longer symmetric about the density interface, then  $h$  corresponds to the bubble penetration distance from the position of the initial unstable interface.

Equation (1.2.1) for  $h$  was arrived at by Youngs (1984) through a nonlinear extension of the linear stability theory (Chandrasekhar 1961). In the linear regime, assuming the viscous forces are negligible, the growth rate of the most dominant mode is given by (Chandrasekhar 1961)



$$n_m = \left\{ \frac{\pi g}{l_m} \frac{\rho_1 - \rho_2}{\rho_1 + \rho_2} \right\}^{1/2}, \quad (1.2.2)$$

where  $l_m$  is the dominant wavelength. In the nonlinear regime, the width of the mix may be taken as being proportional to the dominant wavelength (Lewis 1950), and  $h \sim l_m$ . If the dominant mode takes  $N$  exponential turnover times to evolve, then  $n_m t = N$ . Thus, solving (1.2.2) for  $l_m$ , the mix width is given by

$$h \propto l_m = \frac{2\pi}{N^2} \frac{\rho_1 - \rho_2}{\rho_1 + \rho_2} g t^2. \quad (1.2.3)$$

This argument is similar to the “ $e^{10}$ ” approach for describing the transition of Tollmien-Schlichting waves in a boundary layer (Jaffe 1970). Indeed, coincidentally Youngs (1984) suggests taking  $N = 10$  (i. e., 10 exponential turnover times). This gives an estimate for  $\alpha$  as  $2\pi N^2 \sim 0.06$ . Another approach is to employ the terminal velocity for a dominant wavelength (bubble), given by  $v_\infty \propto c_\infty \sqrt{(\rho_1 - \rho_2 / \rho_1) g R_b}$  where  $R_b$  is the bubble radius (Daly 1967; Ratafia 1973). Daly also suggests the use of  $D_b \sim \lambda_b = l_m \rho_1 / (\rho_1 + \rho_2)$  to characterize the dependence of spike and bubble diameters on the wavelength and density ratio  $\rho_1 / \rho_2$  i.e. at high-density ratios ( $A_t \rightarrow 1$ ), the spikes are very narrow and  $D_b = l_m$ . At low-density ratios, spikes and bubbles have nearly equal diameters given by  $D_b = l_m / 2$ . Substituting for  $R_b = D_b / 2$  in the above expression for bubble terminal velocity, we get  $v_\infty = c_\infty \sqrt{A_t g l_m / 2}$ . For low Atwood numbers ( $\rho_1 / \rho_2 = 1.1$ ), Daly (1967) found  $c_\infty$  to be  $\sim 0.7$ . This is supported by our single-mode simulations, performed under experimental conditions (section 5.3). Then, in the

nonlinear regime, we can take  $v_\infty = dh/dt = dl_m/dt$  giving upon integration over time,  $l_m = \alpha A_1 g t^2$  and  $\alpha \sim 0.05$ , using  $h \sim l_m$  and  $h = 0$  at  $t = 0$ .

The buoyancy driven instabilities described above appear in environmental flows such as effluent discharge into rivers and estuaries, and in industrial applications such as heat exchangers and sprays in internal combustors (Beale & Reitz 1999). Rayleigh-Taylor mixing also occurs during the implosion phase of the Inertial Confinement Fusion process (Lindl 1998), which involves the high-power laser bombardment of a target fuel capsule. Target surface imperfections and non-uniformities in the beam provide initial perturbations for the R-T pressure-driven hydrodynamic instability. Here turbulence-induced mixing sets an upper limit on the peak implosion velocity resulting in the reduction of yield, and it is of interest to dampen the growth of the instability in such cases. Perhaps the largest observable R-T mix is the finger-like ejecta of stellar material believed to be present in the remnants of a young supernova (Gull 1975).

The earliest single-mode R-T experiments were done by Lewis (1950), using fluids of different densities in a vertical tube accelerated by air pressure. Emmons *et al.* (1960) generated a pressure gradient by accelerating a tank containing methanol and air along guide rails. Read (1984) was the first to perform experiments that investigated multimode R-T driven mixing. He used solid-fuel rockets to generate accelerations up to 76g, although the experiment allowed only a few milliseconds of data collection time. Early work on buoyancy-driven flows include the experiments of Jevons (1857) who

studied the formation of cirrus cloud formation through a thermal inversion of a stable interface. Dimonte & Schneider (1996) used a setup similar to Read (1984), but with the acceleration provided by Linear Electric Motors (LEM). Both experiments were capable of handling large density differences. Other methods of obtaining an unstably stratified interface include quickly overturning a narrow box filled with the light fluid on top of the heavy (Andrews 1986; Andrews & Spalding 1990), and withdrawing a plate that initially separates the two fluids (Linden, Redondo & Youngs 1994; Dalziel, Linden & Youngs 1999). All these experiments have short data collection times, and the need for a large number of repeat runs that has limited the extent of statistical data collection.

Recent advances in modeling of buoyancy driven turbulence include the Spectral Transport Model of Besnard *et al.* (1990), Besnard *et al.* (1992), Steinkamp (1995), Steinkamp, Clark & Harlow (1995), and Wilson, Andrews & Harlow (1999), the two-fluid models of Youngs (1989), Andrews (1986), and the Reynolds Stress/Boussinesq models of Snider & Andrews (1996). All of these advanced models for R-T mixing require detailed measures of turbulent quantities such as  $\overline{\rho'^2}$ ,  $\overline{u'^2}$ ,  $\overline{v'^2}$ ,  $\overline{u'v'}$ , and  $\overline{u'v'v'}$  to validate closure models. Although these quantities may be computed from Direct Numerical Simulations (DNS), such calculations are limited to relatively low-Reynolds numbers; thus, there is a continuing need to obtain these quantities experimentally. A recent high resolution simulation by Cook & Dimotakis (2001) was performed at Taylor Reynolds numbers of up to 100, the threshold for mixing transition (Dimotakis 2000). Such a simulation constitutes one realization of the spatially evolving mixing layer of the

current experiment and is typical of the current state-of-the-art of DNS of R-T mixing. Thus, the R-T mix represents a leading grand challenge problem in the DNS of turbulent flows, placing stringent requirements on resolution in time and space, and desired ensemble averages. We also note the prevalence of Large Eddy Simulation (LES) techniques in the study of R-T flows, especially at high Reynolds numbers. The Monotone Integrated Large Eddy Simulation technique (MILES) has been shown to be particularly attractive in the study of flows with discontinuities such as R-T (Youngs 2003).

To predict the turbulent mixing that occurs within the self-similar region, it is important to understand the mechanisms and structure of the turbulent flow-field. In this work, we do this through studying measurements of turbulent velocity and density fields. Over the past eight years Andrews and collaborators (Snider & Andrews 1994; Wilson *et al.* 1999; Wilson & Andrews 2002) have developed a statistically steady, low Atwood number, Rayleigh-Taylor mixing experiment based on the concurrent flow off the end of a splitter plate of cold ( $\rho_1$ ) water over hot ( $\rho_2$ ). The experiment permits extended data collection times (ten minutes or longer), with collection of statistically convergent data, and does not have long time transients. In the present work, we employed Particle Image Velocimetry (PIV) to investigate R-T mixing. We note that Prestridge *et al.* (2000) used PIV and flow visualization techniques to observe the instantaneous two-dimensional (2D) velocity and density fields in their Richtmeyer-Meshkov experiments. Dalziel (1993) used Particle Tracking Velocimetry to investigate low-Atwood number mixing in

his tank and barrier experiments. In this study, turbulence quantities and their spectra were determined from detailed 2D slices of 3D turbulent velocity fields obtained using PIV (for a review of PIV techniques see Adrian 1991), and from high-resolution single-point thermocouple measurements. Independently, Lawrence, Browand and Redekopp (1991) used a related experimental setup in their study of compound mixing due to shear and a stable density stratification. Another version of the experiment can be seen at the end of the film by Stewart (1968).

The implication of (1.2.1) is that at self-similarity all memory of the initial conditions has been lost, and the only relevant length scale is  $gt^2$ . While this suggests that  $\alpha$  is a universal constant, experiments and numerical simulations have produced differing values. The value of  $\alpha$  has been measured at  $\sim 0.03$  from numerical simulations (Youngs (1984); Young *et al.* (2001)), while experimental values are usually higher. Dalziel (1993), Snider & Andrews (1994), and Read (1984) report a value of 0.07 from their experiments, while the LEM experiments of Dimonte & Schneider (2000) give a value of 0.05. Glimm *et al.* (2001) use a front-tracking algorithm in their 3D simulations that yield a value of 0.07 comparable to experiments. Linden, Redondo & Youngs (1994) report a value of  $0.044 \pm 0.005$ , after introducing a virtual origin to account for any transients that may be present due to the initial withdrawal of the dividing plate in their experiment. The difference in the values of  $\alpha$  between experiments and numerical simulations is believed to be due to the presence of long-wavelengths in experiments, while most numerical simulations are initialized with short-wavelength content that

evolve purely through mode-coupling (Cook and Dimotakis 2001; Young *et al.* 2001; Youngs 2003). When such long wavelengths are present,  $\alpha$  is no longer universal, but depends (logarithmically) on the initial amplitudes. Conversely, in the mode-coupling limit present in most numerical simulations  $\alpha$  takes up a lower bound universal value (Dimonte 2003). A comparative study involving many state-of-the-art numerical techniques to resolve the differences between numerical simulations and experiments has been recently undertaken (Dimonte *et al.* 2003). We participated in this study, and our findings are summarized in Appendix C.

3D numerical calculations to test the effect of initial amplitudes on the growth constant  $\alpha$  were conducted as part of the present work. It was suggested by Dimonte (2003), that the growth constant  $\alpha$  would vary logarithmically with the non-dimensional initial amplitude  $k\langle h_{0k} \rangle$ , where  $k$  is the dominant wavenumber of the initial wavepacket, and  $\langle h_{0k} \rangle$  is the initial root mean square (r.m.s.) amplitude. A total of eight simulations, each of size  $128 \times 128 \times 256$  points, and with amplitudes  $k\langle h_{0k} \rangle$  ranging from  $3 \times 10^{-6}$  to  $4 \times 10^{-2}$  were conducted to test the above hypothesis. A 3D, finite-volume, Euler equation code with Van Leer flux limiters developed by Andrews (1995) was used in these computations. Both 2D and 3D versions of this code have been extensively validated (Andrews 1995; Dimonte *et al.* 2003). The above calculations were initialized with modes ranging from 1-32 in some cases, and 2-32, and 3-32 in others, to investigate the role played by the minimum imposed mode (longest wavelength). To study the opposite mode-coupling limit, two calculations with an initial annular shell of energy in modes

16-32 but with amplitudes that differed by two orders of magnitude were performed. Furthermore, the effect on  $\alpha$  of different spectral structures (with slopes = 0, -1, -2) was also studied.

A detailed comparison of experimental results from the turbulent R-T mixing layer with data from numerical simulations was undertaken. The numerical simulations were initialized with experimentally obtained density and velocity data at the start of the flow. The results of the numerical simulations were compared with velocity and density measurements obtained from the flow at later times. The flow parameters (including the density difference), dimensions of the experiment, and the initial conditions, were maintained the same in both the simulations and the experiment. The objective of such a comparative study was to resolve outstanding differences obtained in the value of the so-called universal growth constant,  $\alpha$  between current numerical simulations and experiments. It is widely believed that experiments report higher values of  $\alpha$  due to the presence of long wavelength modes that dominate the growth at late times. While there have been previous numerical studies to attempt an explanation of these differences, most of them have not used the exact conditions present at the start of the experiment. It is hoped that this study will provide a better understanding of the role of long wavelengths on the value of  $\alpha$ . If the experiment can exactly be modeled through numerical simulations, this will allow us to run “numerical experiments” under conditions that cannot easily be implemented in the experiments. Some examples are

variable acceleration studies, initial conditions that cannot be implemented in the experiment, effect of shear etc.



## 2. EXPERIMENTAL SETUP AND DIAGNOSTICS

### 2.1 Preliminaries

A detailed description of the water channel experimental setup, and the diagnostics used to make density and velocity measurements in the next section. A novel technique developed to measure both density and velocity simultaneously is described in section 3.1. Figure 2.1 is a schematic of the experimental setup. The channel consisted of upper and lower entry plenums separated by a splitter plate. The cold water channel was fed from a 500 gallon tank, and a second lagged 500 gallon tank of warm water fed into the lower channel. The cold and warm water streams entered the channel at a mean velocity of  $\sim 4.4$  cm/s. This value of the velocity was chosen so that the parabolic flow (1.2.1) extended over 60 cm, where data could be collected. The density difference was achieved through a temperature difference of 5 to 10°C in the water. Temperature data was converted to density through the following equation of state (Kukulka 1981):

$$\rho = \frac{\left( 999.8396 + 18.2249T - 0.007922T^2 - 55.448 \times 10^{-6}T^3 \right)}{(1 + 18.159 \times 10^{-3}T)} + \frac{149.756 \times 10^{-9}T^4 - 393.295 \times 10^{-12}T^5}{(1 + 18.159 \times 10^{-3}T)} \quad (2.1.1)$$

where  $T$  is in °C, and  $\rho$  is in kg/m<sup>3</sup>. The above expression is nearly linear at temperatures in the range of 15°C to 25°C for the present experiment. Both tanks contained sump pumps to ensure a uniform temperature was maintained in the tanks throughout the experiment. Thus, cold (heavier) water entered through the top plenum, while warm (lighter) water entered through the lower plenum, and the two streams

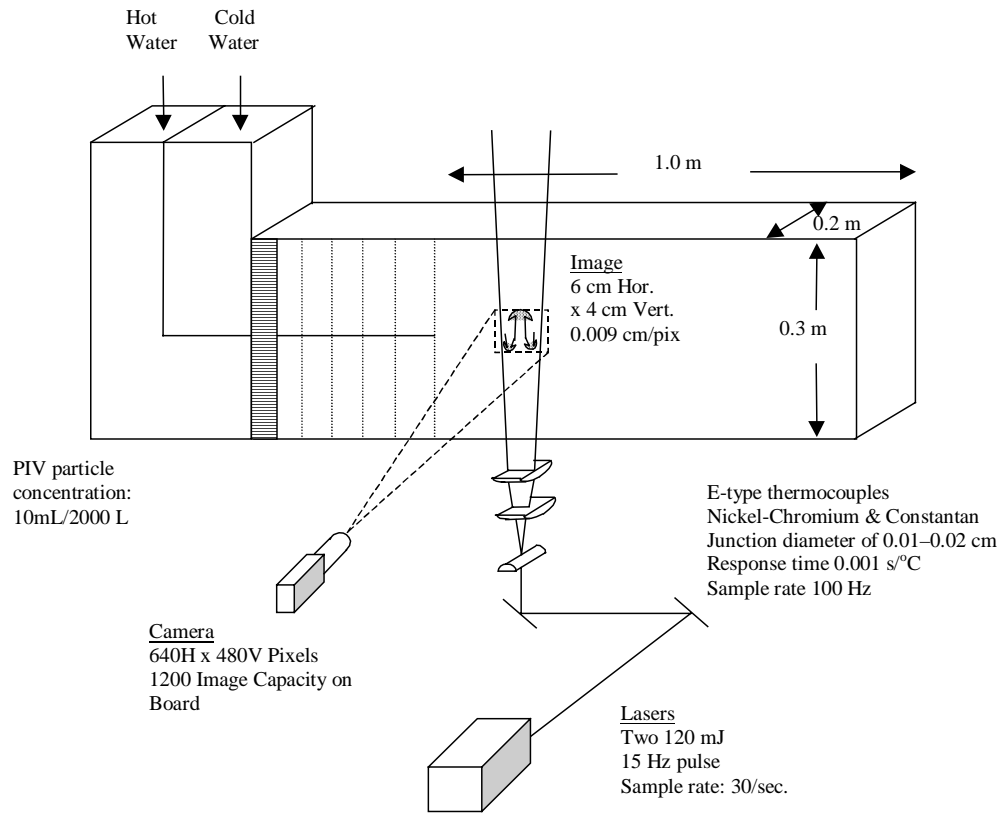
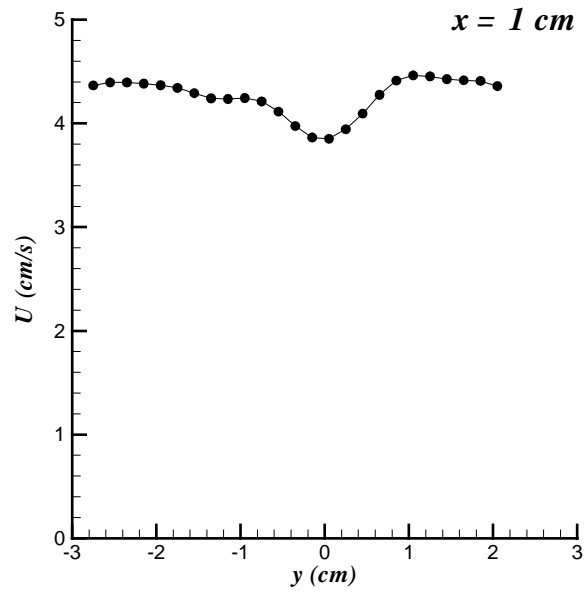
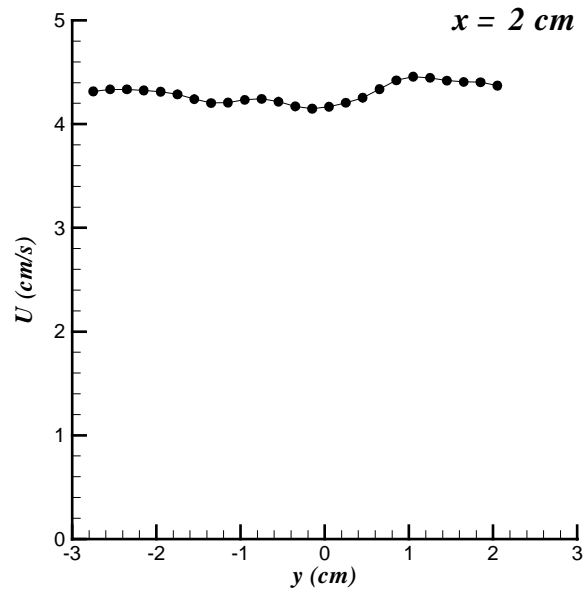


Figure 2.1. Schematic of experimental setup.

formed an unstable Rayleigh-Taylor mix as they left the edge of the splitter plate. The resulting flow was statistically steady, allowing for long data collection times albeit at small Atwood numbers  $A_t < 10^{-3}$ . No shear between the two fluid streams was employed in the present work. Nigrosene dye was injected at the splitter plate, and the flow velocities were adjusted until the dye was convected downstream without undergoing any distortion due to shear. From late-time mean velocity profiles across the mix, the amount of shear was determined to be  $< 1\%$  of the mean convective velocity. The flow channel was 241 cm long (including the inlet and exit plenums), 31 cm deep, and 15 cm wide. At this width, the front and back walls of the channel did not have any effect on the development of the mix in the central region (Snider & Andrews 1994). The test section where the data was collected was 100 cm long. The splitter plate was 0.32 cm thick, with a  $2.5^\circ$  knife-edge. Calibrated rotameters were used to regulate the mean flow rate. Screens and flow straighteners in each of the plenums minimized free-stream turbulence (Snider & Andrews 1994), and suppressed the growth of boundary layers on the walls. A fine mesh (35 mesh/in.) at the end of the splitter plate absorbed some of the momentum deficit



(a)



(b)

Figure 2.2 Mean velocity profiles at  $x = 1$  cm (a) and  $x = 2$  cm (b).

introduced by the knife-edge. The leaning of early-time structures seen in figure 1.2 (a) is due to the development of boundary layers on the splitter plate. From the mean velocity profiles immediately after the splitter plate at  $x = 1$  cm (figure 2.2 (a)), the associated velocity deficit was estimated to be  $\sim 0.4$  cm/s ( $\sim 10\%$  of the mean convective velocity). However, this velocity defect is neutralized rapidly by  $x \sim 2$ cm (figure 2.2 (b)) due to the buoyancy-driven vertical transport of momentum and due to diffusion. The velocities shown in figure 2.2 were measured using the Particle Image Velocimetry technique described in the next section.

## 2.2 PIV System

The PIV system consisted of two Nd-YAG lasers that fire alternately each at a rate of 15 Hz, giving a net sampling rate of 30 Hz. The pulse duration of the lasers was 5 ns, ensuring that the images represented the instantaneous positions of the particles. The laser beam was passed through an array of cylindrical lenses to produce a laser sheet of thickness less than 1 mm. Neutrally buoyant, hollow silvered spheres of diameter  $10 \mu\text{m}$  were used to seed the flow. Seed particle concentrations were varied from 3 ml to 6 ml per 500 gallons of the cold and hot water, and were well stirred into the water by the sump pumps. A KODAK Megaplus digital camera, triggered synchronously with the lasers, was used to record the images with arrays of size  $640 \times 480$  pixels. Typically, 1200 images were collected to obtain convergent statistics (Ramaprabhu & Andrews 2003<sup>a</sup>). A *labview* based system was used to control triggering of the lasers and data collection.

The displacement of a particle in two successive images gives the velocity vector at that point. Our requirements for PIV were standard, and so we used the readily available MATPIV program, a cross-correlation based software (Grue *et al.* 2000). The cross-correlation function  $R(x,y)$  was computed from the two image fields,  $I_1$  and  $I_2$  as

$$R(x,y) = \sum_{i=-M/2}^{M/2} \sum_{j=-N/2}^{N/2} I_1(i,j)I_2(i+x,j+y), \quad (2.2.1)$$

where  $M = N = 2^n - 1$ ;  $n = 3, 4, 5, \dots$ . The mean intensities were subtracted from  $I_1$  and  $I_2$  and the resulting value of  $R(x,y)$  was normalized by the correlation coefficient. The location of the correlation peak with respect to the center of the interrogation window gives the local displacement vector. The vector field is smoothed by a signal-to-noise ratio filter and a global histogram filter. Vectors with a signal-to-noise ratio less than 1.1 or lying outside two standard deviations of the neighboring vectors were replaced by interpolated values. The PIV software yields 1199 vector fields from the 1200 grayscale images. First, second, and third order statistics were computed from the vector fields. One concern is that local density variations can influence the refractive index, resulting in an apparent displacement of the particle position along the line of sight. However, for the low values of density differences used in this experiment, and the short beam traverse distances along the line of sight, this effect was explored and found negligible (see Appendix A; Ramaprabhu & Andrews 2003<sup>a</sup>). Following the method of Adrian (1997), we determined the error in our velocity measurements to be  $\sim \pm 0.05$  cm/s based

on the uncertainty associated with the location of a particle. The resolution issues of the PIV technique are explored in detail in section 4.3.

### 2.3 Thermocouple System

The temperature diagnostics consisted of a vertical rake of thermocouples that were positioned at the centerline of the mix at different downstream locations in the channel. The thermocouple probes were E-type (Nickel-Chromium and Constantan) and welded at the tip to form a bimetallic junction. The thermal response of the E-type thermocouple was  $\sim 0.001$  s/ $^{\circ}$ C (Wilson & Andrews 2002), while the accuracy was  $\pm 0.1^{\circ}$ C (Wilson 2002). A 16-bit data acquisition board collected data from the thermocouples at a maximum sampling rate of 100,000 Hz. To remove some of the noise, local averages of over 1000 samples were performed, resulting in a net sample rate of 100 Hz. The welded thermocouple probe tip was approximately 0.01 cm in diameter. At a downstream distance of 30 cm from the splitter plate, a local mixing Reynolds number may be computed by balancing the potential energy released against the turbulent kinetic energy of the flow to obtain (Snider & Andrews 1994)

$$\text{Re}_x^a = \sqrt{\frac{gA_t}{6}} \frac{(2h_x)^{3/2}}{\nu}, \quad (2.3.1)$$

where  $h_x$  is the mix width (taken to be the distance between points where the mean density is 5% and 95% of the cold or hot fluid) at a downstream distance  $x$  and  $\nu$  is the kinematic viscosity. At this location, the Kolmogorov turbulent scale ( $\eta_k$ ) is given by

$$\eta_k = h_x \text{Re}_x^{a-3/4}. \quad (2.3.2)$$

The corresponding Batchelor scale ( $\eta_B$ ), which is relevant for scalar (thermal/density) fluctuations is

$$\eta_B = \eta_k Pr^{-1/2}, \quad (2.3.3)$$

where  $Pr$  is the Prandtl number ( $Pr \sim 7$  for water at 20°C). At  $x = 30$  cm, equation (2.3.3) gives  $\eta_B = 0.02$  cm, which suggests that the Nyquist spatial resolution criterion is satisfied at the current sampling rates. However, for  $x > 30$  cm, this criterion is not met, and the smallest scales of turbulent motion may not be fully resolved. The data collection time was  $\sim 160$  s, which was chosen to allow more than 80 of the largest scale structures to be recorded (the turnover time of the large scale structures is given by  $T = 2h_x/U \sim 2$  s, where  $U$  is the mean convective velocity of the flow). The long data collection times and the high sampling rate resulted in capturing almost four decades of frequencies. The configuration and details of the thermocouple system are further described in Wilson & Andrews (2002), with a detailed consideration of the Batchelor scale.

During the course of the experiment, the following recursive procedure ensured that the thermocouple was located at the geometric centerline of the mixing layer. Initially, the thermocouple was placed close to the mixing layer centerline by visual inspection (the vertical position of the thermocouple, mounted on a rake, can be adjusted by a vernier screw arrangement), and the data logged. Dye was added to one of the fluids to distinguish the two streams. The data acquisition software computes and prints out the centerline temperature offset factor:



$$\phi = (T_{mean} - T_2)/(T_1 - T_2) \quad (2.3.4)$$

at the end of the data logging process. If  $\phi \neq 0.5$ , the position of the thermocouple is readjusted using a false positioning method (i.e., linear interpolation), and the data logging process is repeated. The process is repeated until  $\phi$  approaches 0.5 to within an accuracy of 5%.

In equation (2.3.1), the Reynolds number was defined assuming that all the initial potential energy in  $h_x$  associated with the unstable density interface was converted completely to kinetic energy. In a buoyancy driven mix with no shear, the mean convective velocity does not contribute to the dynamics of the buoyant mix. As a result, the definition of a Reynolds number often becomes a matter of preference depending on the choice of a suitable velocity scale. Some commonly used definitions are reviewed here. The self-similar nature of this flow may be incorporated into a Reynolds number definition by using the mix width as the length scale, and its time derivative as the corresponding velocity scale (Cook & Dimotakis 2001):

$$\text{Re}_x^b = \frac{h_x \dot{h}_x}{\nu} \quad (2.3.5)$$

An alternative definition uses the terminal velocity introduced earlier in section 1.2 as the velocity scale, resulting in a form close to equation (2.3.1):

$$\text{Re}_x^c = \frac{v_\infty \cdot 2h_x}{\nu} = \frac{2h_x}{\nu} 0.7 \sqrt{A_1 g h_x / 2} \quad (2.3.6)$$

Implicit in (2.3.5) is the use of a r.m.s. velocity scale  $v' \sim \dot{h}_x$ , whereas (2.3.6) uses the terminal velocity of the bubbles in this flow. Finally, at the microscales, a Taylor Reynolds number may be defined based on the Taylor length scale  $\lambda$  and the r.m.s. velocity scale:

$$Re_\lambda = \frac{\lambda v'}{\nu}. \quad (2.3.7)$$

The Taylor Reynolds number is a universal measure of the state of turbulence since it is defined independent of the large-scale features of the flow. For instance, it has been argued that a Taylor Reynolds number of 100 is required to cross the mixing transition threshold for all turbulent flows (Dimotakis 2000). The Reynolds numbers computed from the above definitions are listed for our experiment in Table 2.1 for  $x = 35$  cm. All the definitions based on large-scale features of the flow have similar values of the Reynolds numbers, indicating that these different velocity and length scale definitions are equivalent. Equation (2.3.1) seems to give the highest value ( $\sim 1450$ ), but this may be due to the omission of energy losses due to dissipation. An experimental estimate of dissipation losses is presented in section 4.5.

Equation (2.3.1)	$\sqrt{\frac{gA_t}{6} \frac{(2h_x)^{3/2}}{\nu}}$	1450
Equation (2.3.5)	$\frac{h_x \dot{h}_x}{\nu}$	1000
Equation (2.3.6)	$\frac{h_x v_\infty}{\nu}$	1250
Equation (2.3.7)	$\nu \lambda / \nu$	60

Table 2.1. Reynolds number definitions for R-T flow

### 3. SIMULTANEOUS MEASUREMENTS OF VELOCITY AND DENSITY FIELDS (THE PIV-S METHOD) \*

#### 3.1 Preliminaries

A variant of the PIV technique is described to measure velocity and density simultaneously in a turbulent Rayleigh-Taylor mixing layer. The velocity field is computed by the usual PIV technique of cross-correlating two consecutive images, and deducing particle displacements from correlation peaks of intensity fields. Different concentrations of seed particles were used in the two streams of different temperature (density) fluids, and a local measure of the density was obtained by spatially averaging over an interrogation window. Good agreement is reported between the first and second order statistics for density obtained from this technique and from a thermocouple. Velocity-density correlations computed by cross-correlating individual timeseries are presented. The errors in the density measurements are quantified and analyzed, and the issue of spatial resolution is also discussed. Our purpose here is to introduce the PIV-S method and validate its accuracy against corresponding thermocouple measurements.

In a buoyancy driven flow, such as an R-T mix, temperature plays the role of a ‘dynamic’ scalar influencing the evolution of the velocity field (and being influenced by it) through the buoyancy term and Boussinesq approximation. The resulting turbulence can be characterized, in part, by velocity-density correlations; and, it is of interest to

---

\* Parts of this section including figures 2,3,4,5,6,7,8,9,10,11,12,13 have been reprinted with permission from *Expts. Fluids* **34**, 98–106, 2003 Ramaprabhu, P., & Andrews, M.J., Simultaneous measurements of velocity and density in buoyancy-driven mixing. Copyright Springer-Verlag.

turbulence modelers and for DNS validation to study the variation of such statistics across the mix. A non-intrusive, whole-field technique that we call PIV-Scalar, or PIV-S, is used here to simultaneously measure velocity and temperature (density) fields. The two streams of different temperatures (densities) in an R-T mix are seeded with different concentrations of particles, and a digital camera takes snapshots of the instantaneous intensity field  $I(x,y)$  of reflected light. The velocity field is obtained by a standard PIV cross-correlation technique, while the density field is obtained by performing local spatial averages of the intensity field within interrogation windows roughly the size of 1mm x 1mm (24 x 24 pixels). Thus,

$$\rho(x_c, y_c) \propto \frac{1}{A} \int I(x, y) dA \propto \sum_{j,k=1}^N I(x_j, y_k) \quad (3.1.1)$$

where  $(x_c, y_c)$  denotes the geometric center of the interrogation window of size  $N \times N$  pixels. It is not necessary to determine the constant of proportionality in the above equation since we work with non-dimensional quantities. This also removes the need to calibrate the PIV-S method. Furthermore, this method is simple to implement, and yields low error values, as we shall describe.

Although variation of seed particle concentrations has been used before to determine velocity-density fields (Simoens *et al.* (1996)), they have large errors, particularly in the measurement of second-order moments. This is due to the measurement of point-wise intensity values (rather than local averages as suggested by equation (3.1.1)) as an indicator of density, thus leading to unreliable realizations. Furthermore, these methods

require two cameras to capture the velocity and density fields, introducing additional alignment errors.

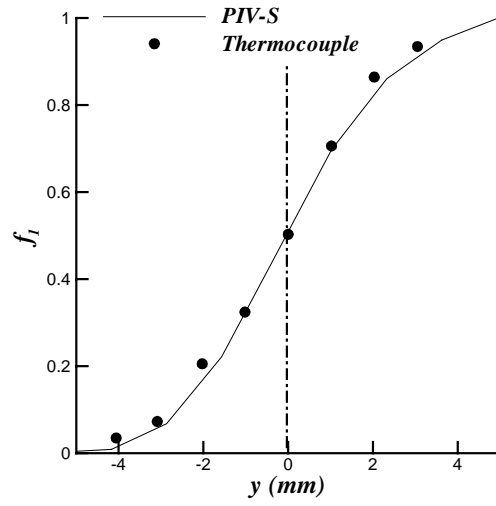
Another technique commonly used is Digital Particle Image Velocimetry/Thermometry or DPIV/T (Dabiri & Gharib 1991; Park *et al.* 2001), which involves seeding the flow with liquid crystal particles that change color in response to temperature changes. From the color of the particle, the local temperature is inferred, while the displacement of the particles gives the velocity field. The measurement of color is more complicated (color is a three-dimensional vector with components [R,G,B]) than that of the intensity (a scalar) and requires sophisticated post-processing techniques. This method also suffers from uncertainties that stem from manufacturing defects of the particles, causing them to reflect light at different wavelengths even while at the same temperature (variations of 5-20% have been observed). In addition, the standard deviation of the wavelength of reflected light is itself a function of the temperature, making this technique difficult to

calibrate. Although Park *et al.* removed some of the errors by local spatial averaging, significant errors remained, in some cases up to 8%.

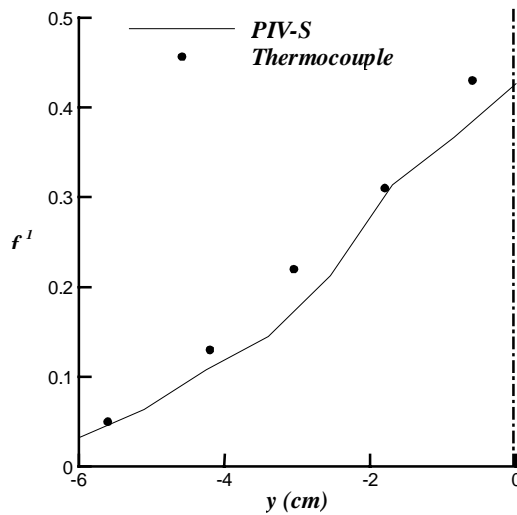
Sakakibara and Adrian (1999) used PIV and Planar Laser Induced Fluorescence (PLIF) in tandem to measure velocity and density fields, respectively. The use of dye gives very high spatial resolution. This method not only requires two cameras, but also suffers from sensitivity of fluorescent dye to light intensity, which may vary due to refraction. Sakakibara and Adrian (1999) overcame this problem by introducing a two-dye technique, with each dye having a different temperature response so that the ratio of the fluorescence intensities itself is independent of the temperature. They estimate the overall accuracy of the method to be around 95% for the mean quantities.

### *3.2 Density Measurements*

The first and second order moments (mean and fluctuation) of density at two downstream locations, viz.  $x \sim 2.5$  cm and  $x \sim 35$  cm from the splitter plate, are presented here. A 24 x 24 pixel (1 mm x 1mm) window was used in the averaging



(a)



(b)

Figure 3.1.  $f_I$  profiles at (a)  $x = 2.5$  cm, and (b)  $x = 35$  cm from PIV-S and thermocouple experiments (dotted line represents centerline of mix).

process, and the reason for choosing this window size is explained in section 3.5. After trying a variety of averaging procedures, such as the use of intensity thresholds, and



point-wise averages, it was found that simply averaging the intensity within a window yielded the best results (lowest r.m.s. error of density fluctuations). All experiments were run at a temperature difference of 5°C between the hot and cold streams ( $A_t \sim 5 \times 10^{-4}$ ), and with no shear (pure buoyancy case). The density data are compared with results from thermocouple measurements at the same locations (the temperature data recorded by the thermocouple are converted to density data from (2.1.1)).

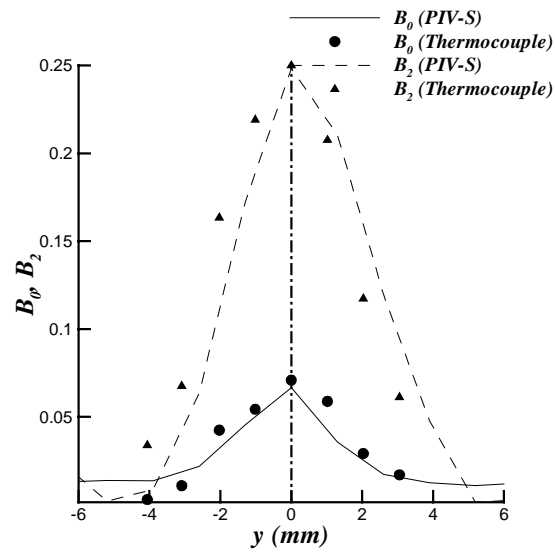
Figures 3.1 (a) and (b) show the volume fraction  $f_l$  of the cold fluid (defined as  $\frac{\bar{\rho} - \rho_2}{\rho_1 - \rho_2}$ ,

where  $\bar{\rho}$  is the time-averaged density) across the mixing layer at  $x \sim 2.5$  cm and  $x \sim 35$  cm downstream (since the mix is much wider at  $x \sim 35$  cm, due to turbulent diffusion, only half the mixing layer could be captured on the photographs in a single experiment). These first-order density statistics agree well with the thermocouple measurements (filled circles). To investigate the agreement between the thermocouple data and the PIV-S measurements, we define the following quantities commonly used (Steinkamp *et al.* 1999, Linden *et al.* 1994, Wilson and Andrews 2002) to characterize a Rayleigh-Taylor mix:

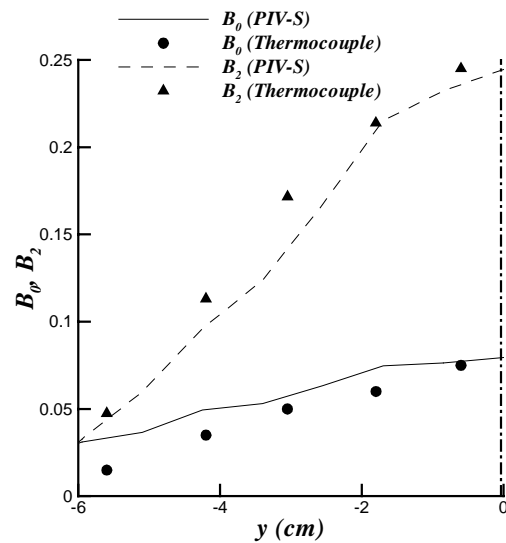
$$\begin{aligned}
f_1 &= \lim_{T \rightarrow \infty} \frac{1}{T} \int_0^T \frac{\rho - \rho_2}{\rho_1 - \rho_2} dt = \lim_{T \rightarrow \infty} \frac{1}{T} \int_0^T \frac{\rho - \rho_h}{\rho_c - \rho_h} dt \\
f_2 &= 1 - f_1 \\
B_0 &= \lim_{T \rightarrow \infty} \frac{1}{T} \int_0^T (\rho - \bar{\rho})^2 dt / \Delta\rho^2 \quad (3.2.1) \\
B_2 &= f_1 f_2 = f_1 (1 - f_1) \\
\theta &= 1 - \frac{B_0}{B_2}
\end{aligned}$$

where  $B_0$  is the nondimensional turbulent intensity of density variations across the mix, and includes the effect of molecular diffusion;  $B_2$  is the corresponding conditioned measure that would result if the two fluids were immiscible and does not account for molecular mixing. Then,  $\theta$  is a molecular mix parameter and is a measure of the extent of mixing due to molecular diffusion first introduced by Dankwerts (1952).  $\theta = 1$  implies perfect molecular mixing and  $\theta = 0$  implies no molecular mixing, i.e., pure two-fluids. In this experiment, the molecular mixing is due to heat conduction.

$B_0$  and  $B_2$  are plotted for the two downstream locations in figures 3.2 (a) and (b). As expected,  $B_0$  and  $B_2$  reach their maximum values at the center of the mix where most of the mixing takes place. Furthermore, at the center of the mix,  $f_1 = f_2 = 0.5$ , so from Equation (3.2.1)  $B_2 = 0.25$ .  $B_0$  and  $B_2$  obtained from the PIV-S and the thermocouple data compare well, particularly near the center of the mix. It is noticeable in figure 3.2 that while the thermocouple values approach zero near the edge, the PIV-S



(a)

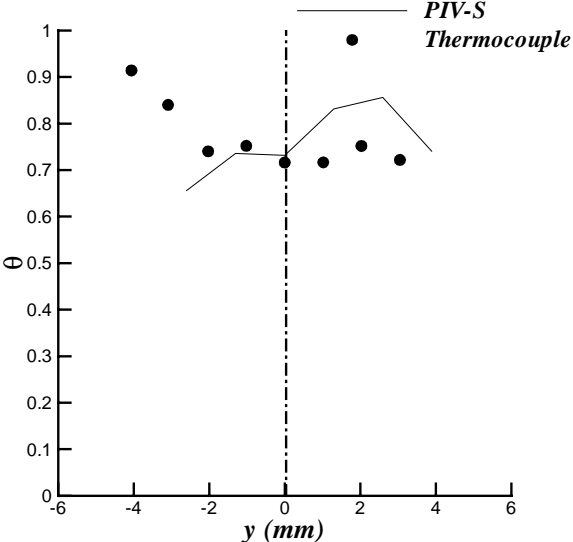


(b)

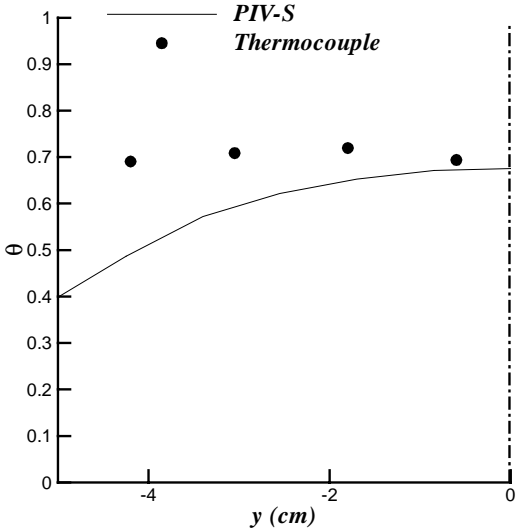
Figure 3.2.  $B_0$  and  $B_2$  profiles at (a)  $x = 2.5$  cm, and (b)  $x = 25$  cm from PIV-S and thermocouple experiments.

measurements of  $B_0$  seem to have a residual value. However, the measured two-fluid density fluctuation,  $B_2$ , agrees well between the thermocouple and PIV-S. This discrepancy may be due to a diffuse thermal edge, or perhaps due to intermittency at the

edge associated with an interface not sufficiently resolved with a spatial-averaging technique such as PIV-S (the much smaller ‘probe-volume’ of the thermocouple is better suited to resolve such sharp interfaces). The disagreement near the edge is also evident in the plots of  $\theta$  (figures 3.3 (a) and 3.3 (b)), which is particularly sensitive to measurement errors. For a fully developed R-T mix,  $B_0/B_2 \sim 0.25$ , and  $\theta \sim 0.75$  across the mix, which is observed here. Since particles have a lower rate of diffusion than heat (higher Schmidt number compared with Prandtl number), a lower value of  $\theta$  might be expected. However, this effect is diminished or eliminated in a well-mixed region such as the center of the mixing layer in these experiments. As a result, we see good agreement in the values of  $\theta$  in this region between PIV-S and thermocouple data. Indeed, experiments where salt was used instead of heat to create the density difference (Dalziel *et al.* 1999) also give similar values of  $\theta$  near the center of the mix, in spite of the much lower value of mass diffusivity associated with salt compared with heat. However, the Schmidt number does play a role away from the center of the mixing layer where PIV-S gives a lower value of  $\theta$ . But, the  $\theta$  value does not become vanishingly small in this region. We attribute this to the advection of fragments of well-mixed fluid from the center of the mix, resulting in a flow history-effect. A contour map of  $B_0$  at  $x = 2.5$  cm is given in figure 3.4 and shows



(a)



(b)

Figure 3.3.  $\theta$  across the mixing layer at (a)  $x = 2.5$  cm, and (b)  $x = 35$  cm from PIV-S and thermocouple experiments.

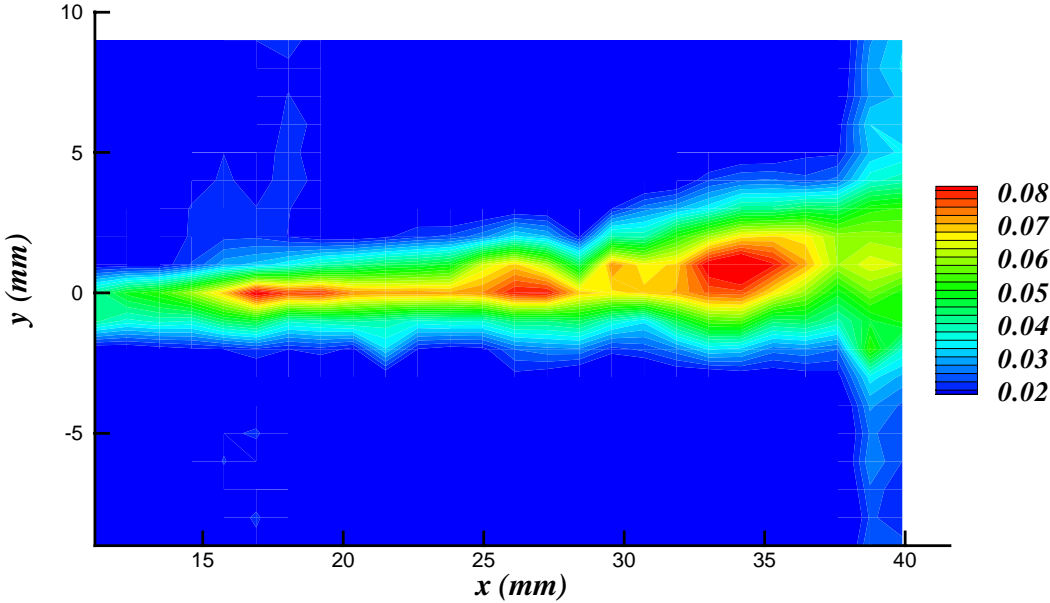


Figure 3.4. Contour map of  $B_0$  at  $x = 2.5$  cm from the splitter plate.

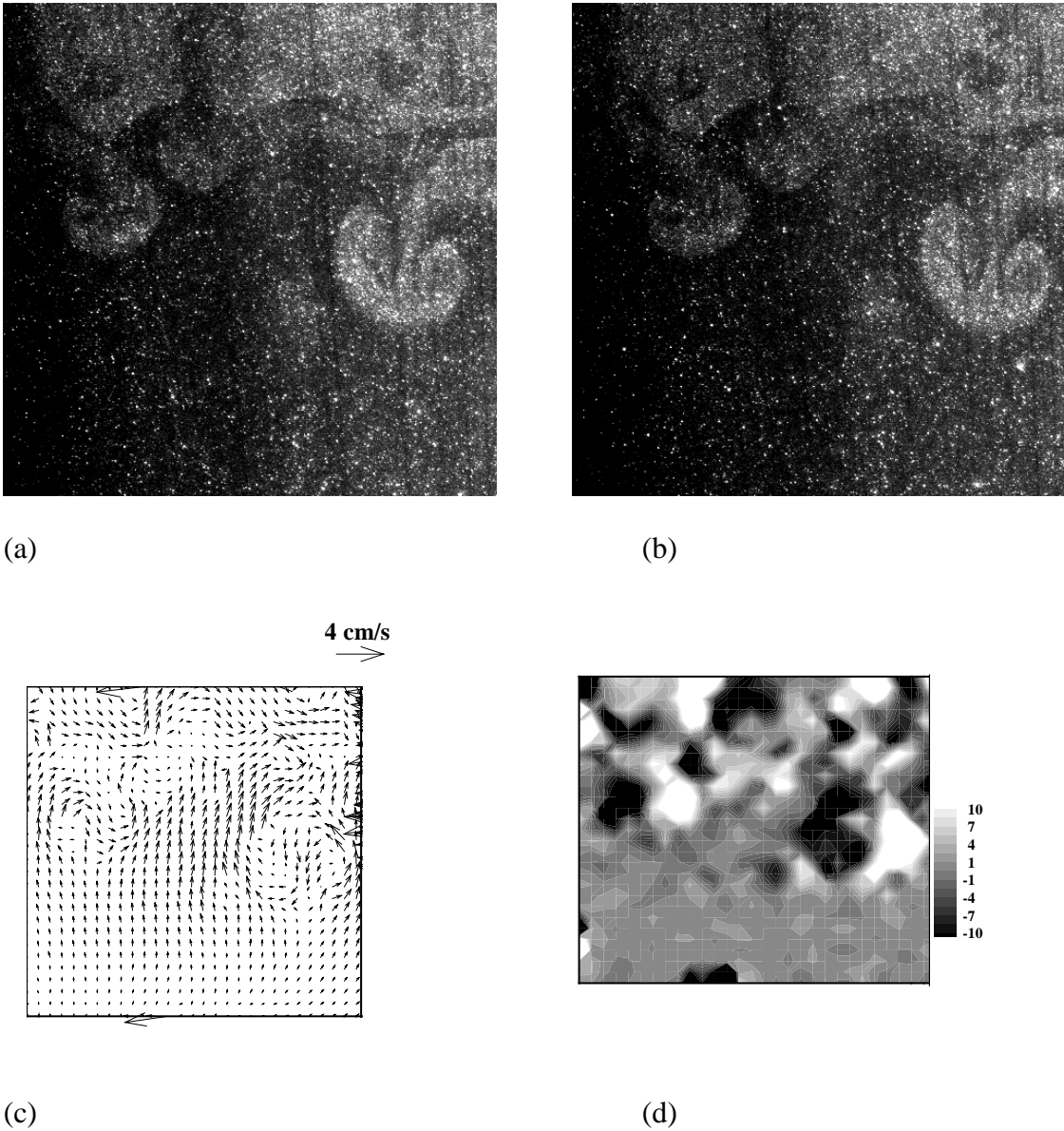


Figure 3.5. (a) and (b) Two successive particle images showing mushroom-shaped structures characteristic of R-T instability. Velocity vector field (c), and vorticity field (d) obtained by cross-correlating the image files of (a) and (b).

the divergence of the mixing layer (the area shown has physical dimensions of 3.6 cm x 2.0 cm).

### *3.3 Velocity Measurements*

Figures 3.5 (a) and (b) show a pair of successive PIV-S images (separated by a time interval of 0.033 s), in which the heavy fluid is seeded with a higher concentration of particles than the lighter fluid. The difference in particle concentrations delineate the structures in the flow. The images are 640 x 480 pixels, while the actual window size is  $\sim 6$  cm x 4 cm. The convective velocity of the flow was 4.4 cm/s in all of the experiments reported here. The images were taken at  $x = 35$  cm and are in the region of self-similar development of the buoyancy mix. The mushroom-shaped structures are characteristic of Rayleigh-Taylor instability. These vortices are three-dimensional structures, with the vorticity field resembling that of a vortex ring. This is a predominantly irrotational flow, with most of the vorticity concentrated within the rollup. Observations from the experiment of the axisymmetric nature of these mushroom structures implies isotropy between the streamwise and spanwise velocity components.

Figure 3.5 (c) shows the velocity vector field (from which the convective velocity has been subtracted) obtained as a result of correlating the two grayscale images. A 16 x 16 pixel interrogation window was used in computing the vector fields. The corresponding out-of-plane z-vorticity component (in  $s^{-1}$ ) is presented in figure 3.5 (d). Apart from a few bad vectors at the edge, the vector field captures the recirculating regions seen in the



original images. The same is true for the vorticity field, where the two-dimensional slices of the recirculating zone show up as alternate regions of positive and negative vorticity.

The vorticity field seen in figure 3.5 (d) is generated primarily through the baroclinic interaction of the density gradient and the pressure gradient (acceleration). For early stages in the instability development, the vorticity equation may be written as (Turner 1980)

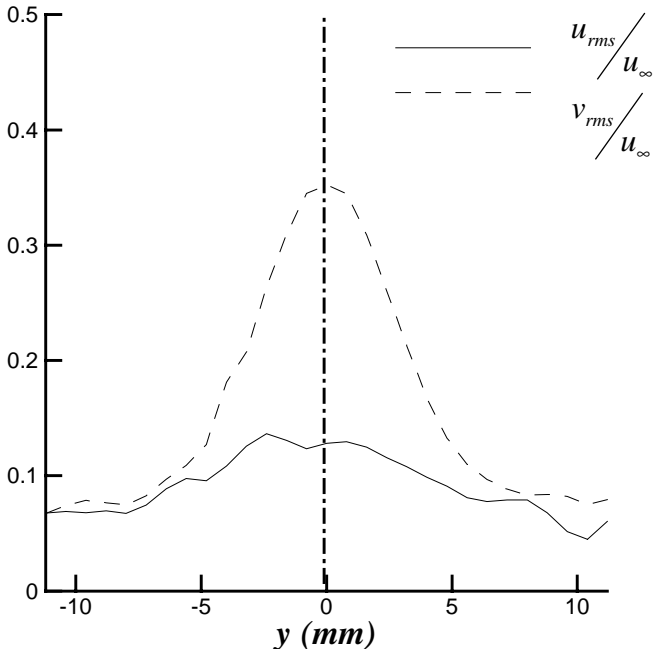
$$\frac{D\zeta}{Dt} = \zeta \cdot \nabla u + \nu \nabla^2 \zeta + \nabla p \otimes \nabla \left( \frac{1}{\rho} \right). \quad (3.3.1)$$

The first two terms in the right-hand side of the above vorticity equation indicate changes in vorticity  $\zeta$ , produced by vortex line stretching and diffusion. The third term, unique to buoyancy driven flows, describes vorticity generation through misalignment of the local density gradient and the pressure gradient. During the initial stages of our experiment, the pressure gradient is the hydrostatic pressure introduced by gravity, and vorticity generation can occur when surfaces of constant density are displaced away from the horizontal. Thus, the sign of vorticity in figure 3.5 (d) is given by the local direction of  $\nabla p \otimes \nabla(1/\rho)$  by the right-hand rule. The initially sinusoidal vortex sheets evolve through localized stretching, before rolling up to form coherent vortices in the shape of mushrooms. Depending on the vortex sheet thickness, secondary instabilities (shear-driven or buoyancy-driven) may develop within the region of roll-up (e.g. the single-mode experiments of Waddell *et al.* 2001).

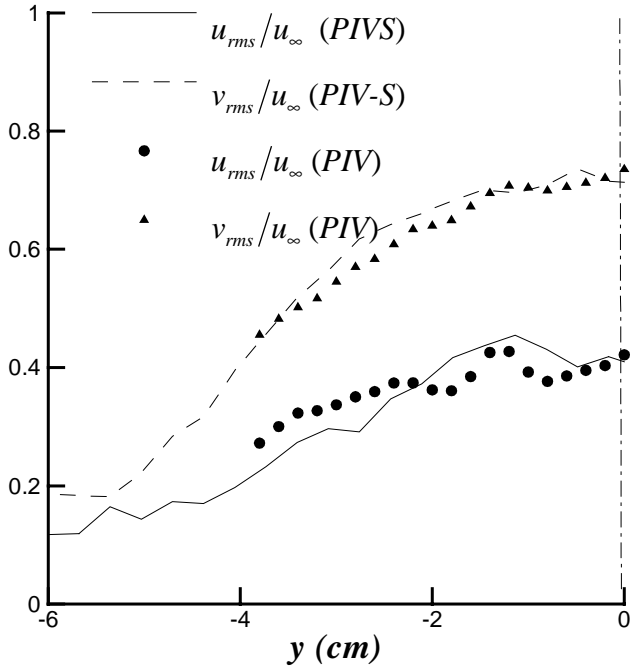
Figures 3.6 (a) and (b) are plots of the horizontal and vertical components of turbulent velocity fluctuations across the mix at  $x = 2.5$  cm and  $x = 35$  cm respectively, non-dimensionalized by a saturation velocity,

$$u_{\infty} = 0.7\sqrt{A_1 g H / 2} \quad (3.3.2)$$

(Andrews & Spalding 1990) where  $H$  is the depth of the channel. Thus,  $u_{\infty}$  represents the velocity associated with the largest wavelengths ( $\sim H$ ). Since this is a no-shear experiment,  $v_{rms}$  dominates over  $u_{rms}$  as the primary transport mechanism. This dominance is tempered downstream, as the coherent structures become more fully developed and three-dimensional. The uniform-concentration PIV experiment (symbols) also shows this trend, with the ratio  $v_{rms}/u_{rms} \rightarrow 1.5$  at  $x \sim 35$ cm observed in figure 3.6 (b). Overall, there is a good agreement between the velocity profiles of the PIV and PIV-S techniques, suggesting that the use of different concentrations of seed particles does not affect the PIV analysis. Figure 3.7 is a contour map of  $v_{rms}/u_{\infty}$  at  $x = 2.5$  cm showing the spread of the mixing layer, in terms of the velocity fluctuations. The features of the velocity profiles are discussed in detail in section 4.2.



(a)



(b)

Figure 3.6. R.M.S. profiles of  $u$  and  $v$  velocity components at (a)  $x = 2.5$  cm, and (b)  $x = 35$  cm from PIV-S and PIV.

### 3.4 Velocity-Density Correlations

From the time series of  $\rho$ ,  $u$ , and  $v$ , it is possible to compute velocity-density correlations (non-dimensionalized by  $\Delta\rho u_\infty$ ) such as shown in figure 3.8 (a). A packet of fluid lighter than the fluid immediately around it ( $\rho' = \rho - \bar{\rho} < 0$ ) will rise ( $v' > 0$ ), thus giving the negative peak of  $\langle \rho' v' \rangle$  at the centerline. Close to the splitter plate ( $x \sim 2.5$  cm), density and vertical velocity fluctuations are strongly correlated. As seen in figure 3.8(a), density fluctuations and horizontal velocity fluctuations  $\langle \rho' u' \rangle$  are weakly related close to the splitter plate. These trends are seen further downstream as well, where the mix-width is much wider due to diffusion (figure 3.8 (b)).

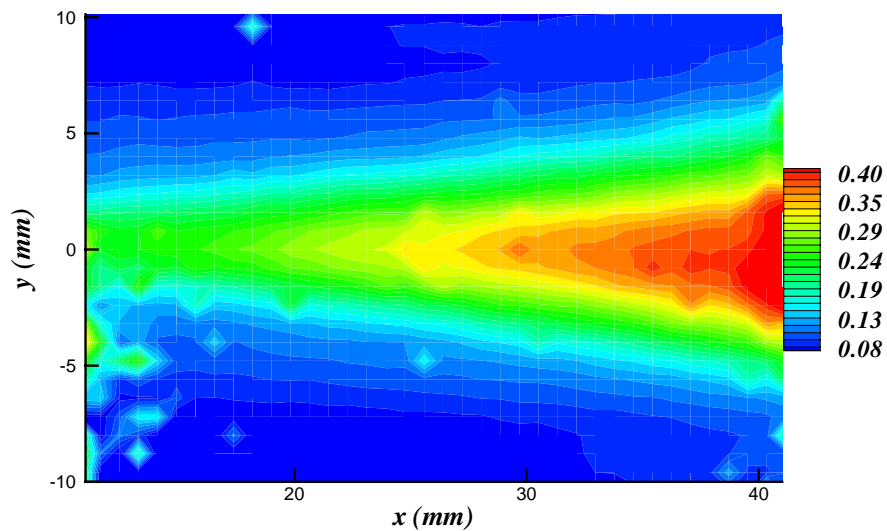
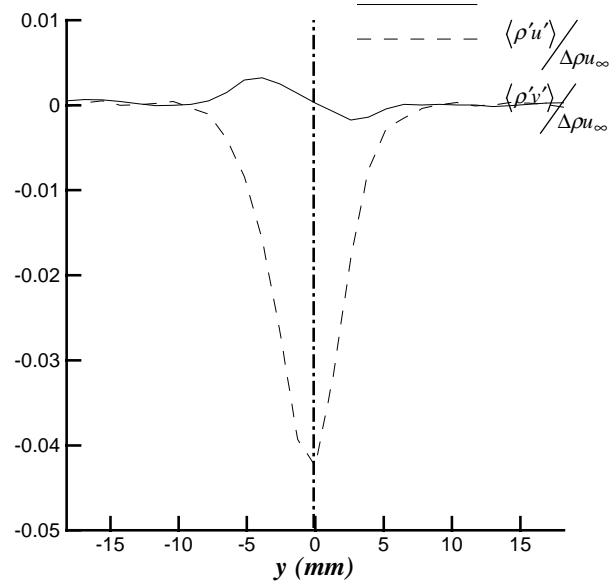


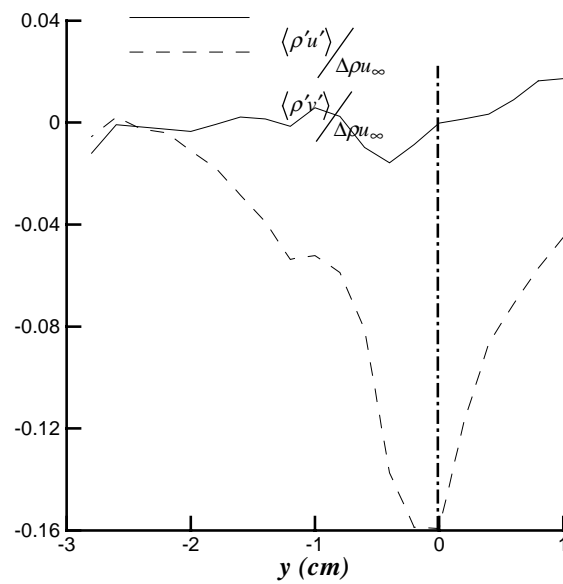
Figure 3.7. Contour map of  $v_{rms}/u_\infty$  at  $x = 2.5$ cm.

### 3.5 Error Analysis

The primary source of error in measuring reflected light intensity as an indicator of density stems from the non-uniformity of distribution of particles, even in a region of constant density; particles seemingly tend to clump together or pass through regions of varying light-sheet intensity. While computing statistical moments of even order, these and other uncertainties accumulate, resulting in residual errors as can be seen near the edge of the mixing layer in figure 3.2. (Note that far away from the mix zone,  $\rho_{rms}$  should  $\rightarrow 0$ , as  $y \rightarrow \infty$ , since there is no variation of density – turbulent or otherwise). To verify that these errors are inherent measurement errors, and not a result of lack of statistical convergence, a detailed convergence test was performed. Assuming that the errors in the density measurements are purely random, it can be shown (Mandel 1964) that the standard deviation of density (at the edge of the mix) fall on a  $\chi^2$  distribution, i.e., if from a series of samples, each of size  $N$ , we obtain the variances of density to be  $\sigma_1^2, \sigma_2^2, \sigma_3^2 \dots$ , then the  $\sigma_i^2$  will fall on a  $\chi^2$  distribution (it can also be shown that the true variance – obtained from an infinite sample – is the mean of the  $\sigma_i^2$ ). If ‘ $n$ ’ is the number of degrees of freedom in each sample, i.e.,  $n = N-1$ , then,



(a)



(b)

Figure 3.8. Profiles of,  $\langle \rho'u' \rangle / \Delta \rho u_\infty$  and  $\langle \rho'v' \rangle / \Delta \rho u_\infty$  at (a)  $x \sim 2.5$  cm downstream, (b)  $x \sim 35$  cm.

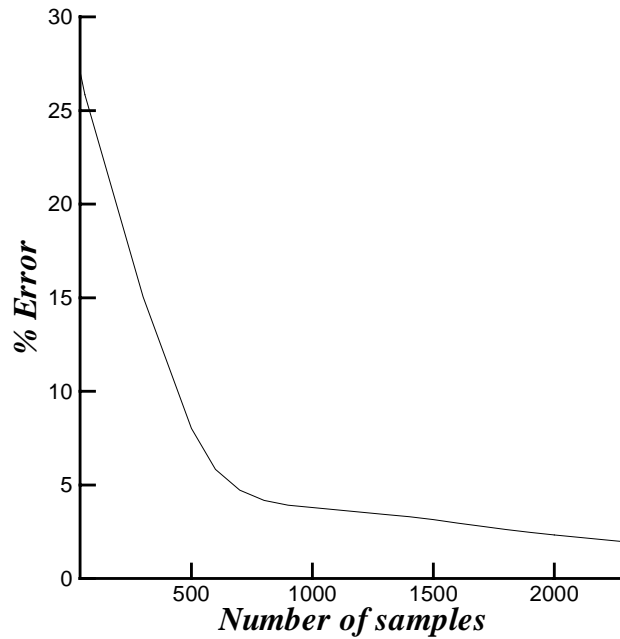


Figure 3.9. % r.m.s. error as a function of number of samples.

$$n \frac{\bar{\sigma}^2}{\sigma^2} = \chi_n^2 \quad (3.5.1)$$

where  $\chi_n^2$  is the  $\chi^2$  function based on  $n$  degrees of freedom. Thus, for a given  $n$ , we may determine the ratio  $\frac{\bar{\sigma}^2}{\sigma^2}$  from the  $\chi^2$  distribution, and hence the error in determining  $\rho$ .

Figure 3.9 shows the % error in determining  $\rho$  at the edge of the mix as a function of the sample size (for a confidence level of 95%). The turnaround at  $N \sim 1000$  is also confirmed by experimental data, and it can be concluded that the errors observed here are purely a result of inherent randomness of the measurement process. Note that the

requirements for convergence may be more severe along the center line, particularly further downstream, as the coherent structures grow in size increasing their turnover time, thus necessitating longer time averages.

The size of the interrogation window used also affects the r.m.s. value. The argument used here in picking the window size of 24x24 pixels is similar to the argument that the ‘continuum hypothesis’ is based on. If the window is too small, the local spatial average is unreliable since it is based on too few realizations. If the window is too large, then we may be averaging over real changes of the field variable. Thus, the window size was chosen in the region of the plateau in figure 3.10, so that the computed averages are not dependent on the size of the interrogation window. From a spatial convergence test (Ramaprabhu and Andrews 2003<sup>a</sup>), the molecular mix values were also found to be reasonably constant for window sizes between 16 and 32 pixels. For windows smaller than 16 pixels, the  $\theta$  values were found to approach two-fluid values due to lack of sufficient samples for averaging (figure 3.11).

By seeding the hot and cold water streams with different concentrations of particles, a measure of the local density has been obtained. This technique requires no modifications to a standard PIV system and does not require additional cameras or optical filters. Since the measurements are of a density indicator (i.e., concentration of particles), and not the actual density or temperature at a point, no calibration is necessary. For this same reason, PIV-S is not limited to a particular range of temperatures or densities. Thus, we have



tried to show the proof-of-principle of this technique for such measurements. The primary limitation of PIV-S technique is its poor spatial resolution of density measurements. A 24x24 pixel averaging window, such as the one used here, limits the spatial resolution of the technique to 1 mmx1mm. Thus, wave number spectra of density fluctuations smaller than this cannot be reliably computed, unless much smaller window sizes are used. The accuracy of this method is of the order of 90% for r.m.s. values of the density. We point out that this method is limited to flows that are not continuously stratified. In such cases, it is not immediately apparent how to “assign” a particular value of particle concentration to a local density value. Also, while the effect of refractive index fluctuations on the PIV results were found to be insignificant here, such effects may have to be taken into consideration when applying this technique to higher density-difference applications. It is expected that computing third order moments,  $\langle \rho'^2 v' \rangle$ ,  $\langle \rho'^2 u' \rangle$ ,  $\langle \rho' u' v' \rangle$  etc. will be a straightforward extension of the methods used here. Also, these higher-order moments will not introduce additional errors and will have the same accuracy as the r.m.s. measurements reported here. This is not true for 4<sup>th</sup> order moments where, once again, random errors do not vanish. Finally, using holographic techniques, such as Holographic Particle Velocimetry, which record the positions of seed particles in 3D space, it is conceivable that 3D measurements of the density field and its correlation with the velocity field may be measured.

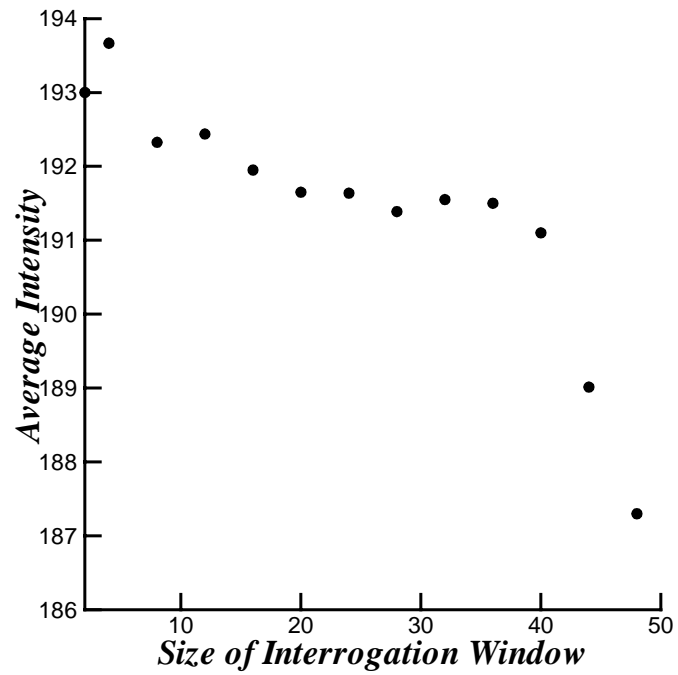


Figure 3.10. Average intensity within an interrogation window as a function of the window size in pixels.

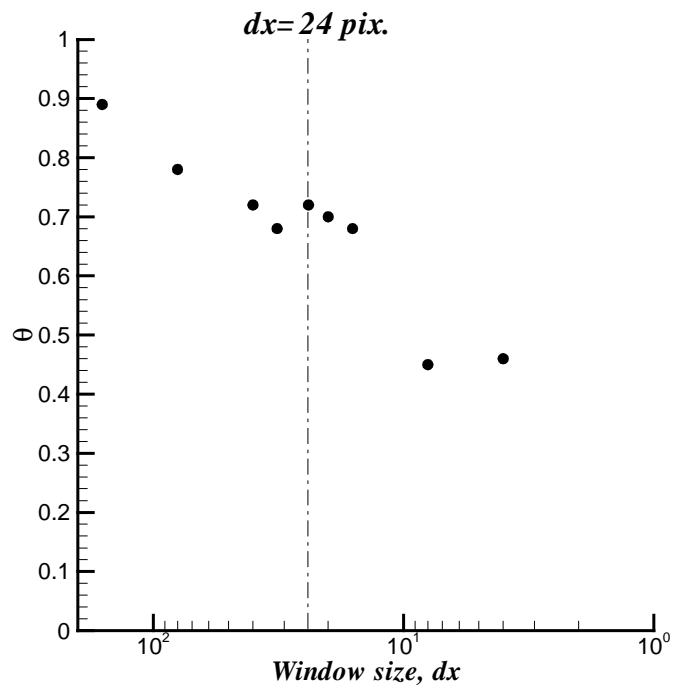


Figure 3.11. Molecular mix fraction  $\theta$  as a function of the window size in pixels.

## 4. EXPERIMENTAL RESULTS

### 4.1 Preliminaries

The subsequent sections contain a discussion of velocity and density data (spectral and statistical) obtained using the experimental diagnostic techniques described in sections 2.2, 2.3 and 3.1. High-resolution ( $\Delta x = \Delta y = 0.03$  cm) velocity data were collected at a sampling rate of 30 Hz at 2 cm and 35 cm downstream from the splitter plate. Thus, the smallest length scales captured with this technique are  $\sim 0.06$  cm. The accuracy of the velocity measurements reported here is  $\sim \pm 0.05$  cm/s. The data collected just off the splitter plate, at 2 cm, represent the initial conditions of the flow. The fine-mesh screen at the edge of the splitter plate creates a “grid-type” turbulence, with a spectrum of velocity perturbations in its wake. At 35 cm downstream, the hot and cold fluids are well mixed and the flow has reached an observed self-similar state. The data presented here describes the more fully developed R-T mix. In addition, lower resolution ( $\Delta x = \Delta y = 0.2$  cm) velocity data were collected at  $x$ -locations ranging from 0 to 56 cm from a series of experiments each with a window size of 8 cm x 6 cm (Table 4.1). The data-sampling rate used in these lower resolution experiments was 15 Hz, and these velocity fields were primarily used for computing the statistics at these locations. The small velocity scales that are not resolved by this set of experiments contribute little to the statistics here because of their small amount of energy.

Following Dalziel *et al.* (1999), we define a dimensionless time

	<b><i>x</i> – location (cm)</b>	<b><i>T</i> - location</b>	<b><i>y</i> – location (cm)</b>	<b>Resolution</b>
Thermocouple	1.0	0.03	0.0	$\Delta t = 0.01$ s
	2.0	0.07	0.0	
	10.0	0.34	0.0	
	20.0	0.70	0.0	
	30.0	1.00	0.0	
	40.0	1.39	0.0	
	50.0	1.74	0.0	
	60.0	2.08	0.0	
PIV (low resolution)	0.0 – 8.0	0 – 0.305	-3.0 – 3.0	$\Delta t = 0.066$ s $\Delta x = \Delta y = 0.2$ cm
	8.0 – 16.0	0.305 – 0.610	-3.0 – 3.0	
	16.0 – 24.0	0.610 – 0.916	-6.0 – 6.0	
	24.0 – 32.0	0.916 – 1.221	-9.0 – 9.0	
	32.0 – 40.0	1.221 – 1.527	-9.0 – 9.0	
	40.0 – 48.0	1.527 – 1.832	-9.0 – 9.0	
	48.0 – 56.0	1.832 – 2.137	-9.0 – 9.0	
PIV (high resolution) PIV-S	2.0	0.07	0.0	$\Delta t = 0.033$ s $\Delta x = \Delta y =$ 0.03 cm
	35.0	1.21	0.0	

Table 4.1. List of thermocouple and PIV/PIV-S experiments

$$T = t \left( \frac{A_t g}{H} \right)^{1/2} = \frac{x}{U} \left( \frac{A_t g}{H} \right)^{1/2}. \quad (4.1.1)$$

Here, the downstream distance  $x$  is converted to time  $t$ , using the Taylor hypothesis,  $t = x/U$ . The definition of  $T$  incorporates the self-similar nature of the flow (here,  $g$  is the acceleration due to gravity,  $x$  is the downstream distance,  $U$  is the mean convective velocity, and  $H$  the depth of the channel). In self-similar units, the two locations  $x = 2$  cm and  $x = 35$  cm (where the high-resolution data were collected) correspond to  $T = 0.07$  and 1.21, respectively. The early- and late-time PLIF images from figure 2, were taken at  $T \sim 0 - 0.305$  and  $T \sim 1.22 - 1.52$  respectively. The low-resolution PIV experiments were performed at  $0 < T < 2.1$ . The mix width plots of Dalziel *et al.* (1999) show a quadratic growth for  $T > 1$ , indicating the onset of self-similarity. Temperature data were collected by thermocouples along the centerline of the mix at 8 downstream locations (the location of the centerline was determined by the false positioning method described in section 2.3). These locations correspond to  $0.03 < T < 2.08$ . In all of the experiments presented here, care was taken to eliminate shear between the two fluid streams. Table 4.1 is a summary of all the experiments reported in this paper.

The molecular mix  $\theta$  (defined in section 3.2) affects the overall growth rate of the mix in the following way. Consider the definitions of  $B_0$  and  $B_2$  as the non-dimensional turbulent density fluctuations in the presence and absence of molecular diffusion respectively. Then,

$$B_0 = \overline{\rho_0'^2} / \Delta\rho^2, \quad B_2 = f_1 f_2 = \overline{\rho_2'^2} / \Delta\rho^2, \quad (4.1.2)$$

where the  $\overline{\rho_0'^2}$  and  $\overline{\rho_2'^2}$  refer to the turbulent density fluctuations for the miscible and 2-fluid cases respectively, and  $\Delta\rho = \rho_1 - \rho_2$ . Equation (1.2.1) for the growth rate of the mix may be rewritten using the modified driving term  $2\sqrt{\overline{\rho_0'^2}}$

$$h = 2gt^2\alpha\sqrt{\overline{\rho_0'^2}}/(\rho_1 + \rho_2). \quad (4.1.3)$$

This is a more natural choice for molecularly mixed fluids, since the density difference available to drive the flow  $\Delta\rho = \rho_1 - \rho_2$  is reduced in the presence of diffusion. For a 2-fluid case at the centerline where  $f_1 = f_2 = 0.5$ , then

$$\overline{\rho_0'^2} = \overline{\rho_2'^2} = f_1f_2\Delta\rho^2 = (\rho_1 - \rho_2)^2 / 4, \quad (4.1.4)$$

so that equation (4.1.3) reduces to equation (1.2.1).

For miscible fluids, we have

$$\frac{\overline{\rho_0'^2}}{\overline{\rho_2'^2}} = \frac{B_0}{B_2} = 1 - \theta. \quad (4.1.5)$$

reducing equation (4.1.3) to (Andrews 2001)

$$h = \tilde{\alpha} A_t gt^2, \quad (4.1.6)$$

where  $\tilde{\alpha} = \alpha\sqrt{1-\theta}$  is an effective growth constant. At the centerline of the mix, measurements of  $\theta$  have been found to vary from 0.7 to 0.8 (Wilson & Andrews 2002), and remain reasonably constant across the mix (see below). Assuming an intermediate value of  $\theta = 0.75$ , the presence of molecular diffusion serves to reduce the growth rate of the mix by a factor of 0.5. The front tracking calculations of Glimm *et al.* (2001) suggest 2-fluid value for  $\alpha$  of 0.07, giving a net growth constant  $\tilde{\alpha} = 0.5\alpha = 0.035$ . This is consistent with the value reported by most numerical simulations that have molecular diffusion in them.

The centerline time-evolution of the mix-parameters defined in section 3.2 and determined from the thermocouple measurements, are shown in figure 4.1. Close to the

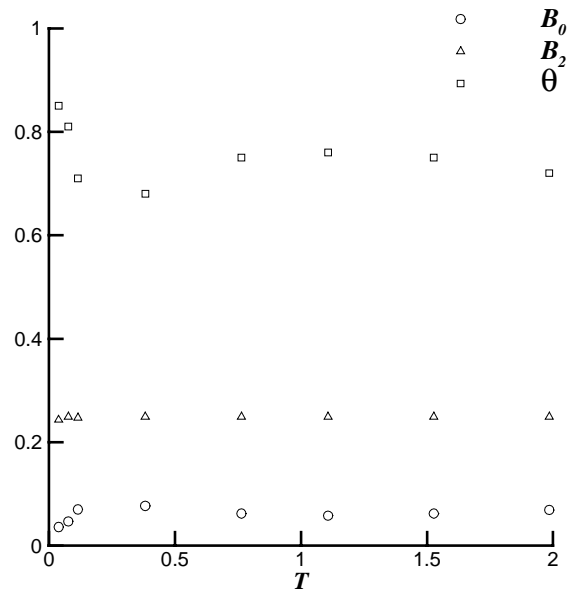


Figure 4.1. Time evolution of scalar turbulence intensity and mix parameters measured at the centerline.

splitter plate ( $T \sim 0.034$ ), the mixing layer is diffuse and, as a result,  $\theta$  values are high in this region (and corresponding  $B_0$  values are low). As the mix develops farther downstream, the fluctuation levels increase with the onset of the instability, resulting in a slight drop in the value of  $\theta$ . This corresponds to the stretching of the initial diffuse layer, followed by rolling up into mushroom-shaped structures. This is also seen in the p.d.f.s of density values (figure 4.2), which switch from an initial distribution with a single peak ( $T = 0.034$ ) suggesting a diffuse region, to a distinctly bimodal distribution at later times ( $T = 0.347$ ), indicating fluctuating density fields. Eventually ( $T = 1.008$ ), turbulent diffusion serves to smooth out some of these fluctuations, and the histogram regains a dominant peak corresponding to  $(\rho - \rho_2)/(\rho_1 + \rho_2) = 0.5$  at the center of the mix. As expected, the 2-fluid parameter  $B_2$  remains relatively constant at a value of 0.25. This further confirms that these measurements were indeed at the centerline of the mix, since at the center  $f_1 = f_2 = 0.5$  and  $B_2 = 0.25$  according to equation (3.2.1). It is noteworthy that all the parameters change little in the developing self-similar regime of the mix ( $T > 1$ ).

In section 3.2, we argued that PIV-S accurately captures  $\theta$  at the centerline, due to the preponderance of small-scales at that location. We attempt to quantify this by defining an appropriate intermittency factor  $\gamma$ . A common definition of intermittency focuses on the vorticity in the fluid,  $\gamma_\omega$ , i.e., rotational fluid is marked as turbulent fluid, and irrotational fluid is marked as quiescent. An intermittency function,  $I$ , based upon vorticity is defined as (Pope 2000)



$$I(y, t) = H(|\omega(y, t)| - \omega_{\text{threshold}}), \quad (4.1.7)$$

where  $\omega$  is the out-of-plane component of the local vorticity field,  $\omega_{\text{threshold}}$  is a small positive threshold, and  $H$  is the Heaviside function. Thus  $I$  is 1 for  $|\omega| > \omega_{\text{threshold}}$  and zero otherwise. The intermittency factor is then given by

$$\gamma_{\omega}(y) = \langle I(y, t) \rangle, \quad (4.1.8)$$

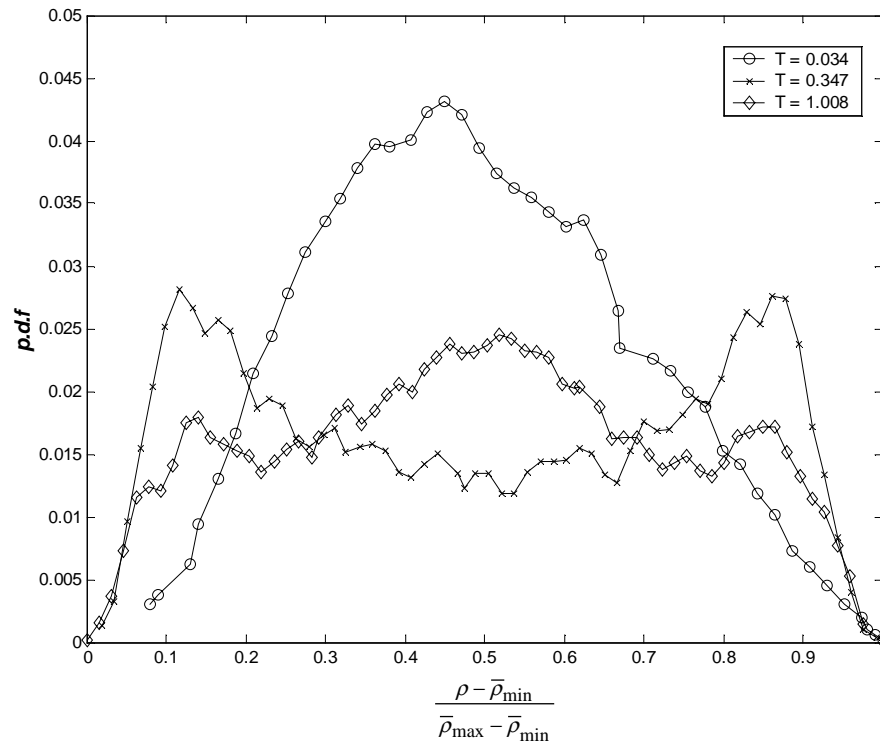
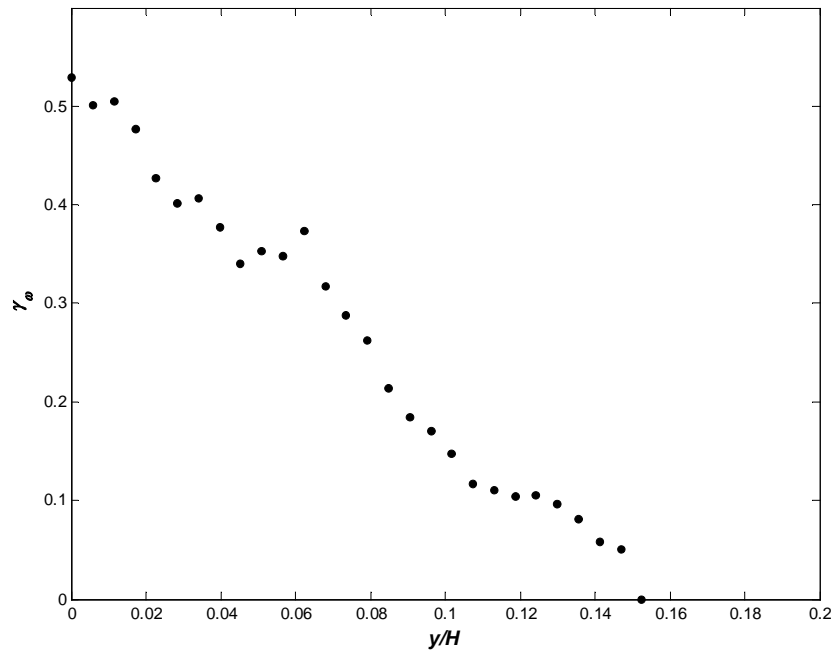
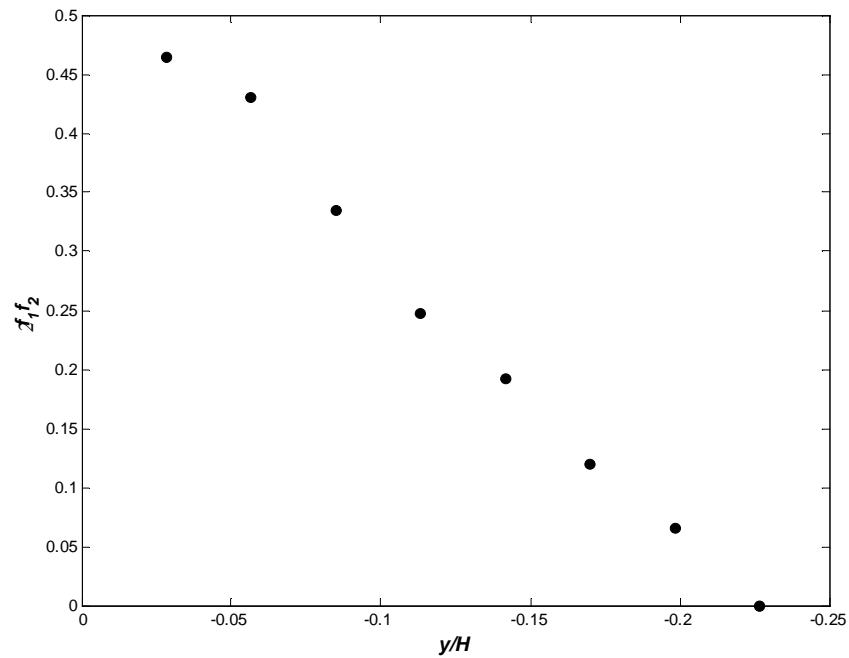


Figure 4.2. p.d.f.s of centerline non-dimensional density at 3 different times.



(a)



(b)

Figure 4.3. (a) Intermittency factor  $\gamma_\omega$  (based on a vorticity threshold) and (b) intermittency factor (based on the two-fluid parameter  $B_2$ ) across the mix at  $T = 1.21$ .

where  $\langle \bullet \rangle$  indicates time-averaging. For the present experiment, the cross-stream profile of  $\gamma_\omega$  is shown in figure 4.3 (a) for  $T = 1.21$  ( $\omega_{threshold}$  was chosen so that  $\frac{\omega_{threshold}^2}{\langle \omega \rangle^2}$  was  $\sim 5\%$ ). Unlike shear layers and wakes, where  $\gamma_\omega$  can reach a maximum value of 1 at the centerline (LaRue & Libby 1976), the intermittency factor reaches a peak value of 0.5 in our buoyancy driven mix. This is due to significant cross-stream transport of rotational and irrotational fluid, thus decreasing the value at the centerline. However, this picture is incomplete, as we will show in the following. For our purposes, we are interested in identifying the interface between the heavy and light fluids. Therefore, a more natural definition for the present buoyant mixing is an intermittency factor (or a density intermittency factor) based on the volume fraction.

We take  $f_{threshold} = 0.5$  as the threshold for defining a density intermittency factor. Then, using the Heaviside function and instantaneous volume fractions  $f'_1 = \frac{\rho - \rho_2}{\rho_1 - \rho_2}$ ,

$f'_2 = 1 - f'_1$ , we may define

$$N^+(y, t) = \mathbf{H}(f'_1(y, t) - f_{threshold})$$

$$N^-(y, t) = \mathbf{H}(f_{threshold} - f'_2(y, t)).$$

Hence  $\langle N^+(y, t) \rangle$  and  $\langle N^-(y, t) \rangle$  denote the probability of finding fluid 1 and 2, respectively, at  $y$ ; thus,  $\langle N^+(y, t) \rangle \equiv f_1$ , and  $\langle N^-(y, t) \rangle \equiv f_2$  by definition of volume

fraction. Any definition of density intermittency will have to include the volume fraction of the fluid, which can be interpreted as a conditional measure of the density of the fluid and be symmetric about the centerline of the mix. This may be accomplished by defining a density intermittency factor as

$$\gamma_\rho = \frac{1}{2} \left( 1 - \left( \langle N^+(y,t) \rangle - \langle N^-(y,t) \rangle \right)^2 \right) = \frac{1}{2} \left( (f_1 + f_2)^2 - (f_1 - f_2)^2 \right), \quad (4.1.9)$$

using  $f_1 + f_2 = 1$ . In the above the  $f_{threshold}$  term is eliminated when the Heaviside operation is performed. This definition ensures that  $\gamma_\rho$  reaches a peak value of 0.5 at the centerline where  $f_1 = f_2 = 0.5$  and goes to zero at the edges where  $f_1 = 1 - f_2 = 0$  and vice-versa. After some algebraic manipulation, equation (4.1.9) simplifies to

$$\gamma_\rho = 2f_1f_2 = 2B_2. \quad (4.1.10)$$

Thus, a  $\gamma_\rho$  value of zero implies the presence of a single fluid (not necessarily irrotational), and a value of 0.5 indicates that both fluids are present with equal probability (i.e., a large amount of density intermittency). Figure 4.3 (b) plots  $\gamma_\rho$  as a function of  $y/H$  at  $T = 1.21$  and shows a peak value of 0.5 at the centerline. This indicates the presence of a large amount of density intermittency as well as associated interfacial area at the centerline with a value approaching the single-fluid limit at the edge of the mix. Thus, the structures at the centerline are much more contorted, with greater interfacial area resulting in molecular diffusion across the interface, as shown in figure 1.2 (b).

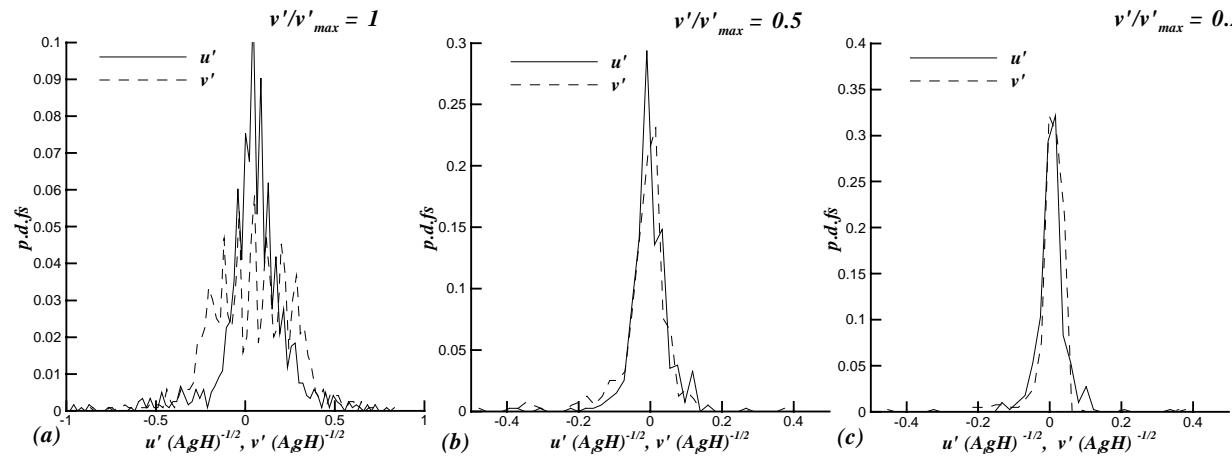
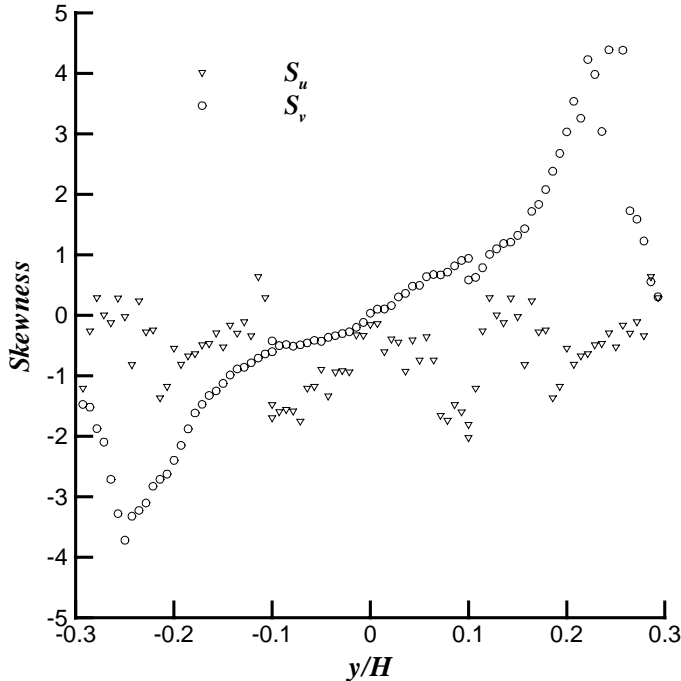


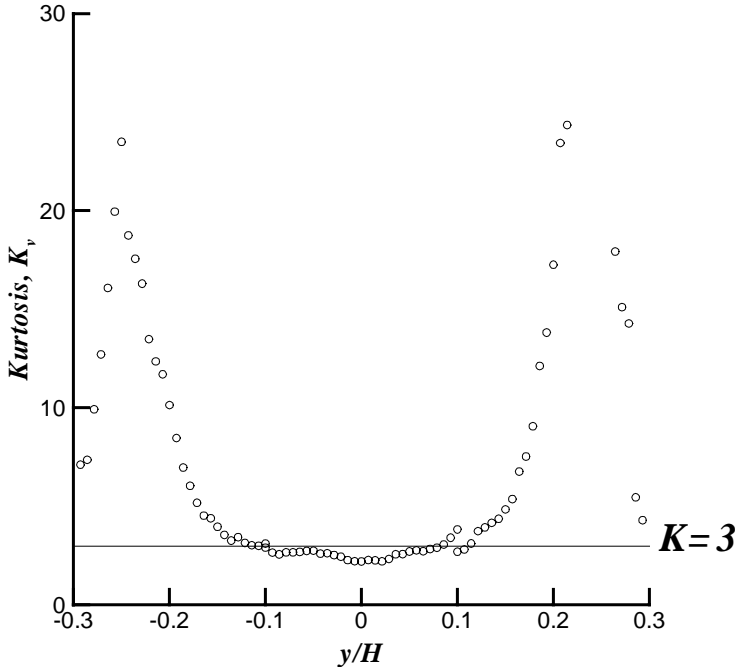
Figure 4.4. p.d.f.s of vertical and horizontal velocities at three locations across the mix.

(a)  $\frac{v'}{v'_{max}} = 1$ , (b)  $\frac{v'}{v'_{max}} = 0.5$ , (c)  $\frac{v'}{v'_{max}} = 0.2$  corresponding to  $y/H = 0, 0.13$ , and  $0.2$  respectively ( $T = 1.21$ ).

These observations are also supported by velocity p.d.f.s at  $T=1.14$  for three locations across the mix: at points where  $\frac{v'}{v'_{max}} = 1, 0.5,$  and  $0.2$  corresponding to  $\frac{y}{H} = 0, 0.13,$  and  $0.2$  respectively (figures 4.4 (a), (b) and (c), respectively) with  $v'_{max}$  available from figure 4.8 (b). The resolution in all three figures is the same, i.e., the number of intervals across the dynamic range of the velocities is constant. At the center of the mix, where  $\frac{v'}{v'_{max}} = 1,$  the vertical velocity distribution is flatter than the horizontal velocity components and covers a wider range of scales; thus, the likelihood of finding large velocities is roughly the same as that of finding small velocities. This implies that there is a greater hierarchy of scales at the center of the mix, resulting in a greater interfacial area and hence enhanced mixing. Approaching the edge of the mix with  $\frac{v'}{v'_{max}} = 0.5$  and then  $0.2,$  for both the horizontal and vertical components, small velocities become more likely than large ones. In addition, the vertical velocity p.d.f.s become more skewed and less Gaussian near the edge for reasons explained by considering the skewness below.



(a)



(b)

Figure 4.5. Skewness (a) and Kurtosis (b) profiles across the mix at  $T = 1.21$ .

The third and fourth moments of the velocity field represent the skewness and flatness (kurtosis) of the velocity probability density functions. These functions are conventionally normalized by the velocity r.m.s.:

$$S_u = \frac{\langle u'^3 \rangle}{\langle u'^2 \rangle^{3/2}}, S_v = \frac{\langle v'^3 \rangle}{\langle v'^2 \rangle^{3/2}}, K_u = \frac{\langle u'^4 \rangle}{\langle u'^2 \rangle^2}, K_v = \frac{\langle v'^4 \rangle}{\langle v'^2 \rangle^2}, \quad (4.1.11)$$

where  $\langle u'^2 \rangle$  and  $\langle v'^2 \rangle$  profiles are given in figures 4.8 (a) and (b) respectively. Cross-stream profiles of the skewness and kurtosis of the horizontal and vertical velocity distributions are shown in figures 4.5 (a) and (b), respectively.  $S_u$  is close to zero across the mix, since the horizontal velocity field is symmetric about the vertical. However,  $S_v$  is zero at the centerline and antisymmetric about it. Alternately, the predominant velocity determines the sign of skewness, because of the third power. It can be noted that  $S_v > 0$ , for  $y > 0$ , as fluid is predominantly rising (the upper edge of the mix), whereas  $S_v < 0$  for  $y < 0$  as fluid is predominantly falling (lower edge of the mix). Neglecting the horizontal velocities, which cancel out due to symmetry, mass conservation for the mix considered as a 2-phase fluid gives  $f_1 v_1 + f_2 v_2 = 0$ , where  $f_1, f_2$  and  $v_1, v_2$  are the volume-fraction and the vertical velocity components of the heavy and light fluids, respectively. At the centerline,  $f_1 = f_2 = 0.5$  and  $v_1 = -v_2$ , resulting in a symmetric p.d.f. and  $S_v = 0$ . At the edge,  $f_1 \rightarrow 1$  (and  $f_2 \rightarrow 0$ )  $v_1$  is a small negative velocity while  $v_2$  is a large positive velocity. Conversely, as  $f_1 \rightarrow 0$ ,  $v_1$  is a large negative velocity and  $v_2$  has a small positive value. Thus, the vertical velocity skewness profile is zero at the centerline, with positive values for  $y > 0$  and negative values for  $y < 0$ . (Beyond the edge of the mix, the skewness drops to zero due to the presence of random noise).



The fourth moment of velocity, the Kurtosis, is shown in figure 4.5 (b). For a Gaussian p.d.f., the skewness is zero and the kurtosis approaches a value of three. In the present case, the vertical component  $K_v$  approaches the Gaussian value ( $K = 3$ ) at the centerline and is highly non-Gaussian at the edges. This is in agreement with the skewness data,

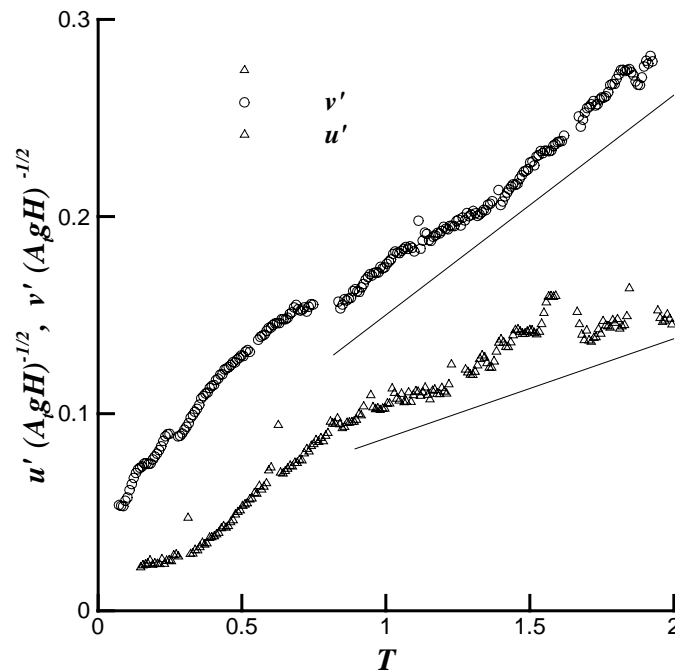


Figure 4.6. Centerline vertical and horizontal velocity *r.m.s.* as a function of non-dimensional time.

which also show Gaussian behavior at the center, and a non-Gaussian trend at the edges. The symmetric profile of  $K_v$  arises from taking the fourth power of the velocity fluctuations. The  $u$ -component has considerable jitter across the mix, which are

amplified when raised to the fourth power and hence is not shown in figure 4.5 (b). We conclude that the presence of both fluids with equal probability, associated with a high intermittency factor, and the hierarchy of scales, both contribute to the enhanced mixing measured at the centerline.

#### 4.2 Statistics

From the low resolution PIV experiments described earlier in this section and listed in Table 4.1, the centerline r.m.s. values of the vertical,  $v'$ , and horizontal,  $u'$ , velocity components at locations  $0 < T < 1.8$  are shown as a function of time in figure 4.6. The  $v'$  values, after an initial period of exponential growth ( $T < 0.5$ ), grow linearly with time in the self-similar region (However, it is not clear if the condition for exponential growth of initial disturbances,  $h_\lambda \ll \lambda$  is satisfied in these experiments). The centerline vertical velocity normalized by  $\sqrt{A_t g H}$  reaches a peak value of 0.28 at  $T = 1.9$ . The vertical velocity at the centerline can be related to the mix width of equation (1.2.1) by

$$v' = \frac{dh}{dt} = 2\alpha A_t g t . \quad (4.2.1)$$

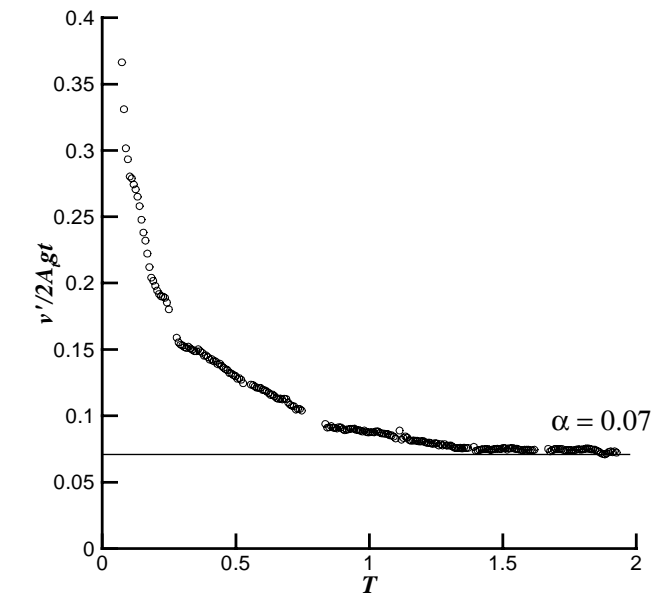
Note that (4.2.1) is valid only in the self-similar region of the flow. Thus, from the time evolution of  $v'$ , we can determine the growth constant  $\alpha$  by computing the ratio  $v'/2A_t g t$ . This ratio is plotted as a function of the non-dimensional time in figure 4.7 (a). The saturation of  $\alpha$  at late time to a constant value of 0.07 suggests that the flow reaches self-similarity in these experiments. This is an interesting result, as in the past we obtained the same value for  $\alpha$  of 0.07 in this experiment (Snider & Andrews 1994) by

measuring the half mix width  $h$  (based on the 5% and 95% threshold for the volume fraction) directly and relating it to  $\alpha$  through equation (1.2.1). Therefore, by using equation (4.2.1) and obtaining  $\alpha = 0.07$  from the centerline value of  $v'$ , we imply that the expansion of the mix is driven by velocity fluctuations that occur across the whole mix and not just the edge. This characterization is supported by observations of the mixing layer, shown in figure 1.2 (b), where large-scale structures span the mix and dominate the velocity fluctuations. As a result, many of the statistics presented in this work remain practically constant across the mix. Spectral analysis of the velocity fluctuations later provides further support for this interpretation of the mix dynamics.

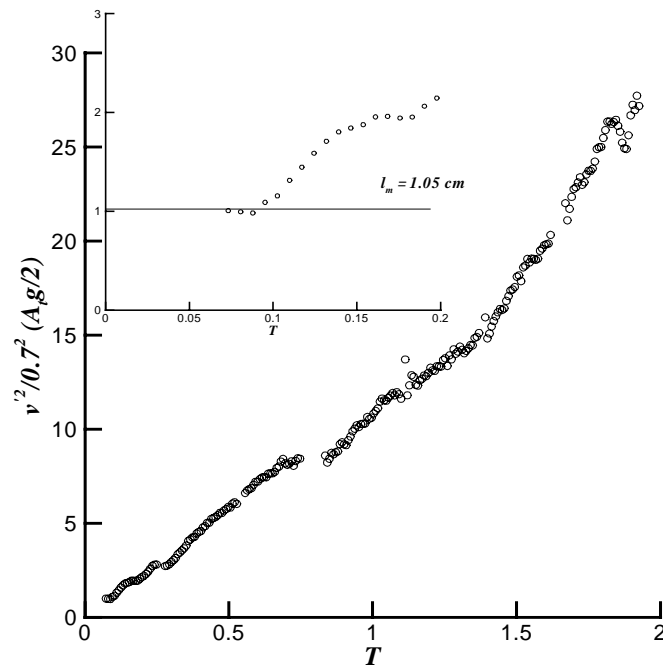
At early times, one may expect a single wavelength to dominate the dynamics. The centerline vertical velocity may then be approximated by the terminal velocity (Andrews & Spalding 1990), a natural extension of Layzer's terminal velocity formulation for  $A_t = 1$ ,

$$v' \sim 0.7\sqrt{A_t g l_m / 2}, \quad (4.2.2)$$

where  $l_m$  is the dominant growing wavelength. We may then determine the value of  $l_m$  in this flow by plotting  $v'^2 / (0.7^2 A_t g / 2)$  in figure 4.7 (b). The value of  $l_m$  thus obtained from the flat region close to the splitter plate (at  $0.07 < T < 0.12$ ) was 1.05 cm (figure 4.7 (b) inset); a peak in the velocity spectral data close to the inlet around this value further confirms the presence of a dominant wavelength at  $l_m \sim 1.05 \text{ cm}$  (Section 4.3). The appearance of the second plateau between  $T \sim 0.15$  and  $T \sim 0.2$  is believed to be the



(a)

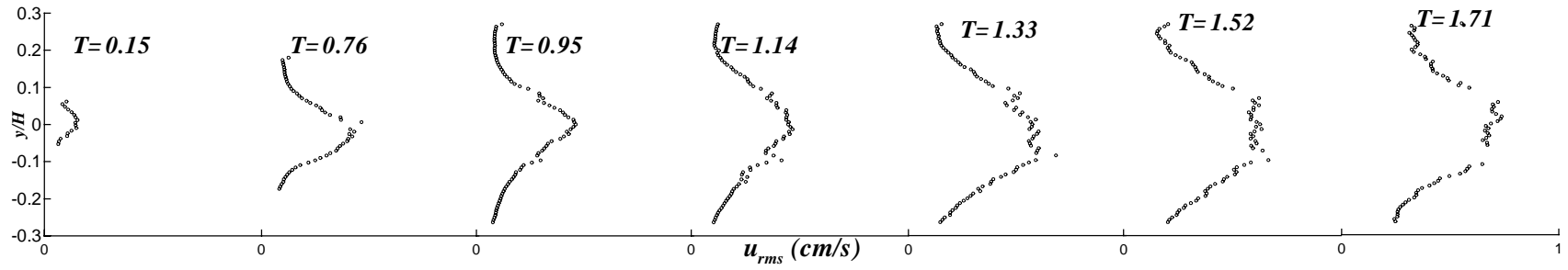


(b)

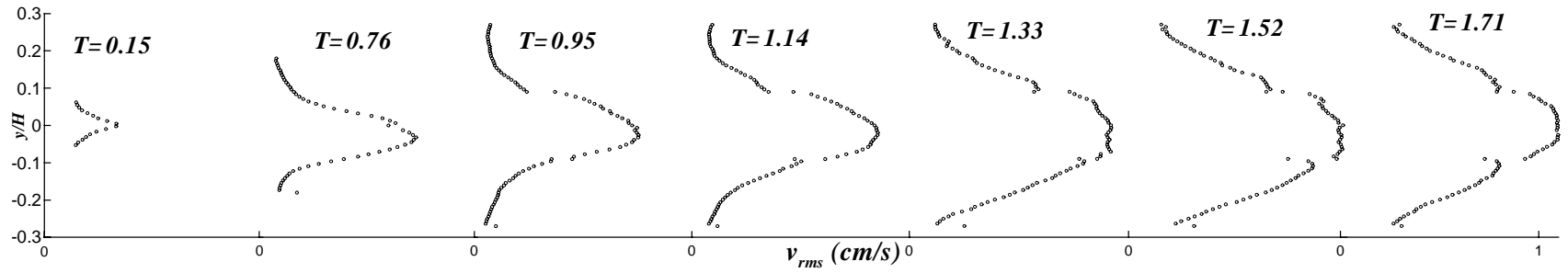
Figure 4.7. (a).  $\alpha = v'/2A_1gt$  at the centerline plotted as a function of  $T$  and (b)  $l_m = v^2/0.7^2 A_1g/2$  in cm at the centerline plotted as a function of  $T$ . Inset shows  $l_m$  close to the splitter plate.

result of pairing of these structures. At late time, the value of  $l_m$  reaches a maximum of  $\sim 27$  cm comparable to the channel depth of 30 cm, although it is no longer accurate to characterize the dynamics in terms of a single wavelength. Not surprisingly, the single-mode dynamics in this experiment are restricted to very early stages of the R-T development.

The cross-stream profiles of horizontal and vertical velocity fluctuations are shown in figures 4.8 (a) and (b), respectively. The velocity axes are retained in dimensional coordinates to give a sense of the relative magnitudes of the peak values as they evolve in time. Vertical velocity fluctuations dominate over the horizontal velocity component and provide most of the transport of mass, momentum, and energy. The figure indicates that for  $T > 0.76$ , the velocity profiles evolve in a shape-preserving manner and will collapse onto a single curve when normalized by the appropriate variables.



(a)



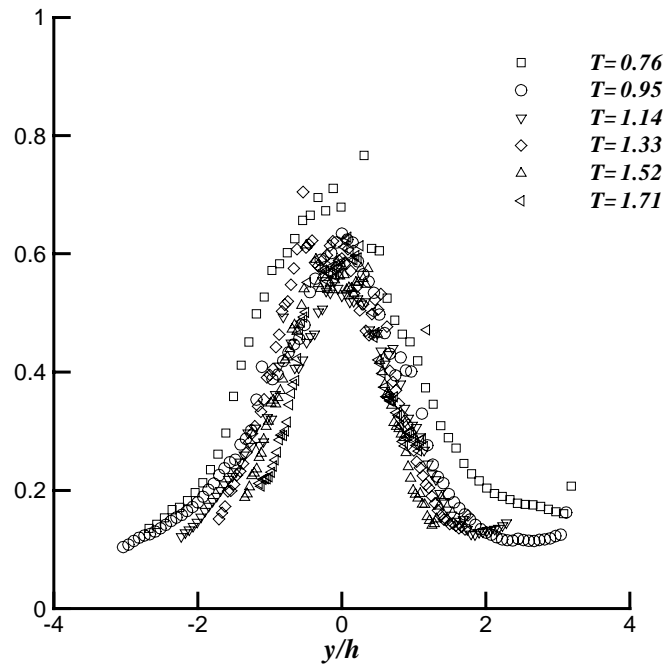
(b)

Figure 4.8. (a)  $u'$  profiles at different  $T$  – locations. (b)  $v'$  profiles at different  $T$ -locations.

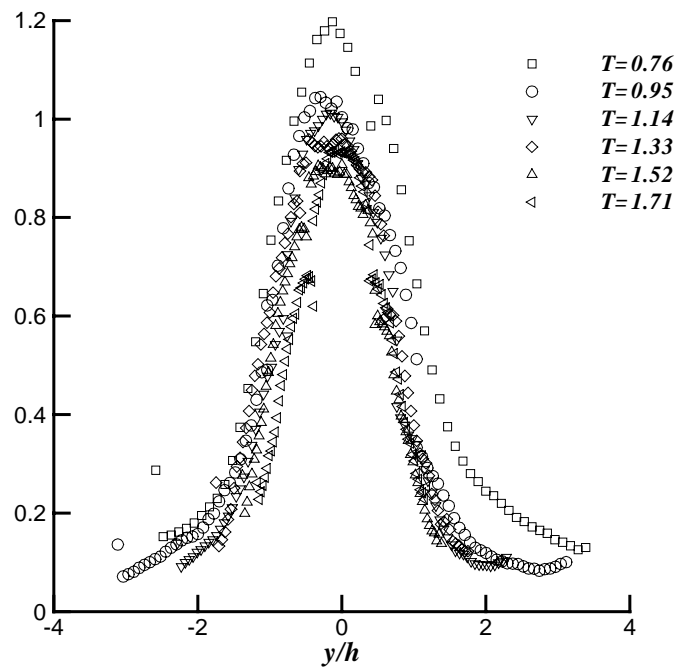
We normalize with the saturation velocity defined by  $u_\infty = 0.7\sqrt{A_t g h_x / 2}$ , where  $h_x$  is the local mix-width computed from  $h_x = \alpha A_t g t^2$  with  $\alpha = 0.07$ . Then,  $u_\infty$  and  $h_x$  are chosen as the self-similar scales and used to normalize the cross-stream velocity profiles in figure 4.8. The results for the horizontal and vertical velocity fluctuations are shown in figures 4.9 (a) and (b), respectively, and show a good collapse for all  $T$ - locations except  $T = 0.76$  where the flow may not be fully self-similar. The vertical velocities expressed in terms of the saturation velocity have a peak around 1, showing that this choice of the self-similar variable is appropriate and physically meaningful. Since there is no shear in this experiment,  $v'$  dominates over  $u'$  everywhere. This dominance decreases with downstream distance from a ratio  $\sim 2$  close to the splitter plate, to a ratio of  $\sim 1.6$  as the structures become more three-dimensional. Furthermore, by  $T=1.21$  the ratio  $\frac{v'}{u'}$  is almost constant across the mixing layer (figure 4.10), suggesting an existing equilibrium between the  $u'$ - and  $v'$ - kinetic energy production terms everywhere.

Ristorcelli (2001) suggested the large-scale anisotropy between  $u'^2$  and  $v'^2$  can also be characterized through the normalized anisotropy tensor,  $b_{ij}$ . A discussion on the geometry of the small scales is deferred until the section on velocity spectra. Following Pope (2000), the anisotropy tensor is defined as

$$b_{ij} = \frac{\langle u_i u_j \rangle}{\langle u_k u_k \rangle} - \frac{1}{3} \delta_{ij}, \quad (4.2.3)$$



(a)



(b)

Figure 4.9. (a)  $u'$  profiles at different  $T$ -locations expressed in self-similar units and (b)  $v'$  profiles at different  $T$ -locations expressed in self-similar units.



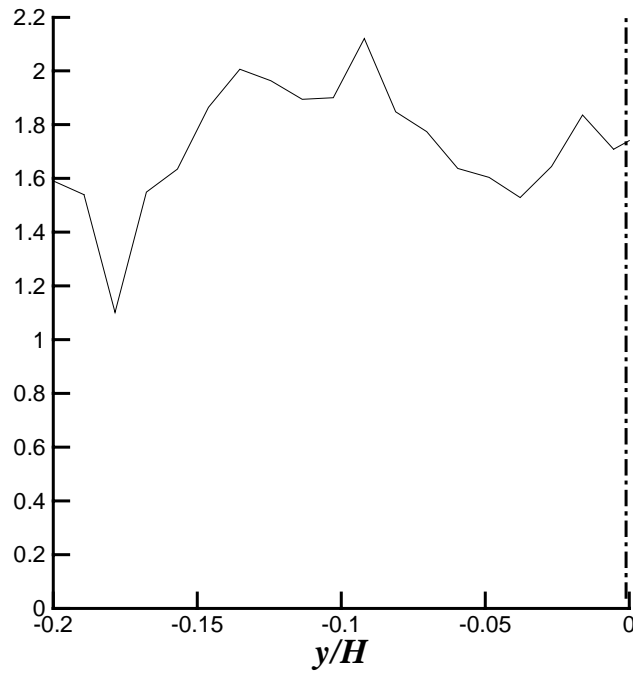
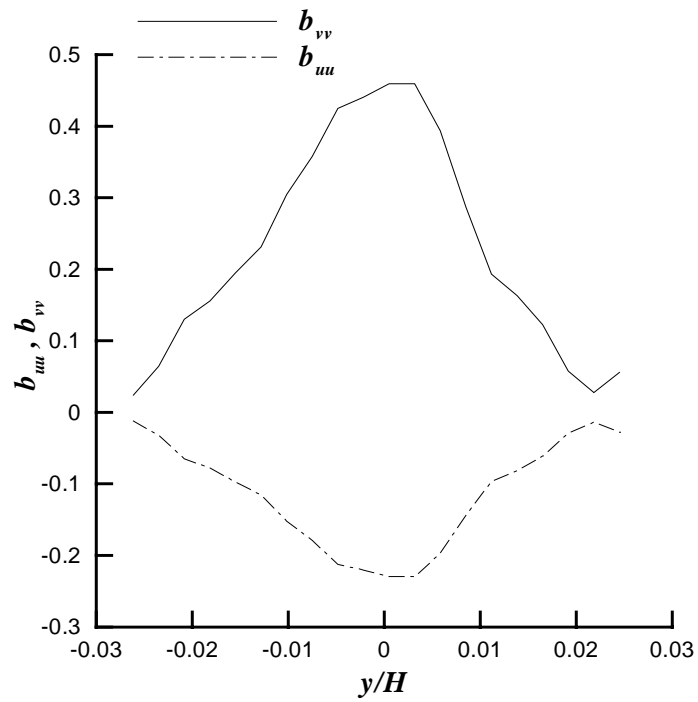


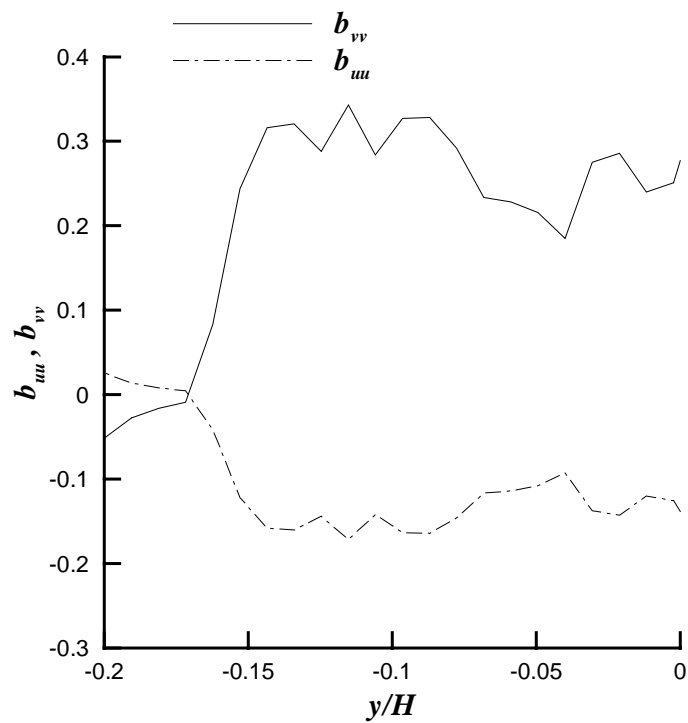
Figure 4.10. Ratio of  $v'/u'$  across the mix at  $T = 1.21$ .

where  $\delta_{ij} = 1$  for  $i = j$ , 0 otherwise, and  $\langle u_k u_k \rangle$  is twice the kinetic energy. Thus, this is the deviatoric part of the Reynolds stress tensor normalized by the kinetic energy term. Pope (2000) shows that the anisotropic stress tensor is responsible for the transport of turbulent momentum. In an R-T mix, the cross-correlation term  $\langle u' v' \rangle$  is negligible since the mushroom-shaped structures have left-right symmetry about the center, so  $u' v'|_{right} = -u' v'|_{left}$ . Similarly, for  $u$  and  $w$  components,  $\langle w' v' \rangle$  and  $\langle w' u' \rangle \sim 0$ . Thus,

$$\langle u_i u_j \rangle = \begin{pmatrix} \langle u'^2 \rangle & 0 & 0 \\ 0 & \langle v'^2 \rangle & 0 \\ 0 & 0 & \langle w'^2 \rangle \end{pmatrix}. \quad (4.2.4)$$



(a)



(b)

Figure 4.11. Profiles of the anisotropy tensor across the mix at (a)  $T = 0.07$ , and (b)  $T = 1.21$ .

In the above equation,  $\langle u'^2 \rangle$  and  $\langle v'^2 \rangle$  are measured, and  $\langle u'^2 \rangle = \langle w'^2 \rangle$  is taken from axisymmetry of the coherent structures. For isotropic turbulence,  $\langle u_i u_i \rangle / \langle u_k u_k \rangle = 1/3$  and so  $b_{ii} = 0$ . Also,  $-1/3 \leq b_{ij} \leq 2/3$ , where the upper and lower limits represent one-dimensional and two-dimensional distributions of turbulent kinetic energy, respectively. Thus,  $b_{ij}$  characterizes the geometry of the turbulence, independent of the amplitude of the fluctuations.

Figures 4.11 (a) and (b) are plots of the anisotropy tensor across the mix at  $T = 0.07$  and  $T = 1.21$ , respectively, where  $b_{uu}$  corresponds to the horizontal velocity component, and  $b_{vv}$  corresponds to the vertical velocity component. The velocity ratio profiles of figure 4.10, and anisotropy profiles shown in figure 4.11 are based on the high-resolution velocity data shown in figure 3.6. At both times, near the center of the mix, most of the transport appears to be in the vertical direction. Once again, we see that the statistics are reasonably constant across the mix at  $T = 1.21$ . It appears that at both locations  $b_{ii} \rightarrow 0$  near the edges of the mix, which is attributed to the decay of turbulent fluctuations in this region rather than any inherent local isotropy. At  $T = 0.07$ , the drop off near the edges is more gradual, suggesting the presence of a viscous diffusive layer. Thus, it appears that the mix at the end of the splitter plate consists of a central region where buoyancy dominates padded by viscous layers at both the top and bottom. The geometry of the small scales is discussed in the next section.

### 4.3. Spectra

To study the structure of small-scales, velocity and density spectral data are presented in this section in the wavenumber domain. The velocity spectra were computed by extracting a velocity timeseries at the centerline at certain spatial locations, and then calculating the power associated with the (mean-subtracted) signal in the Fourier domain. To compare with the wavenumber spectra obtained directly from spatial variations in the velocity field, the temporal data have been converted to spatial data first using the Taylor hypothesis, and the spectra then computed in the wavenumber domain. Similarly, density fluctuation spectra have been computed from the temperature timeseries (converted to spatial data) obtained from thermocouple measurements. The density data obtained from the equation of state, are first non-dimensionalized to give  $\rho^* = (\rho - \rho_2) / (\rho_1 - \rho_2)$ . Then, the scalar energy spectra are computed using the equation

$$E_{\rho'}(k) = \frac{2\Delta x}{N} \left| \sum_{i=0}^{N-1} \rho^*_i e^{2\pi j k x_i} \right|^2, \quad (4.3.1)$$

where  $N$  is the number of samples,  $\Delta x = U\Delta t$  is the sampling interval, and  $j = \sqrt{-1}$ .

Thus, the scalar energy spectrum is the wavenumber representation of  $B_0$ , i.e.,

$$\int_0^{\infty} E_{\rho'}(k) dk = B_0.$$

The non-dimensional energy spectra of density fluctuations  $E_{\rho'}(k)H^{-1}$ , at  $T = 0.034$  ( $x \sim 1$  cm) is shown in figure 4.12 (a). The corresponding compensated energy spectrum

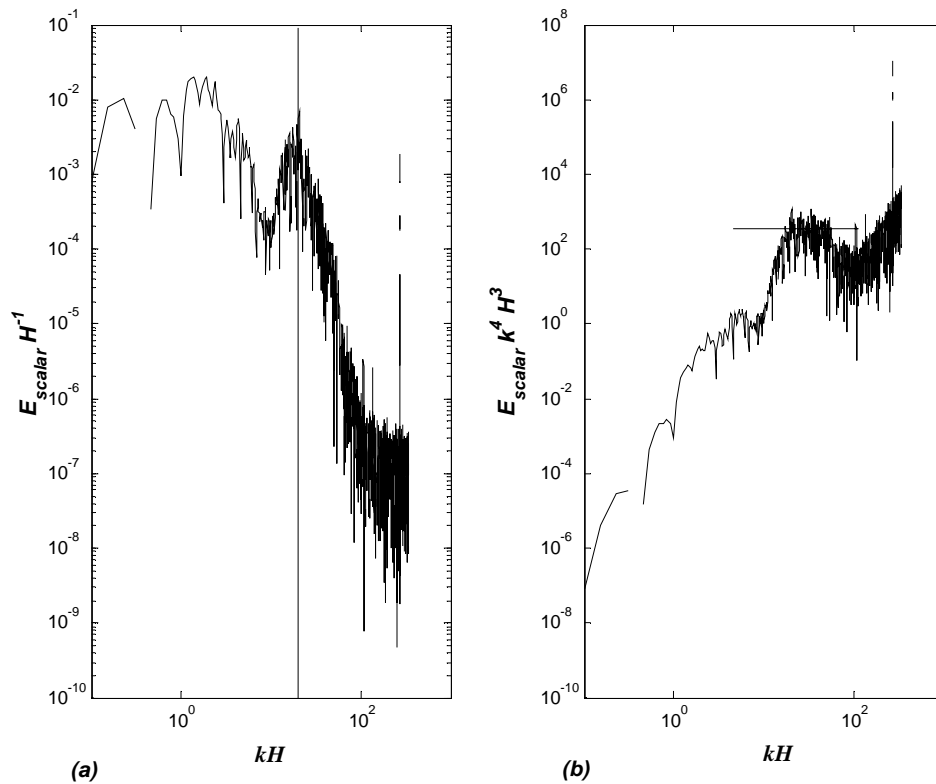


Figure 4.12. Density fluctuation spectrum (a) at  $T = 0.034$  at the centerline. Dashed line represents  $kH = 20$ . (b) Compensated fluctuation spectrum  $k^4 E(k)$ . Solid line represents the horizontal.

$k^4 E_{\rho'}(k)$  (normalized as  $k^4 E_{\rho'}(k) H^3$ ) is plotted in figure 4.12 (b). The factor  $k^4$  is used to illustrate regions with a slope of  $-4$ , which will appear horizontal in the compensated spectrum. Inspection of figure 4.12 (b) shows a region of zero slope toward the higher wavenumbers, an exponential  $-4$  collapse that corresponds to the presence of a viscous diffusive layer at the start of the mix formed in the wake of the splitter plate (Corrsin 1951). At this early time, no equilibrium has been achieved between the production and dissipation terms as evidenced by the absence of an inertial range. From figure 4.12 (a),

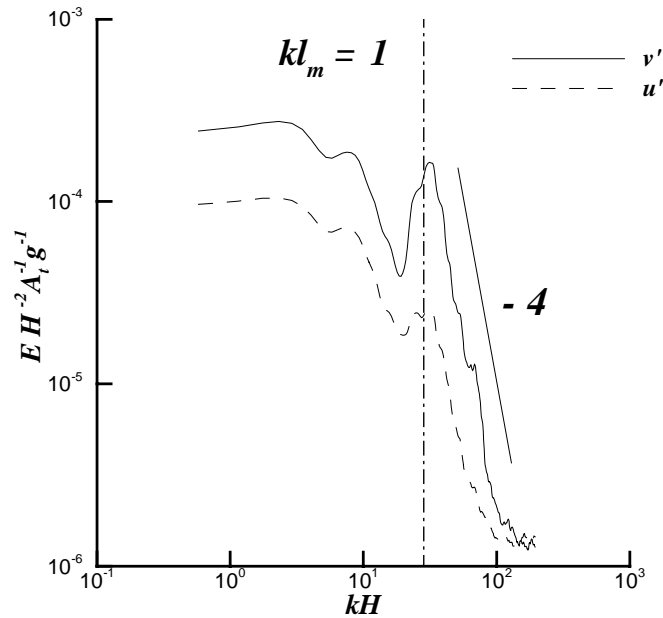


Figure 4.13. Frequency velocity spectra at  $T = 0.07$  at the centerline. The dashed line represents  $kH \sim 20$ .

it is evident that most of the energy is instead concentrated evenly in the low wavenumber region of the spectrum ( $kH < \sim 20$ ). The corresponding velocity spectra  $E_{u'}(k)$  and  $E_{v'}(k)$  at  $T \sim 0.07$  normalized by  $H^2 A_t g$  are shown in figure 4.13 and have a similar two-region structure: a flat region at the low-end of the wavenumber range followed immediately by a steep (slope  $\sim -4$ ) dissipative high-wavenumber region. Similar to the density spectra, there is a peak around  $kH \sim 20$  corresponding to a dominant wavepacket. Without this initial wavepacket, the  $k^{-4}$  fall-off would have started earlier, and the dip seen just before  $kH \sim 20$  is indicative of this collapse. Consistent with the profiles of  $\langle u'^2 \rangle$  and  $\langle v'^2 \rangle$  seen earlier, vertical fluctuations dominate, particularly at low wavenumbers, which make up most of the energy. It is believed from

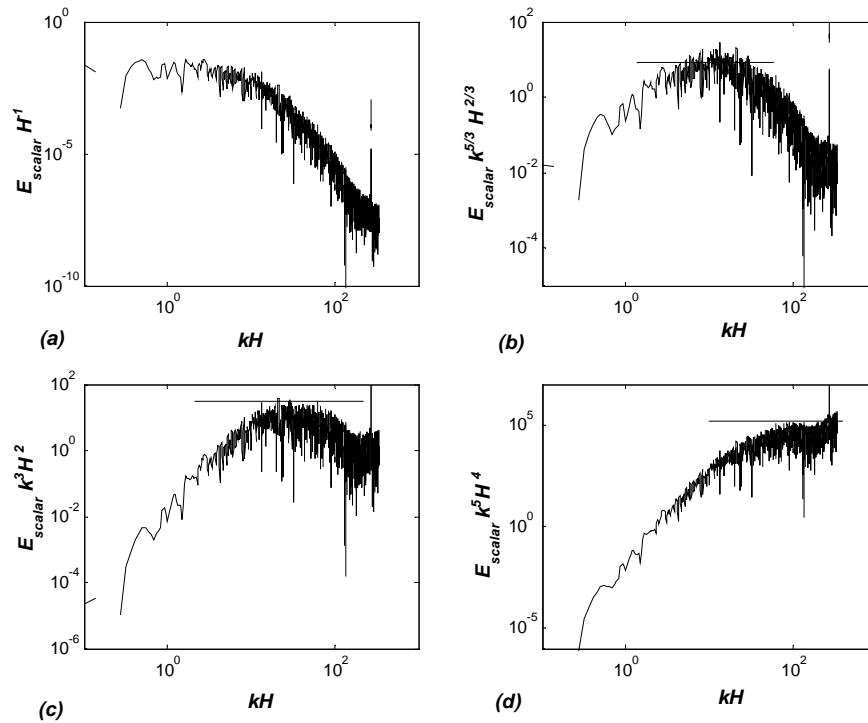


Figure 4.14. (a) Centerline density fluctuation spectrum  $E(k)$  at  $T = 1.008$  and compensated fluctuation spectra  $k^m E(k)$  where (b)  $m = 5/3$ , (c)  $m = 3$ , and (d)  $m = 5$ . Solid line represents the horizontal.

these measurements that for this experimental setup, the velocity spectrum, rather than the density spectrum, at the end of the splitter plate represents the true initial perturbation to the flow. This is because velocity perturbations are shed from the splitter plate, which lead to the formation of density perturbations in the wake. This is in contrast with Richtmeyer-Meshkov experiments where the initial perturbation is provided directly to the density interface. The velocity spectra obtained here may be used to initialize numerical simulations of Rayleigh-Taylor flows that are often initialized with density perturbations. We note the work of Dalziel *et al.* (1999), who used initial velocity spectra from their barrier experiments, and report good quantitative

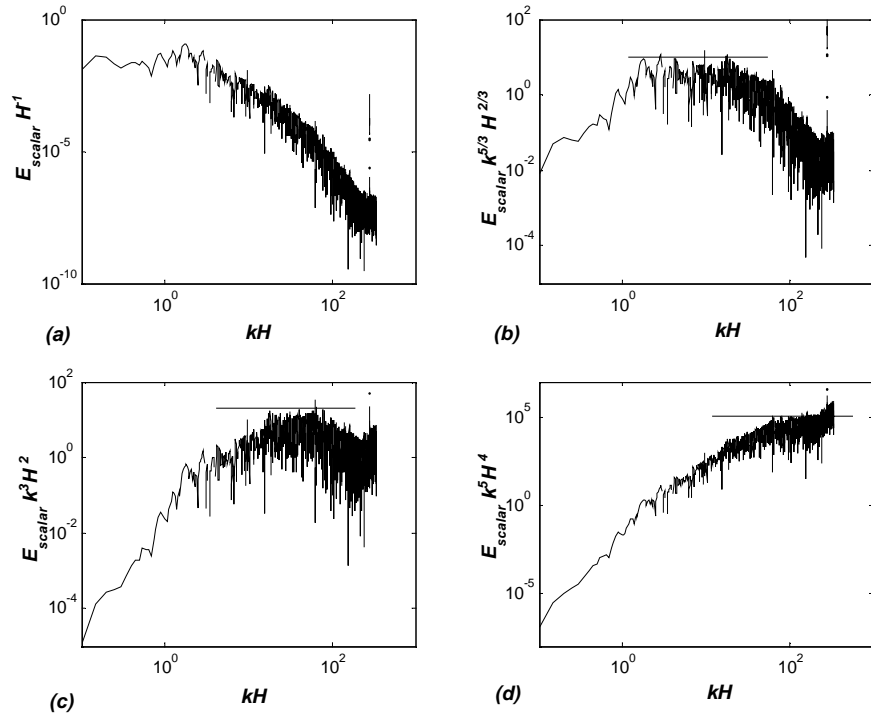


Figure 4.15. (a) Centerline density fluctuation spectrum  $E(k)$  at  $T = 2.08$  and compensated fluctuation spectra  $k^m E(k)$  where (b)  $m = 5/3$ , (c)  $m = 3$ , and (d)  $m = 5$ . Solid line represents the horizontal.

agreement in the large-scale measures such as the mix width. The perturbations in our experiment are primarily two-dimensional due to small-scale wake shedding off the end of the splitter plate, with short-wavelength modes (ripples) in the third direction. As mentioned previously, the dashed line indicating  $l_m = 1.05$  cm corresponds closely to a peak in the energy spectra, showing that the early-time dynamics shown here are dominated by a single wavelength that may also be conveniently represented in a numerical simulation.



Figures 4.14 (a) and 4.15 (a) show the density fluctuation spectra in the self-similar region at times  $T = 1.008$  and  $T = 2.086$ , respectively. The compensated energy spectra  $k^m E_{\rho'}(k)$  (normalized as  $k^m E_{\rho'}(k) H^{m-1}$ ) are also plotted in 4.14 and 4.15 (b)  $m = 5/3$ , (c)  $m = 3$ , and (d)  $m = 5$ . Figures 4.14 and 4.15 are snapshots of the density fluctuation spectra at early and late stages of the self-similar evolution. At each stage, there appears to be four distinct regions in the fully developed scalar spectrum (Wilson & Andrews 2002): 1) an energy containing range, 2) an inertial subrange with nearly a  $-5/3$  slope, 3) a viscous-diffusive subrange with a  $-3$  slope, and 4) a steeper diffusion dominated region with a  $-5$  slope. Figure 4.15 shows that with time, the viscous-diffusive layer is relegated primarily to the smaller scales where the energy cascade is due to stretching of fine-scale structures by the local velocity fields. Finally, at  $T = 2.08$ , the  $-5$  region occupies a very small portion of the spectrum. This process is accompanied by buoyancy-driven filling in (due to the development of the mushroom-shaped coherent structures) of the  $-5/3$  portions of the spectra. Since  $Re = 2h\dot{h}/\nu \propto t^3$  in this flow, the inertial range increases in width rapidly, spanning almost two decades of frequencies by  $T = 2.08$ .

In figure 4.16 (a), the velocity spectrum at  $T \sim 1.21$  also shows an inertial range with approximately a  $-5/3$  slope and a dissipative range with a  $-3$  slope. To elucidate the slopes in the velocity spectra, a moving window-averaging process was used that preserved the integral of  $E_{u'}(k)$  and  $E_{v'}(k)$  to within 1%. Figure 4.16 (b) presents the results of this smoothing process, with a window size of 20 points. Again, at the large

scales there is considerable anisotropy between the horizontal and vertical components. However, at higher wavenumbers, there is a convergence of energy associated with the horizontal and vertical velocities, indicating a tendency towards isotropy at these scales. Although we capture up to two decades in the wavenumber domain, we do not completely resolve the dissipative scales, as evidenced by the saturation (flattening) at large wavenumbers. From equation (2.3.1),  $Re_x \sim 1450$  at  $T \sim 1.21$ . The corresponding Kolmogorov time-scale is (Tennekes & Lumley 1972)

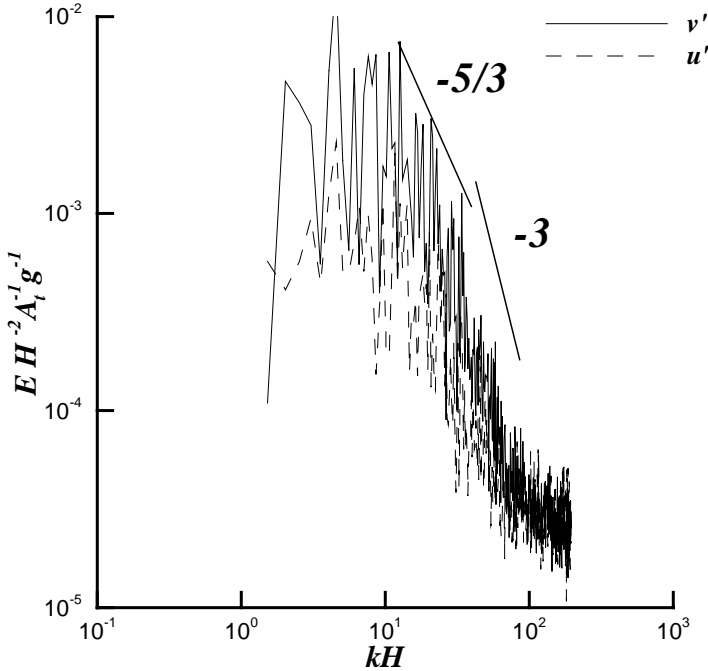
$$\tau_k = T Re_x^{-1/2} = 0.052 \text{ s} . \quad (4.3.2)$$

Here,  $\tau_k$  is the Kolmogorov time-scale and  $T$  is the integral time scale ( $= 2h_x/U$ ). Thus, at a sampling rate of 30 Hz ( $\Delta t = 0.03\text{s}$ ), the corresponding Nyquist limit ( $\sim 0.026 \text{ s}$ ) is not satisfied. Furthermore, there is also some spatial averaging due to the finite size of the PIV window, which could contribute to a smearing of the noise at higher frequencies.

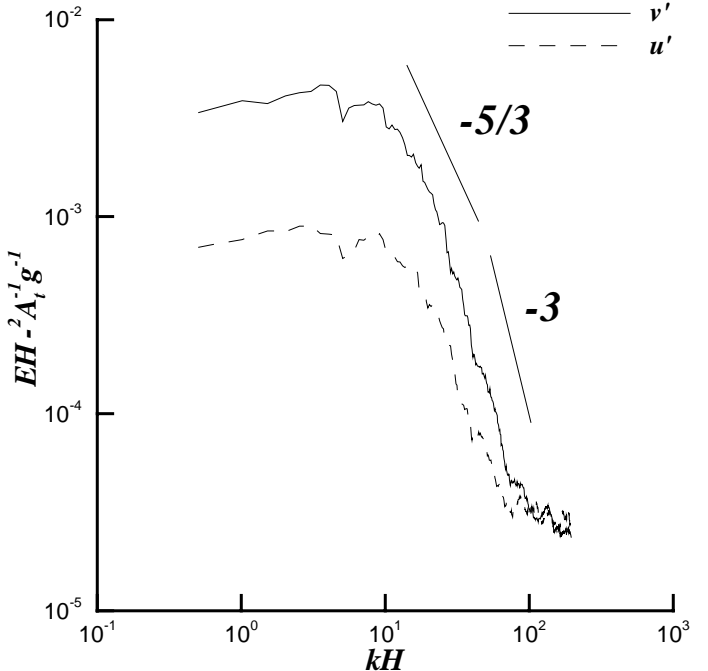
In the self-similar region of the flow ( $T > 1$ ), an equilibrium is achieved between the production and dissipation terms of the kinetic energy equation. This equilibrium manifests itself as the  $-5/3$  region in the spectrum. The universal inertial range spectrum is given by (Tennekes & Lumley 1972)

$$E(k) = A \varepsilon^{2/3} k^{-5/3} , \quad (4.3.3)$$

where  $\varepsilon$  is the kinetic energy dissipation rate and  $A$  is a universal constant. From the  $u'$  and  $v'$  velocity spectra, the net three-dimensional kinetic energy spectrum may be computed by assuming isotropy between  $u'$  and  $w'$  components of the velocity



(a)



(b)

Fig.4.16. Frequency velocity spectra at the centerline at  $T = 1.21$  (a) Raw spectra and (b) spectra smoothed using a window-averaging process.

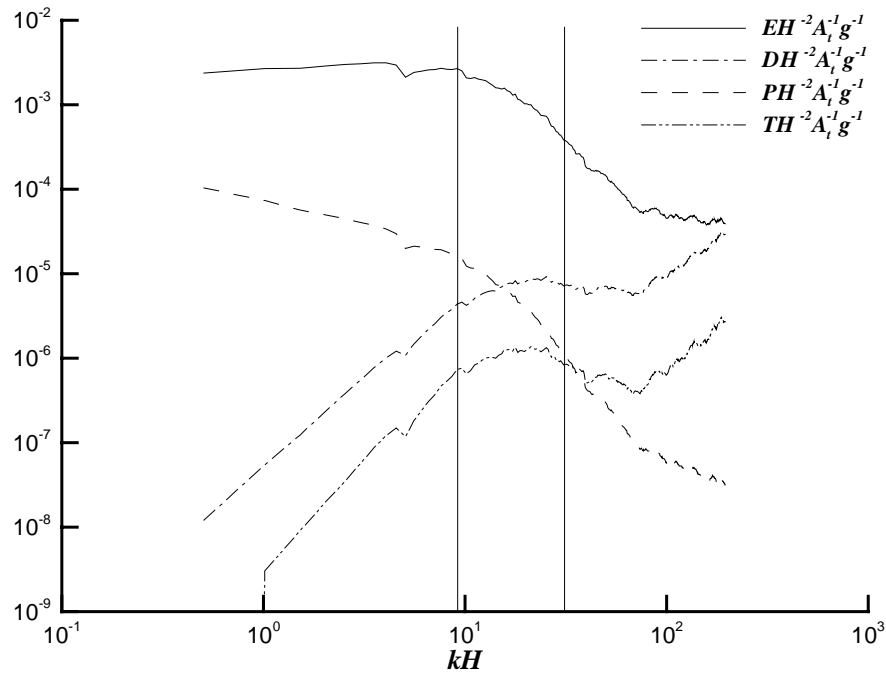


Figure 4.17. Spectra of total kinetic energy  $E(k)$ , Production  $P(k)$ , Dissipation  $D(k)$ , and Transfer  $T(k)$  at  $T = 1.21$  at the centerline.

fluctuations. In equation (4.3.3),  $A$  was determined through a curve fit of the experimental data to  $E(k)$  to be  $\sim 5$  ( $A \sim 1.5$  for most turbulent flows, Tennekes & Lumley (1972)). In the above,  $\varepsilon$  was determined from the integral of  $D(k)$  the dissipation spectrum given by

$$D(k) = 2\nu k^2 E(k), \quad (4.3.4)$$

where  $\nu$  is the viscosity and  $\varepsilon = \int D(k) dk$ . Correspondingly, the production spectrum

$P(k)$  can be written as

$$P(k) = \frac{2\pi B}{A^{1/2}} \frac{S^2}{\varepsilon^{1/3}} k^{-2/3} E(k), \quad (4.3.5)$$

where  $S$  is the dominant strain rate in the flow ( $S = u/l$ , where  $u$  and  $l$  are the velocity and length scales given by  $u = v'$  and  $l = \frac{u^3}{\varepsilon}$ , respectively, and  $B$  is another universal constant). By fitting the experimentally measured  $P(k)$  to the above equation,  $B$  was determined to be 0.6 ( $B \sim 0.3$  for a typical turbulent flow, Tennekes & Lumley (1972)). The difference between the measured values of  $A$  and  $B$  from those obtained from other flows is believed to be due to the moderate values of  $Re$  employed in the current work.

Thus,  $P(k)$  represents the production of kinetic energy primarily due to straining of eddies by successively larger eddies. Figure 4.17 is a plot of the above defined spectra for  $T = 1.21$ . Production is dominant at low wavenumbers, and dissipation is dominant at high wavenumbers. The intermediate region (enclosed by the solid lines), where  $P(k)$  and  $D(k)$  intersect, is thus the inertial subrange. In this subrange, the energy transfer spectrum  $T(k) = \frac{2\pi}{A^{3/2}} kE(k)s(k)$  has a zero slope indicating constant energy flux.

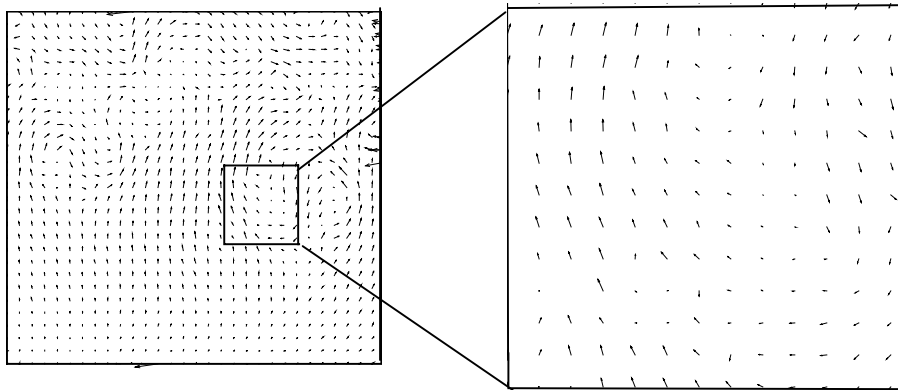
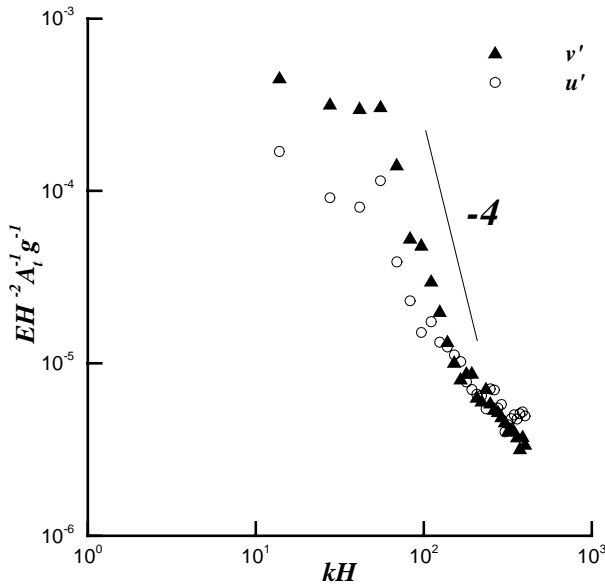


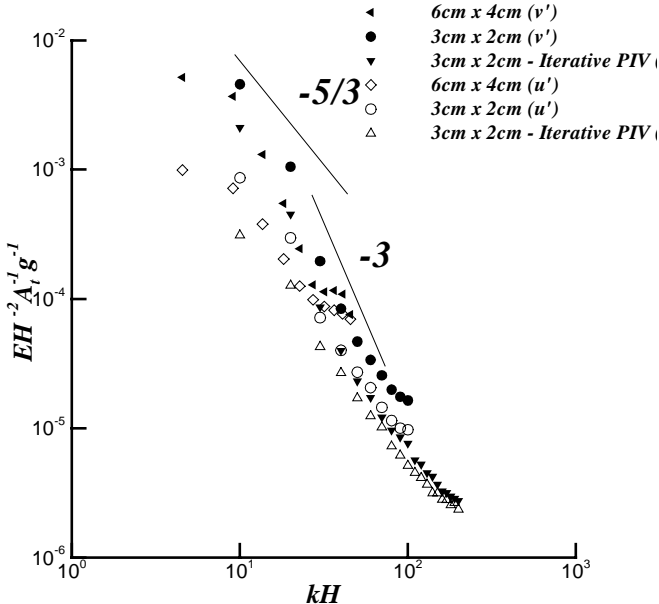
Figure 4.18 Velocity field from fig. 3.5 (c) processed through iterative-PIV technique

Wavenumber power spectra were also obtained by taking velocity data points along a vertical slice of the 2D velocity field. The higher wavenumbers were captured by repeating the experiment, with the PIV camera placed much closer to the channel. This reduced the physical size of the window from 6 cm x 4 cm to 3 cm x 2 cm, thus doubling the spatial resolution. A further increase in resolution was obtained by using an iterative PIV technique (Scarano & Riethmuller 1999), an approach similar to that used in multi-grid numerical simulations. In the first iteration, the displacement vector is computed to integer accuracy. The interrogation window size is then halved and the integer displacement is used to search for a correlation peak, thus giving a velocity vector that is of sub-grid accuracy. Figure 4.18 shows the vector field of figure 3.5 (c), but processed using the iterative approach, giving twice the resolution. Thus, with both refinements we are able to achieve a four-fold improvement in resolution, and we can capture turbulence length-scales as small as 0.06 cm.

Figures 4.19 (a) and (b) are plots of the wavenumber spectra at  $T = 0.07$  and 1.21, obtained from the above process. The structural properties are similar to the spectra obtained from timeseries data: anisotropy at the large scales and a tendency towards isotropy at the smaller scales. At  $T = 0.07$ , the wavenumber spectrum shows a flat top and a steep dissipative range at high wavenumbers. The spatial resolution at this Reynolds number is sufficient to capture the Kolmogorov scales. Also, at  $T \sim 1.21$  there is a distinct inertial range with the  $-5/3$  slope. For the  $u'$  and the  $v'$  velocities, the spectra were constructed by overlaying the individual spectra from each wavenumber range. The tailing off seen at the end of each of these spectra is due to noise saturation at that resolution. Thus, by coming in closer and applying the iterative PIV technique, both the resolution and the accuracy of the measured wavenumber spectra have been improved.



(a)



(b)

Figure 4.19. Wavenumber velocity spectra at the centerline at (a)  $T = 0.07$  and (b)  $T = 1.21$ .



From the results it is evident that buoyancy forcing at small Atwood numbers does not affect the formation of a  $-5/3$  inertial range, in accordance with the classical Obukhov-Corrsin theory for turbulent scalar fluctuations (Obukhov 1949; Corrsin 1951). The scaling argument proposed by Zhou (2001) for the velocity spectra of a Rayleigh-Taylor flow is extended here to scalars. Zhou argues that the kinetic energy dissipation is a function of the timescale of decay of triple velocity correlations,  $\tau(k)$ ,

$$\varepsilon \sim \tau(k) k^4 E^2(k), \quad (4.3.6)$$

where  $E(k)$  is the kinetic energy spectrum,  $k$  is the wavenumber, and the exponents in the above equation are obtained from dimensional analysis. In the absence of external forcing on the energy containing eddies (e.g., homogenous, isotropic turbulence),  $\tau$  may be chosen as the timescale of nonlinear interactions among the energetic modes.

$$\tau(k) = [k^3 E(k)]^{-1/2}. \quad (4.3.7)$$

Substituting for (4.3.7) in (4.3.6), the classical Kolmogorov form of the energy spectrum is recovered:

$$E(k) \sim \varepsilon^{2/3} k^{-5/3}. \quad (4.3.8)$$

In the presence of external buoyancy forcing, the governing timescale is supplied by gravity. Thus,  $\tau_{RT} = (k A_t g)^{-1/2}$ , giving (Zhou 2001)

$$E_{RT}(k) \sim (g A_t)^{1/4} \varepsilon^{1/2} k^{-7/4}. \quad (4.3.9)$$

The constant of proportionality in the above equation was determined to be  $\sim 3$  from our experimental velocity data. An extension of the above argument may be proposed for

buoyancy forcing of the scalar fluctuation spectrum. The dissipation of scalar variance is given by (Tennekes & Lumley 1972)

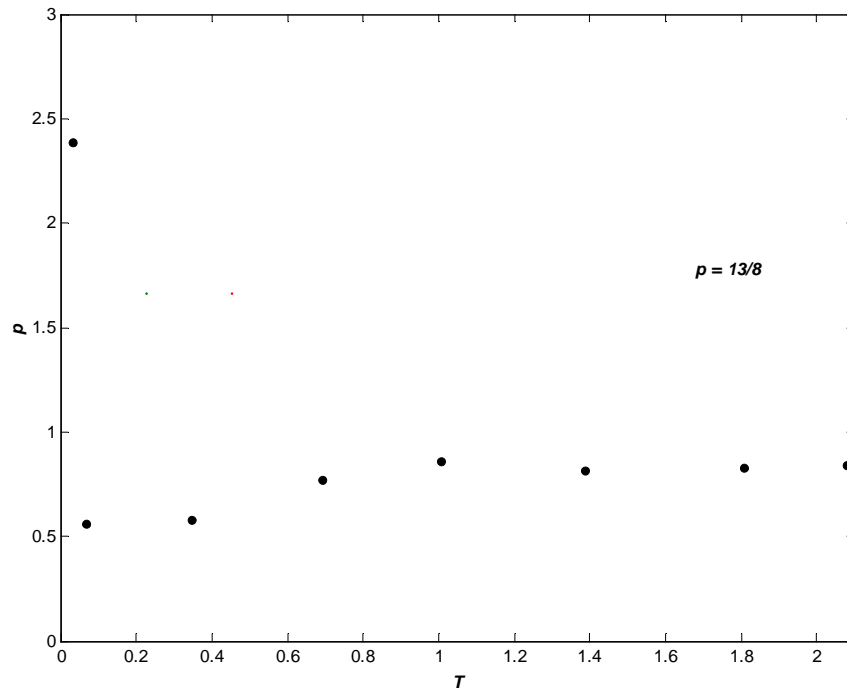


Figure 4.20. Time evolution of exponential curve-fit index,  $p$  for centerline temperature measurements.

$$N \sim k^2 E^{scalar} (kE_{RT})^{1/2}. \quad (4.3.10)$$

Substituting for  $E_{RT}(k)$  from equation (4.3.9), we get

$$E_{RT}^{scalar} \sim N(A_1 g)^{-1/8} \epsilon^{1/4} k^{-13/8}, \quad (4.3.11)$$

giving a power law close to the  $-5/3$  observed in the present experiments. For  $T \sim 1.008$ , the constant in equation (4.3.11) was determined from our data to be  $\sim 1$ . Thus, it

appears that the buoyancy forcing does not significantly alter the power law of the inertial range.

The spectral structure of temperature (density) fluctuations at each time can be quantified through an exponential curve fit,  $E(k) \sim e^{-p}$ . The best fit to the data is obtained by performing a Nelder-Mead simplex direct search (Nelder & Mead 1965) in  $p$ -space by minimizing the function  $E(k) - e^{-p}$ . For  $Re \rightarrow \infty$ ,  $p$  should  $\rightarrow 13/8$  for density fluctuations in R-T flows. Figure 4.20 is a time history of  $p$  and shows that this asymptotic value is never reached due to the finite values of  $Re$  in this experiment. At early times,  $p \sim 2.5$  is highest due to the presence of the viscous-diffusive layer with an exponential drop-off. However, the onset of self-similarity ( $T \sim 1.008$ ) is clearly marked by the attainment of a constant value by  $p$  ( $\sim 0.85$ ). This implies that the structure of the scalar spectra is preserved in the self-similar regime even as it contains regions where the slope is not  $-13/8$ . These are primarily the energy-containing scales and the diffusive scales. At high enough  $Re$ , it is expected that these scales will occupy a much smaller percentage of the spectral width giving a value for  $p$  approaching  $13/8$ .

#### *4.4 Taylor Microscales*

More significant than the Kolmogorov scales are the Taylor microscales associated with the local strain rate, and can be directly obtained from the turbulent velocity fluctuations. The Taylor length scales,  $\lambda_u$  and  $\lambda_v$ , associated with the horizontal and vertical velocity fluctuations are given by

$$\lambda_u(t) = \left[ -\frac{1}{2} f''(0,t) \right]^{-1/2} \quad \lambda_v(t) = \left[ -\frac{1}{2} g''(0,t) \right]^{-1/2}, \quad (4.4.1)$$

where  $f(r,t)$  and  $g(r,t)$  are the non-dimensional autocorrelation functions given by

$$f(r,t) = \langle u(x+r,t)u(x,t) \rangle / \langle u^2 \rangle$$

$$g(r,t) = \langle v(x+r,t)v(x,t) \rangle / \langle v^2 \rangle.$$

Thus, the Taylor microscale is the  $r$ -intercept of the osculating parabola  $f(r)$  at  $r = 0$  (Pope 2000).

From the velocity data, a point at the center of the mix was picked, and its autocorrelation function in space was computed. This process was repeated for other datapoints in the vicinity, and the mean Taylor length scale was determined. A histogram of the Taylor scales also showed a peak around the mean value. Like much of the velocity statistics described in Section 4.2, it was found that the Taylor scales do not vary significantly across the mix. Thus, we present only the centerline values in the following.

The results are presented in table 4.2, along with the Kolmogorov scale for comparison. The Taylor scales in space show a tendency toward anisotropy with a  $\lambda_y/\lambda_x$  ratio approaching a value of 2. Cook & Zhou (2002) in their DNS simulations report a ratio of

Taylor length scale, $\lambda_x$	0.29 cm
Taylor length scale, $\lambda_y$	0.62 cm
Vertical Velocity scale, $v'$	0.82 cm/s
Horizontal Velocity scale, $u'$	0.45 cm/s
Taylor Reynolds number, $Re_{\lambda_y}$	60
Kolmogorov length scale, $\eta$	0.027 cm

Table 4.2. Taylor scales at  $T = 1.21$ .

1.4 at  $T > 2.5$  (for  $\rho_2/\rho_1 \sim 3$ ). Furthermore, the Taylor microscales are approximately 10-20 times the size of the Kolmogorov scales. Taking the velocity scale associated with the Taylor length scales to be the r.m.s. of vertical velocity fluctuations, a Taylor scale Reynolds number may be computed for the present experiment as

$$Re_{\lambda} = \frac{\lambda v'}{\nu} = 60. \quad (4.4.2)$$

This value is less than the threshold for mixing transition for turbulent flows ( $Re_\lambda \sim 100$ ) and is expected to cross this value further downstream. However, we observe self-similarity has been achieved in these experiments as is evidenced by the p.d.f.s, spectra,

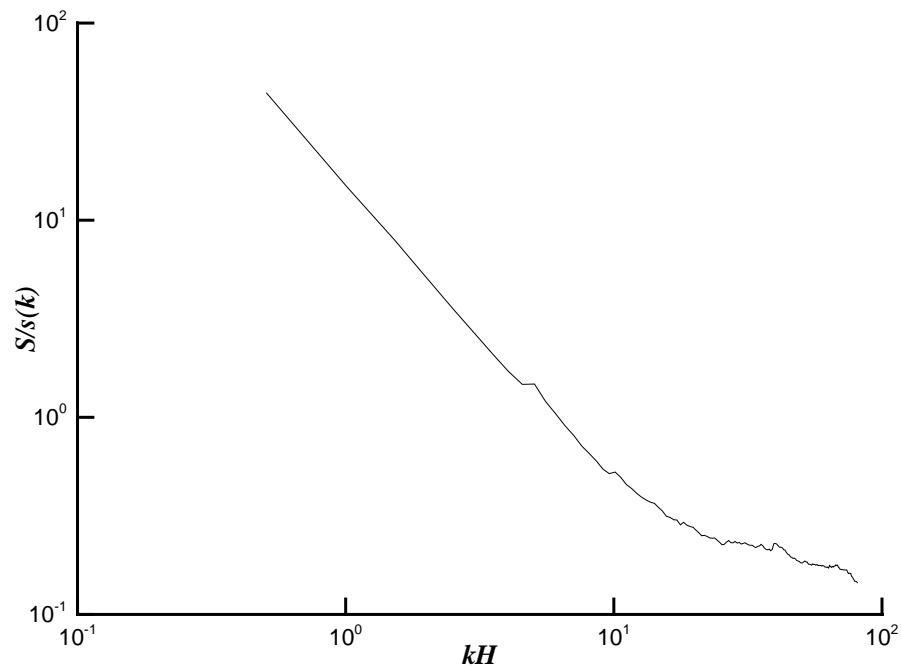


Figure 4.21. Spectra of  $S/s(k)$  showing tendency toward isotropy at higher wavenumbers for the centerline velocity spectra.

and velocity profiles (for  $T > 1$ ), even though our Taylor Reynolds number of 60 is less than the value of 100 suggested (Dimotakis 2000) for mixing transition. Thus, even at low Atwood numbers, there is surely a differential straining of eddies in the direction of gravity, resulting in anisotropy of velocity fluctuations at all but the smallest scales.

This tendency toward anisotropy may be quantified by the local (in wavenumber space) strain rate. For any eddy of size  $2\pi/k$ , with a characteristic velocity scale defined as  $[kE(k)]^{1/2}$ , the characteristic strain rate can be defined as (Tennekes & Lumley 1972)

$$s(k) = \frac{(kE(k))^{1/2}}{2\pi/k} = \frac{(k^3E(k))^{1/2}}{2\pi}. \quad (4.4.3)$$

Thus the local strain rate increases with decreasing eddy size, so that the smallest eddies undergo the severest straining. Following Tennekes & Lumley (1972), taking the time scale  $1/s(k)$  to represent the time required to return to isotropy once the strain field is removed, the eddies with large  $k$  are quickest in their realignment. So the non-dimensional parameter  $S/s(k)$ , where  $S$  is the mean strain rate, characterizes the degree of isotropy (large  $S/s(k) \rightarrow$  anisotropy).  $S/s(k)$  is plotted for the velocity spectrum at  $T \sim 1.21$  in figure 4.21 and shows anisotropy at all but the smallest scales. This is consistent with the picture depicted by the velocity spectra and Taylor microscales.

#### 4.5 Energy Budget

Following Youngs (1994), from our simultaneous measurements of velocity and density fields, the net kinetic energy dissipation from the initial state of the flow is computed. The initial potential energy  $PE_i$ , associated with the flow, is calculated assuming a stepfunction at  $z = H/2$  for the density profile at  $T = 0$ . Thus,

$$PE_i = \int_0^H \rho_{step} gy dy = \int_0^{H/2} \rho_1 gy dy + \int_{H/2}^H \rho_2 gy dy. \quad (4.5.1)$$

Also, at  $T = 0$ ,  $KE_i \sim 0$ , since there is negligible energy associated with velocity fluctuations. Further downstream, the potential energy at  $T = 1.21$  is computed from the measured density profile as

$$PE_f = \int_0^H \rho_{measured} g y dy \quad \cong \quad \sum_{i=0}^n \rho_i g y_i \Delta y. \quad (4.5.2)$$

The potential energy released to the flow by  $T = 1.21$  is then given by  $PE_{released} = PE_f - PE_i$ . Some of this energy is converted into kinetic energy, which can be directly obtained from our measured velocity profiles of  $u'$  and  $v'$ . As previously mentioned, observations of the axisymmetric mushroom structures mean we may take the turbulence as homogeneous with respect to the streamwise direction  $x$  and the spanwise direction  $z$ , and set  $\langle u'^2 \rangle = \langle w'^2 \rangle$ . Then,

$$KE_{generated} = \frac{1}{2} \int_0^H \rho (2\langle u'^2 \rangle + \langle v'^2 \rangle) dy, \quad (4.5.3)$$

and the net kinetic energy dissipation is given by

$$D = PE_{released} - KE_{generated}. \quad (4.5.4)$$

The net  $KE$  dissipation as a fraction of the potential energy released,  $D/PE_{released}$  was determined from our measurements to be 0.49 at  $T \sim 1.21$ . Note that the net kinetic energy dissipation may also be determined from  $\varepsilon = \int D(k) dk$  where  $D(k)$  is given by equation (4.3.4). Youngs (1994) reported a value of 0.52 obtained from 3D numerical simulations, and significantly lesser values from 2D simulations ( $D/PE_{released} \sim 0.06$ ) since dissipation is primarily a 3D mechanism. For a self-similar mix, characterized by the length scale  $gt^2$ , it is expected that  $D/PE_{released}$  and  $KE_{generated}/PE_{released}$  become



constant in the self-similar regime. Thus, we find good agreement between the present experiments and related, but higher Atwood number, 3D simulations.

The mixing efficiency  $\psi$ , a bulk mixing parameter, can also be computed from the density data, and represents the fraction of the initial potential energy,  $PE_i$ , that is used up in mixing the fluid (Linden & Redondo 1991), and is given by

$$\Psi = (PE_{released} - \frac{1}{4}P_0)/(\frac{1}{2}P_0), \quad (4.5.5)$$

where  $P_0 = 4/3 PE_i$  is the initially available potential energy and  $PE$  is the potential energy released by late time. From the current data,  $\psi$  was determined to be  $\sim 0.78$ , which is higher than the value reported by Linden & Redondo's salt experiments ( $\psi \sim 0.35$ ) at low Atwood numbers (For completely mixed fluids,  $PE = 1/2P_0$ , and  $\psi = 0.5$ ). We believe that Linden & Redondo report lower values from measuring  $\psi$  at late time, when there is almost no kinetic energy left in the flow (the maximum value of 0.5 can be reached only in this limit). In our experiment at  $T \sim 1.21$ , there is still a significant amount of kinetic energy ( $\sim 50\%$  of the potential energy released). By assuming a linear profile for the density (supported by our experimental measurements in figure 3.1), we show here analytically that values of  $\sim 0.8$  can be expected. From Linden & Redondo, the initially available potential energy in the flow may be written as

$$P_0 = \frac{1}{2}gH^2\Delta\rho, \quad (4.5.6)$$

where  $\Delta\rho = \rho_1 - \rho_2$ , and  $H$  is the mix-width. The energy released by late time is

$$PE_{released} = g \int_0^H z (\rho(y) - \rho_2) dy. \quad (4.5.7)$$

We substitute a linear profile for  $\rho(y) = \rho_2 + \Delta\rho \frac{y}{H}$  in (4.5.7) giving

$$PE_{released} = \frac{g\Delta\rho H^2}{3}. \quad (4.5.8)$$

Using (4.5.6) and (4.5.8) in (4.5.5), the mixing efficiency  $\psi$  is  $\sim 0.83$ . Thus, this definition is seemingly not appropriate for such dynamic conditions as the self-similar regime of the R-T flow. Perhaps a more appropriate mixing measure is the pointwise molecular mixing fraction  $\theta(y)$ , or the global molecular mix parameter

$$\Theta = \frac{1}{H} \int_0^H \theta(y) dy \quad (4.5.9)$$

that we report in this work.

## 5. NUMERICAL TECHNIQUE

### 5.1 Preliminaries

A 3D, single-phase version of the finite-volume code *RTI-3D*, developed by Andrews (1995) was used to solve the Euler equations. The code is third-order accurate in space and second-order accurate in time. The single-phase governing equations are

$$\text{Continuity: } \frac{\partial(f_i \rho_i)}{\partial t} + \frac{\partial(f_i \rho_i u)}{\partial x} + \frac{\partial(f_i \rho_i v)}{\partial y} + \frac{\partial(f_i \rho_i w)}{\partial z} = 0 \quad (5.1.1)$$

$$\text{x-momentum: } \frac{\partial(f_i \rho_i u)}{\partial t} + \frac{\partial(f_i \rho_i u^2)}{\partial x} + \frac{\partial(f_i \rho_i uv)}{\partial y} + \frac{\partial(f_i \rho_i uw)}{\partial z} = -f_i \frac{\partial p}{\partial x} + f_i B_{i,x} \quad (5.1.2)$$

$$\text{y-momentum: } \frac{\partial(f_i \rho_i v)}{\partial t} + \frac{\partial(f_i \rho_i uv)}{\partial x} + \frac{\partial(f_i \rho_i v^2)}{\partial y} + \frac{\partial(f_i \rho_i vw)}{\partial z} = -f_i \frac{\partial p}{\partial y} + f_i B_{i,y} \quad (5.1.3)$$

$$\text{z-momentum: } \frac{\partial(f_i \rho_i w)}{\partial t} + \frac{\partial(f_i \rho_i uw)}{\partial x} + \frac{\partial(f_i \rho_i vw)}{\partial y} + \frac{\partial(f_i \rho_i w^2)}{\partial z} = -f_i \frac{\partial p}{\partial z} + f_i B_{i,z} \quad (5.1.4)$$

where the  $f_i$ s are the volume fractions of the  $i^{\text{th}}$  fluid ( $f_1 + f_2 = 1$ ),  $u$ ,  $v$ , and  $w$  are the velocities in the  $x$ -,  $y$ - and  $z$ - directions, and  $B_{i,(x,y,z)}$  is a body force term. A staggered cell arrangement is used for the pressure and velocities, with the pressure node located at the cell center, while the velocities are computed on the cell faces. Explicit time stepping was used in the solution of these equations, with the size of the time step chosen to satisfy a Courant condition (in practice, the time step was chosen to be a tenth of the Courant limit). A three-stage, fractional step algorithm is used to advance the solution in time: At each step, an advection calculation followed by a Lagrangian source term update is performed. In the Lagrangian calculation,

$$u_E^* = u_E^{n+1/2} + \frac{\Delta t}{\rho_i \Delta x} (p_P^n - p_E^n) + g_x \quad (5.1.5)$$

$$v_N^* = v_N^{n+1/2} + \frac{\Delta t}{\rho \Delta y} (p_P^n - p_N^n) + g_y \quad (5.1.6)$$

$$w_T^* = w_T^{n+1/2} + \frac{\Delta t}{\rho \Delta z} (p_P^n - p_T^n) + g_z \quad (5.1.7)$$

where  $E, N$ , and  $T$  are the East, North, and Top cell faces, and  $g_x = g_z = 0$ . The superscript  $n+1/2$  denotes an intermediate value obtained after an advection update, and the asterisk represents the results of the Lagrangian update. To satisfy continuity, the net volume flux across each cell is set to zero:

$$\delta V_E - \delta V_W + \delta V_N - \delta V_S + \delta V_T - \delta V_B = 0 \quad (5.1.8)$$

where say,  $\delta V_E = \Delta t \Delta y \Delta z (u_E^{n+1} \rho_E^{n+1})$ . Here,  $n+1$  indicates the updated velocities that satisfy continuity, after a correction has been added i.e.  $u_E^{n+1} = u_E^* + \Delta u_E$  for velocities and  $p_P^{n+1} = p_P^* + \Delta p_E$  for pressure. Substituting the updated velocities in to equations (5.1.5), (5.1.6), and (5.1.7) and subtracting these equations evaluated with the velocities at  $*$ , we get for the velocity correction in the East face,

$$\Delta u_E = \frac{\Delta t}{\rho_i \Delta x} (\Delta p_P - \Delta p_E), \quad (5.1.9)$$

with similar expressions for the other components. Using these expressions in (5.1.8) results in a Poisson equation for the pressure correction  $\Delta p$ .

$$-a_P \Delta p + a_E \Delta p_E + a_W \Delta p_W + a_N \Delta p_N + a_S \Delta p_S + a_T \Delta p_T + a_B \Delta p_B = -D \quad (5.1.10)$$

where, for instance,

$$a_E = -\frac{\Delta t \Delta y \Delta z}{\Delta x} \left( \frac{f_{1,E}^{n+1}}{\rho_1} + \frac{f_{2,E}^{n+1}}{\rho_2} \right) \quad (5.1.11)$$

An iterative conjugate gradient algorithm is used to solve the Poisson equation. The iterative procedure is repeated until  $|D|$  summed over all the cells is less than a specified threshold (typically  $\sim 10^{-4}$  for the simulations reported here).

The Van Leer method (Van Leer 1977) was used to calculate convective fluxes. The method minimizes numerical diffusion, and prevents spurious overshoots and undershoots that occur due to the use of higher order numerical schemes. A two-phase, 2D version of this code was tested and validated for both R-T and Kelvin-Helmholtz flows in Andrews (1995). The 3D, single-phase version was used in Dimonte *et al.* (2003), and compared well with other benchmark codes commonly used in the study of R-T. These results are summarized in Appendix C.

Figure 5.1 shows a 2D slice of the 3D computational domain. For the simulations discussed in sections 6.3, 6.4 and 6.5, the dimensions of the box were chosen to be 1cm x 1cm x 2cm in the  $x$ -,  $z$ -, and  $y$ - directions respectively (where  $y$ - is the direction of the gravity vector). The interface between the heavy ( $\rho_1$ ) and light ( $\rho_2$ ) fluids is at  $y = 0$ . The densities were chosen to be  $\rho_1 = 3$ , and  $\rho_2 = 1$  g/cc ( $A_r=0.5$ ). These densities were chosen to match the values used by other benchmark codes in the comparative study reported in Appendix C. The box is 0.9375 cm in the positive  $y$ - direction and 1.0625 cm in negative  $y$ - direction to account for the slightly different growth rates of bubbles and

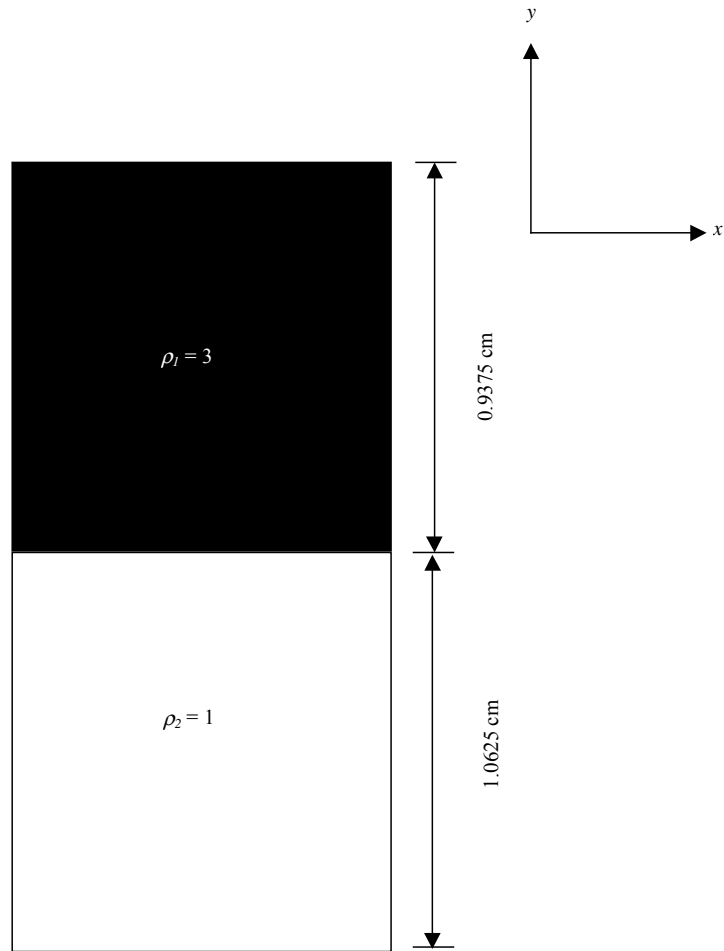


Figure 5.1 2D slice of computational domain used in numerical simulations:  $\rho_1 = 1$  g/cc, and  $\rho_2 = 3$  g/cc.

spikes at this Atwood number. For the simulations that used experimental initial conditions (sections 7.2 and 7.3), the box size was chosen to be 15cm x 15cm x 30cm and the Atwood number was 0.00075, except where stated otherwise. For the low Atwood number cases, the interface was exactly at the center of the box.

Perturbations are imposed on the interface ( $y=0$ ) as fluctuations of the density surface.

These are then converted to volume fraction using,  $f_1(x, z) = 1 + \frac{h_0(x, z)}{\Delta}$  for  $y < 0$ , and

$f_1(x, z) = \frac{h_0(x, z)}{\Delta}$  for  $y > 0$ , where  $\Delta$  is the grid spacing in cm. The pressure is initialized

to the hydrostatic pressure in this incompressible problem using,  $p(y) = gy(\rho_1 - \rho)$ ,

where  $\rho = f_1\rho_1 + f_2\rho_2$ . Periodic boundary conditions were used in the  $x$ - and  $z$ -

directions, while zero-flux conditions were used in the  $y$ -direction. All the multi-mode

simulations reported here used a resolution of  $128 \times 128 \times 256$  grid points in the  $x$ -,  $z$ -, and

$y$ - directions respectively. The single-mode calculations discussed in the next two

sections had lower resolutions (discussed below). The calculations were stopped when

the bubble height reached  $\sim 0.8$  cm i.e. 80% of the computational domain height. The

bubble and spike amplitudes were written out at each timestep, while 3D datafiles

containing the volume fractions and velocities were written for  $A_i g t^2 = 1, 2, 3 \dots$

### *5.2 Estimation of Numerical Viscosity: Single-mode Calculations*

While RTI-3D solves the Euler equations with no specified viscosity, numerical

diffusion serves to smear out small scales in much the same way physical viscosity

would. Such numerical techniques, referred to as MILES (Monotone-Integrated Large

Eddy Simulation), have been demonstrated to be particularly attractive for flows with

shocks (Richtmeyer-Meshkov) and discontinuities (R-T) by Youngs (2003). The

effective numerical viscosity of the MILES technique used here was determined through

comparison of single-mode simulations with linear theory results (Chandrasekhar 1961).

The technique used is described in detail in Dimonte *et al.*(2003), and some essential aspects are reviewed herein. These single-mode calculations were initialized with perturbations in the  $x$ - and  $z$ - directions with a wavelength  $\lambda = 1$  cm, and amplitude  $a_0 = 0.001$  cm.

$$h_0(x, z) = a_0(\cos(kx) + \cos(kz)), \quad (5.2.1)$$

where  $k = 2\pi/\lambda$  and had an Atwood number of 0.5. The density interface at the centerline was converted to volume-fraction as described in section 5.1. The calculations were performed at resolutions of  $\lambda/\Delta = 4, 8, 16$ , and 32.

Figure 5.2 (a) shows the time evolution of bubble amplitudes defined using the 50% volume fraction thresholds at different resolutions. The initial exponential growth of these disturbances, appears linear in the log-scales of 5.2 (a). The highest resolution case (32 zones/ $\lambda$ ) grows the fastest, while the case with 4 zones/ $\lambda$  has the slowest growth rate. In the presence of viscosity, the exponential growth of small-amplitude R-T modes is modified according to the following dispersion relation (Chandrasekhar 1961):

$$\Gamma^2 = Akg - 4\nu k^2 \Gamma + 4k^4 \nu^2 \left( \sqrt{1 + \Gamma/k^2 \nu} - 1 \right) \quad (5.2.2)$$

The viscosity  $\nu$ , in the above equation is determined by using the observed growth rate  $\Gamma$  from the numerical simulations (Dimonte *et al.* 2003). Here,  $\Gamma$  is obtained by fitting the observed amplitudes to linear theory ( $h_k(t) = h_{0k} \cosh(\Gamma t)$ ). For all the cases, around  $t = 7$ s, the transition to nonlinearity takes place with the bubble velocity reaching its

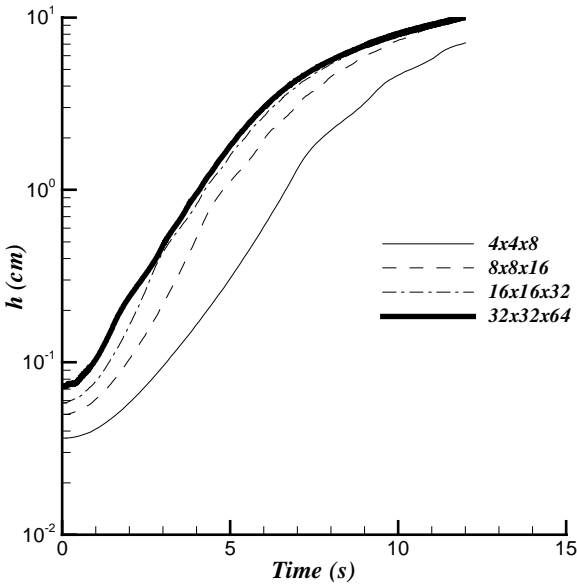


terminal value ( $v_\infty = c_\infty \sqrt{A_t g l_m / 2}$ ). We describe the procedure to determine  $c_\infty$  in the next section.

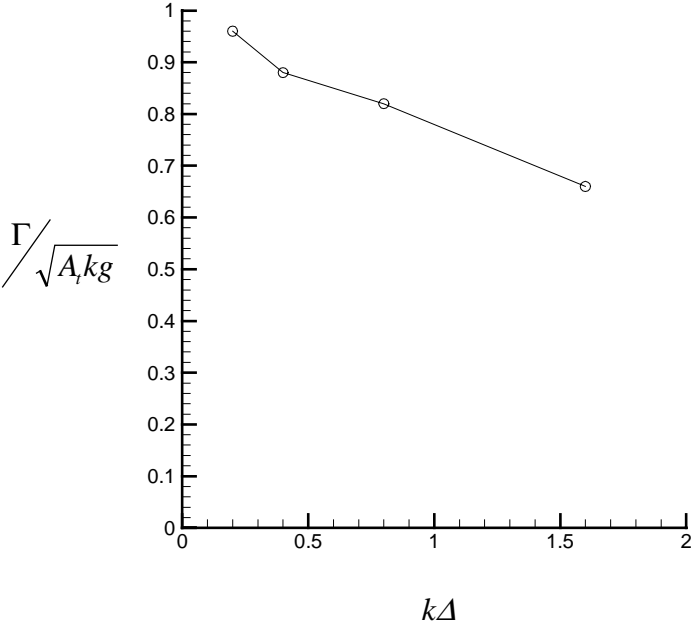
Figure 5.2 (b) shows the variation of the scaled growth rate  $\Gamma / \sqrt{Akg}$  with  $k\Delta$ , the non-dimensional zoning parameter. For  $k\Delta = 0.196$  (32 zones/ $\lambda$ ), the growth rate approaches the inviscid value ( $\Gamma / \sqrt{Akg} \sim 1$ ). At a resolution of 4 zones/ $\lambda$ ,  $\Gamma$  is only  $\sim 65\%$  of the inviscid value. From the above, we can conclude that to resolve an R-T mode (with  $\sim 20\%$  error) at least 8 nodes are required. As we will see in section 6.2, the implication of a numerical viscosity for multi-mode simulations is that it sets an upper bound for the fastest growing modes.

### 5.3 Determination of $c_\infty$ : Single-mode Calculations

We now describe the procedure used to determine the constant  $c_\infty$  required for defining the terminal velocity for a single bubble in section 4.2. To match the experiments, these simulations had a box size of 15cm x 15cm x 60cm, and an Atwood number of 0.001. This would produce R-T bubbles similar to that observed in the experiment. The perturbations were initialized as before (section 5.2), with an amplitude  $a_0$  of 0.1cm (now,  $\lambda = 15$ cm). The contour map of the initial perturbations is shown in figure 5.3. The evolution of the 50% isosurfaces of volume-fraction  $f_I$  are shown in figure 5.4 (a),



(a)



(b)

Figure 5.2. (a) Bubble amplitude evolution from the single-mode calculations at different resolutions. (b) The non-dimensional exponential growth-rate as a function of the resolution.

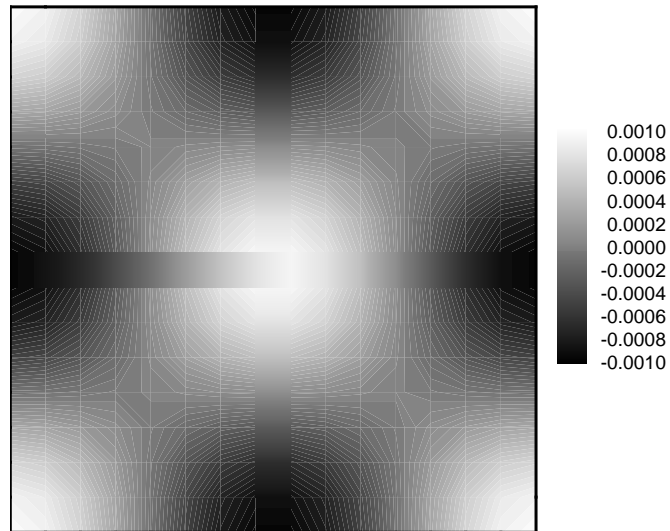


Figure 5.3. Contour map of volume fraction  $f_I(x,z)$  at  $t = 0$  for the single-mode calculations.

(b), and (c) for  $A_t g t^2 = 0.1, 0.4,$  and  $0.7$  m respectively. Since the initial perturbation had a peak at the center of the computational box (white region in figure 5.3), a bubble forms at the center in figure 5.4, with spikes at the four corners, while spikes form at the cell faces. The amplitudes of the spike and bubble penetration are approximately the same in

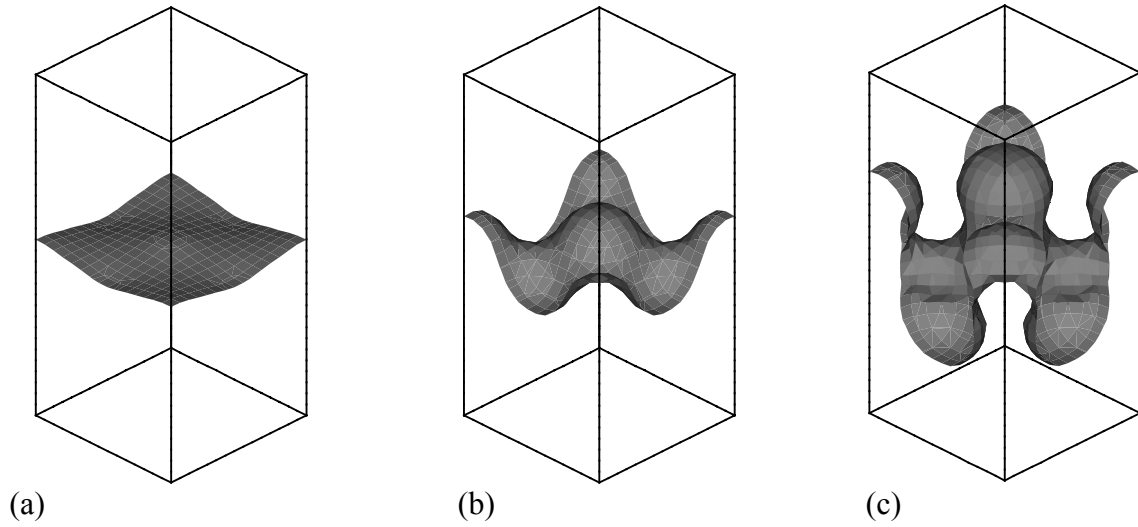


Figure 5.4. (a), (b) and (c) showing the evolution of single-mode perturbations at  $A_1 g t^2 = 0.1$ , 0.4, and 0.7 m respectively. Shown are the iso-surfaces of  $f_I = 0.5$ .

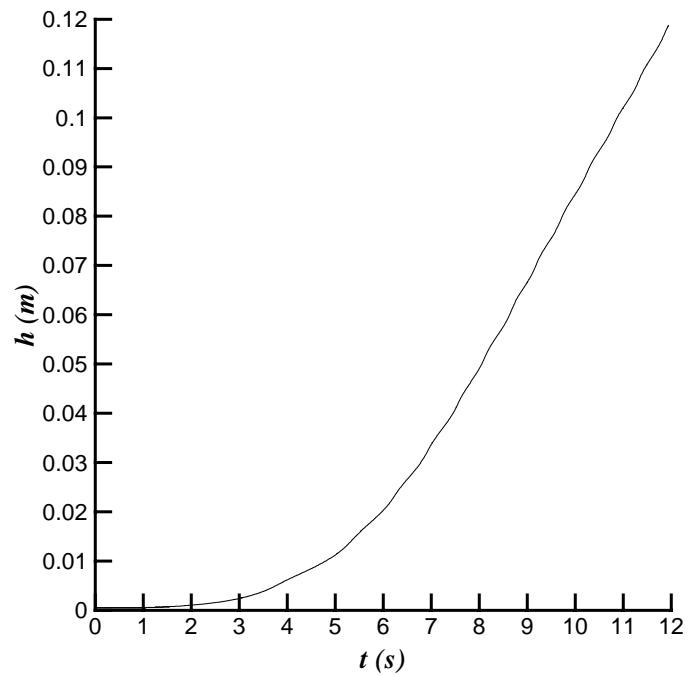


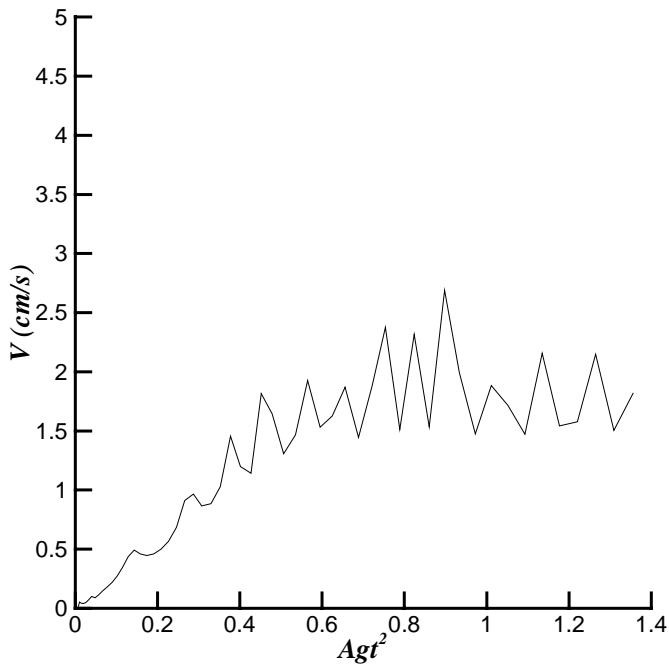
Figure 5.5. Evolution of bubble amplitude  $h$  (m) plotted as a function of time (s).

this low-Atwood number simulation. The evolution of the bubble amplitude (defined based on the 50% of the volume fraction) is shown in figure 5.5 and shows a region of exponential growth followed by linear growth in time (saturation to constant velocity). Note that in the presence of other wavelengths, bubbles compete and larger bubbles would accelerate past the smaller structures. Thus, the larger the bubble the greater its velocity, modifying the linear growth rate seen here to the quadratic evolution described in (1.2.1).

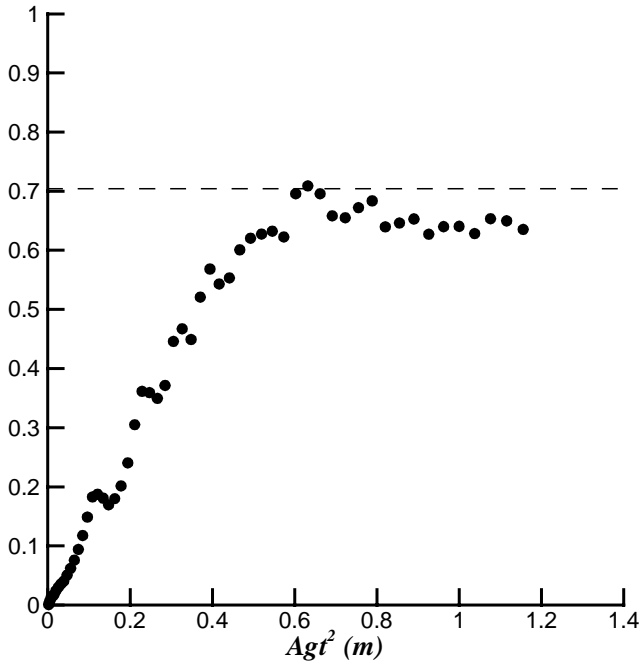
The speed of penetration of the bubble is obtained by differentiating the bubble amplitude with respect to time,  $v_\infty = dh_b/dt$ , and is plotted in figure 5.6 (a). The non-dimensional constant  $c_\infty$  is then determined as

$$c_\infty = \frac{v_\infty}{\sqrt{A_t g \lambda / 2}}. \quad (5.3.1)$$

Figure 5.6 (b) is a plot of  $c_\infty$ , which approaches the previously reported value of 0.7 (Daly 1967) at low Atwood numbers. At higher  $A_t$ , Daly's values are lower ranging from 0.49 for a density ratio  $\rho_1/\rho_2$  of 1.5 to 0.32 for  $\rho_1/\rho_2 = 10$ . According to Daly, the discrepancy at higher Atwood numbers may have been due to lack of sufficient time window for averaging.



(a)



(b)

Figure 5.6. Evolution of the terminal velocity  $v_\infty$  (a) and the dimensionless constant  $c_\infty$  (b) for a 3D R-T bubble at  $A_r=0.001$ .

## 6. EFFECT OF INITIAL CONDITIONS ON R-T GROWTH

### 6.1 Introduction

In section 6.3, a model for the dependence of R-T growth on the initial conditions is verified through numerical simulations. The model developed by Dimonte (2003) and described in Appendix D, relates the self-similar constants  $\alpha$  and  $\beta$  to the initial perturbation amplitude. Other effects such as mode-coupling, and spectral slopes were also investigated. In section 4.2, the self-similarity of R-T flows was demonstrated through the velocity r.m.s. profiles, p.d.f.s of density, and spectra of velocity and density. Here, we address the issue of universality of the R-T growth constant  $\alpha$ .

It is well known (Chandrasekhar 1961) that for R-T in the linear regime ( $h_k \ll 1/k$ ) in the absence of stabilizing mechanisms such as viscosity or surface tension, the bubble height remains a function of the initial amplitudes:

$$h_k(t) = h_{0k} \cosh(\Gamma t), \quad (6.1.1)$$

where the exponential growth rate  $\Gamma = \sqrt{A_t g k}$ , and  $k$  is the wavenumber of a mode.

When the flow transitions to nonlinearity ( $h_k \sim 1/k$ ), successively longer wavelengths come to the fore and grow as (Ratafia 1973)

$$v_\infty = c_\infty \sqrt{A_t g \lambda_b / 2}, \quad (6.1.2)$$

where  $c_\infty$  is a Froude-like number, and was determined to have a value of  $\sim 0.7$  from single-mode studies (section 5.3; Daly 1967), and  $\lambda_b$  is the bubble wavelength. For R-T, the Froude number  $Fr_0$  is defined as

$$Fr_0 = v_b \sqrt{\frac{\rho_1}{\rho_1 - \rho_2} \frac{2}{gD_b}}. \quad (6.1.3)$$

A more detailed discussion on the definition and significance of Froude number on the self-similar evolution of R-T is deferred until section 6.2. In the nonlinear regime, R-T grows according to equation (1.2.1). In this picture, the flow has no memory of the initial conditions and the only relevant length scale is  $A_t g t^2$ . Two parameters characterize self-similarity:  $\alpha_b = \frac{dh_b}{d(A_t g t^2)} = \text{constant}$ ,  $\beta_b = \frac{\lambda_b}{h_b} = \text{constant}$ . However, as described in section 1.2, a universal value for the growth constant  $\alpha_b$  has eluded both experimental and numerical investigations. In sections 6.3, 6.4, and 6.5, we are primarily concerned with the dependence of the bubbles (rising columns of light fluid) on the initial conditions, since R-T flows are driven by the growth of the bubbles. The bubbles in turn displace the heavier fluid that form spikes.

Birkhoff (1955) argued that for self-similarity to be established, the initial spectra should have amplitudes distributed as  $k^{-1}$ . Birkhoff's model predicts a dependence of  $\alpha_b$  on three parameters viz. the initial r.m.s. amplitude  $h_{0k}$ , the Froude number  $Fr_0$ , and the threshold for the nonlinear transition ( $\sigma \sim h_k k$ ). Cherfilis and Mikaelian (1996) generalized



Birkhoff's model to any initial amplitude, and nonlinear threshold  $\sigma$ , giving for  $\alpha_b$  (and setting  $A_t \sim 1$ )

$$\alpha_b = \frac{Fr_0}{4 \left[ (2\pi)^{-1/2} \ln(\sigma/h_{0k}) - \sigma/Fr_0 \right]} \quad (6.1.4)$$

Birkhoff assumed  $Fr_0 = 1/\sqrt{6\pi} = 0.23$  from Layzer (1955), the standard value for  $\sigma = 1/2\pi$ , and  $h_{0k} = 0.001$  giving  $\alpha_b = 0.07$ ; The value of  $Fr_0$  used here is much lower than that suggested by experimental measurements (Read 1984) and drag-buoyancy models (Davies & Taylor 1950; Scorer 1957; Collins 1957; Alon *et al.* 1995). Using  $Fr_0 \sim 1$  from these studies, (6.1.4) gives  $\alpha_b \sim 0.14$  which is higher than experimentally observed values even at high  $A_t$  (Dimonte & Schneider 2000). Note that Birkhoff only considered a 1-D initial spectrum, resulting in a two-dimensional flow.

Haan considered the constructive interference experienced by adjacent modes in a wavepacket, triggering transition when the sum of modal amplitudes in the wavepacket is  $\sim \sigma/k$ . Thus individual modes in a wavepacket may become nonlinear even when their amplitudes are below the threshold due to their interaction with adjacent modes of similar phase. In this formulation, a  $k^{-2}$  initial spectrum is required to produce self-similarity (as defined above). Dimonte (2003) developed these ideas further by considering the role of the Froude number and  $\beta_b$ , and applying a Fermi transition (see Appendix D) to a wavepacket (rather a single mode). The resulting model equations, repeated below, will be verified here using carefully designed numerical simulations.

$$\alpha_b = \frac{Fr_0 \sqrt{\pi}}{4} \left[ \cosh^{-1} \left( \frac{Fr_0 \sqrt{\pi/2}}{k \langle h_{0k} \rangle} \right) - 1 \right]^{-1} \quad (6.1.5)$$

$$\beta_b = \frac{2\sqrt{\pi}}{Fr_0} \left[ \cosh^{-1} \left( \frac{Fr_0 \sqrt{\pi/2}}{k \langle h_{0k} \rangle} \right) - 1 \right]^{-1} \quad (6.1.6)$$

( $\langle \bullet \rangle$ ) is defined as the average over a wavepacket of width  $\delta k$  defined in Appendix D).

Using the same value for  $Fr_0$  as above, and setting  $k \langle h_{0k} \rangle = 0.001$  in the above equation, we get  $\alpha_b \sim 0.06$  which is closer to the experimentally observed value of 0.07. Similar to Birkhoff's model, which was extended to Richtmeyer-Meshkov and Kelvin-Helmholtz flows (Cherfills & Mikaelian 1996), the above formulation may also be generalized to these other flows. Dimonte's model is described in detail in the Appendix D to this work.

The above analysis assumes the presence of long-wavelength perturbations in the initial spectral content whose initial amplitudes govern their late-time self-similar growth rate. In the opposite limit, where such low-wavenumber modes have negligible energy compared with the high-wavenumber content, long-wavelengths are generated purely by the nonlinear coupling of modes. The resulting evolution of bubble heights is then independent of initial amplitudes, and  $\alpha_b$  takes up a lower bound value of  $\sim 0.03 \pm 0.003$  (Dimonte *et al.* 2003). Note that while most numerical simulations are initialized with such annular spectra, most experiments have long-wavelength content in their initial conditions. This could explain the discrepancy between the experimental and numerical

values of  $\alpha_b$ . Here, we examine both these limits through 3D, numerical simulations. Other possible influences on the growth rate such as the spectral shapes (referred to as the Spectral Index ( $p$ ) herein, and quantified as the exponent of the wavenumber i.e.  $h_{0k} = k^{-p}$ ), are also explored here.

### 6.2 Multi-mode Calculations

The multimode calculations were designed to test the dependence of the growth constant  $\alpha_b$  on the initial amplitudes, Spectral Index, and mode-coupling. The two-dimensional perturbations are initialized as,

$$h_0(x, z) = \sum_{k_x, k_y} a_k \cos(k_x x) \cos(k_z z) + b_k \cos(k_x x) \sin(k_z z) + c_k \sin(k_x x) \cos(k_z z) + d_k \sin(k_x x) \sin(k_z z) \quad (6.2.1)$$

where  $k = \sqrt{k_x^2 + k_z^2}$ .

Simulation	Spectral Index ( $p$ )	$N_{\min}$	$N_{\max}$	$k\langle h_{0k} \rangle$
1	-2	3	32	0.004
2	-2	3	32	$4.0 e^{-05}$
3	-2	3	32	0.04
4	-2	1	32	0.0011
5	-2	1	32	0.011
6	-2	2	32	0.0044
7	-2	2	32	0.0003
8	-2	2	32	$3.0 e^{-06}$
9	0	2	32	$0.004^*$
10	-1	2	32	$0.0045^*$
11	-	16	32	$0.0016^*$
12	-	16	32	$1.6 e^{-05}^*$

Table 6.1: List of simulations.

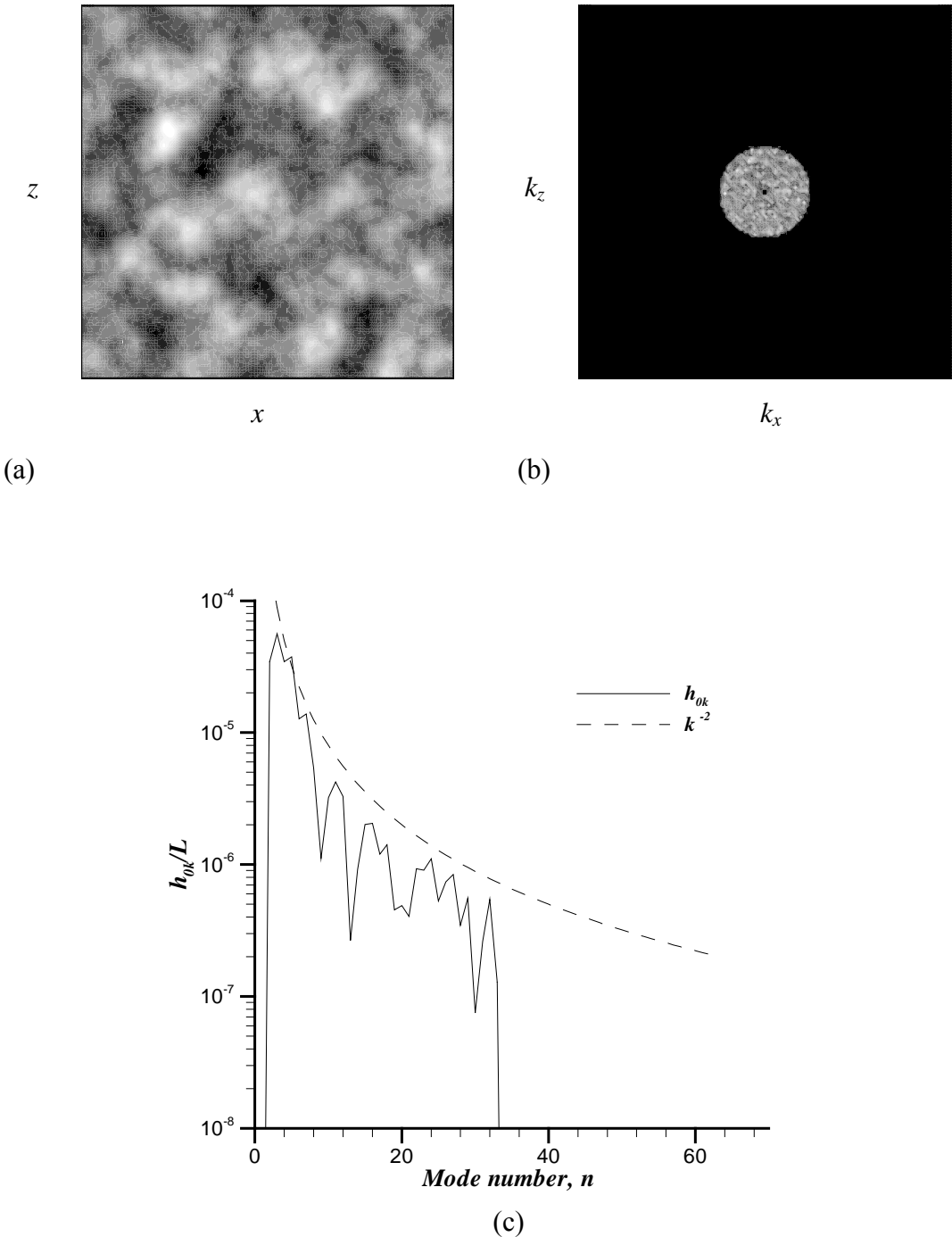


Figure 6.1 Initial perturbations for simulation 6 in (a) physical and (b) wavenumber space. (c) Initial perturbations as a function of the mode number,  $n$ . Dotted line elucidates the  $k^{-2}$  structure.

In the above, the amplitudes  $a_k$  etc. have random phases. Table 6.1 is a list of all the calculations. Simulations 1 – 8 were initialized with a non-dimensional r.m.s. amplitude  $k\langle h_{0k} \rangle$  ranging from  $3 \times 10^{-6}$  (case 8) to 0.04 (case 3). Here,  $k$  is chosen from linear stability analysis as the most dominant mode in the initial wavepacket. The r.m.s. amplitude of a wavepacket  $\delta k$  is defined as (Haan 1989; Dimonte 2003):

$$\langle h_k \rangle = \left[ \frac{L^2}{2\pi} \int_{k-\delta k}^{k+\delta k} h_k^2 k' dk' \right]^{1/2}. \quad (6.2.2)$$

Note that for a  $k^{-2}$  spectral structure,  $k\langle h_{0k} \rangle$  is a constant value independent of  $k$ . All of these cases had the modal amplitudes  $a_k$ ,  $b_k$ ,  $c_k$ , and  $d_k$  varying as  $k^{-2}$  to test equations (6.1.5) and (6.1.6). These calculations had energy in modes 1-32 (cases 4, and 5), 2-32 (cases 1, 2, and 3), and 3-32 (cases 6, 7, and 8). Here, a mode represents one wave of a perturbation, and the mode number  $n = L/\lambda$ . Figures 6.1 (a) and (b) are the perturbation amplitudes for a typical case (# 6) in physical and wavenumber space respectively. Figure 6.1 (c) is the corresponding azimuthally averaged Fourier amplitudes elucidating the  $k^{-2}$  (dashed line) structure of the spectra. Cases 6, 9, and 10 all have the same amplitude ( $k\langle h_{0k} \rangle \sim 0.0044$ ) and  $N_{min}$  (=2), but spectral indices (quantified by the exponential curve-fit index,  $p$ ) of  $-2$ ,  $0$ , and  $-1$  respectively. Together, they constitute a study on the effect of  $p$  on  $\alpha_b$  and  $\beta_b$ .

To test the opposite limit of mode-coupling, the perturbation energy was confined to an annulus ( $16 < n < 32$ ) in wavenumber space (figures 6.2 (a) and (b)) for cases 11 and 12.

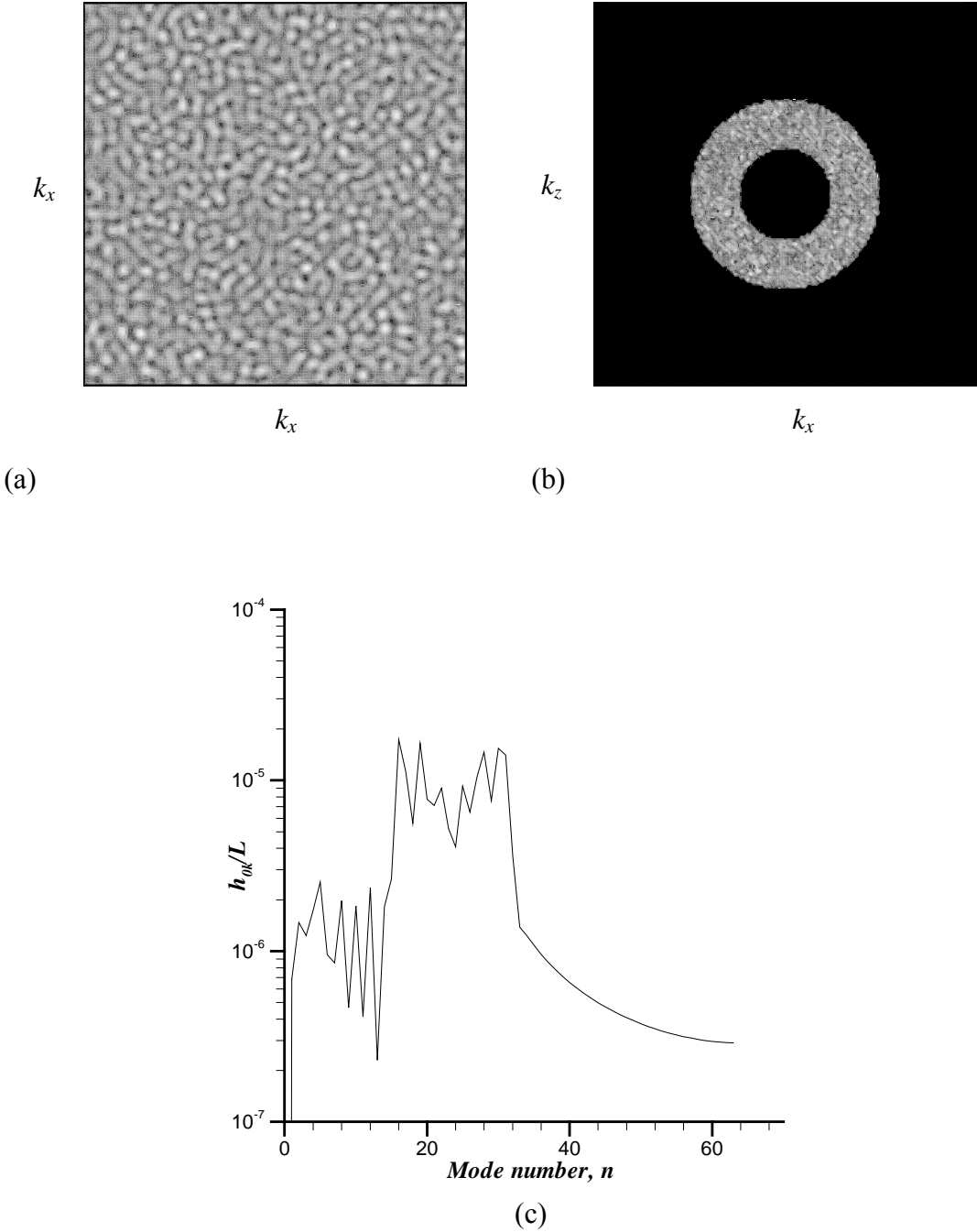


Figure 6.2. Initial perturbations for simulation 11 in (a) physical and (b) wavenumber space. (c) Initial perturbations as a function of the mode number,  $n$  showing energy between  $n = 16$  and  $32$ .

The azimuthally averaged Fourier amplitudes for case 11 are shown in figure 6.2 (c). Most numerical simulations of R-T (Young *et al.* 2001; Cook and Dimotakis 2001; Youngs 1991; Youngs 1994; Youngs 2003) are initialized with such an annular distribution of energy. It is expected that the mode-coupling cases will produce a much lower growth rate than the simulations initialized with the longer modes. It must also be noted that most experiments have long-wavelength content in their initial conditions (Ramaprabhu & Andrews 2003<sup>b</sup>; Dimonte & Schneider 2000), which could explain the higher values of  $\alpha_b$  conventionally reported from such studies.

We now address the issue of the peak wavenumber in the presence of numerical viscosity in these simulations. Numerical viscosity (like other stabilizing mechanisms) places an upper bound on the fastest growing wavenumbers. Setting  $\partial\Gamma/\partial k = 0$  in equation (5.2.2), the peak wavenumber  $k_p$  is determined as (Daly 1967; Chandrasekhar 1961):

$$k_p \approx 0.5 \left( \frac{A_t g}{\nu^2} \right)^{1/3}. \quad (6.2.3)$$

The fastest growing mode number for the current simulations was determined to be  $N_p \sim 24$  (Dimonte *et al.* 2003), and within the range of modes (1-32) imposed in the initial conditions here. This guarantees that the linear growth stage is reproduced accurately by these calculations.



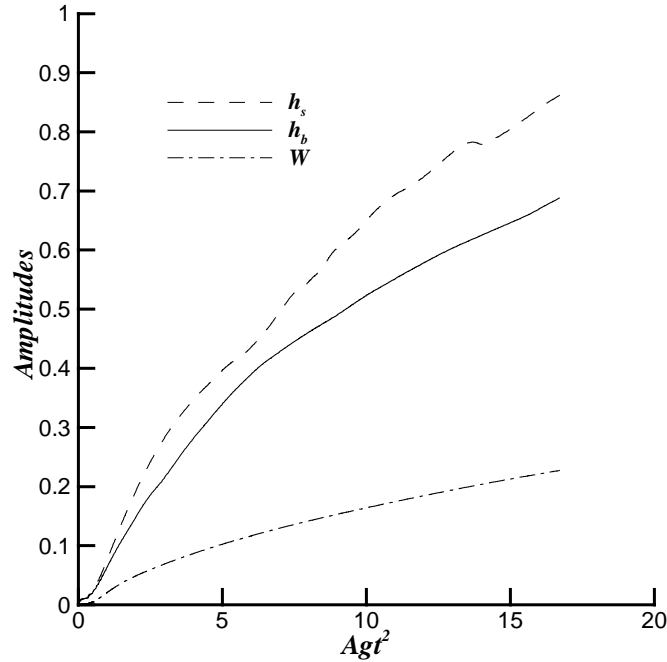


Figure 6.3. Evolution of bubble and spike amplitudes ( $h_b$  and  $h_s$ ), and integral width  $W$  for case 6.

Figure 6.3 shows the evolution of the bubble and spike amplitudes ( $h_b$  and  $h_s$ ) as a function of the self-similar length scale  $A_i g t^2$  (cm) for case 6. The bubble and spike amplitudes are defined as the  $y$ -location where the average value (over the  $x$ - $z$  plane) of  $f_l$  reaches 1% and 99% respectively. Nonlinearity sets in when the most dominant wavelength  $\lambda_p = 2\pi/k_p$  saturates. This transition time may be determined by equating the linear and nonlinear velocities for  $k_p$  using the Fermi transition (Appendix D), giving

$$t_k = (A_i k_p g)^{-1/2} \cosh^{-1} \left( \frac{Fr_0 \sqrt{\pi/2}}{k \langle h_{0k} \rangle} \right). \quad (6.2.4)$$

For the parameters used here, the transition occurs at  $A_1 g t_k^2 \sim 0.604$  for this case. Table 6.2 is a list of the transition times from all the simulations. We take this time to represent the onset of self-similarity, and the statistics for each case were determined after the nonlinear transition had set in. One of the concerns in computing  $\alpha_b$  and  $\beta_b$  was that it had to be done in a time window after the nonlinear transition, but before the emergence through mode-coupling of longer wavelengths not originally imposed. The time  $t_{mc}$  at which wavelengths due to mode-coupling appear is determined as follows. From the width of the wavepacket (Appendix D)  $\delta k = \pm \frac{3}{8} k_p$ , where  $k_p$  is the dominant mode at any given time, we may determine the lowest mode in the computational domain to be

$$k_{\min} = k_p - \frac{3}{8} k_p. \quad (6.2.5)$$

When  $k_{\min}$  equals the lowest mode imposed in the initial conditions, mode-coupling is said to have set in. For example, for simulation 1, this would occur when  $n_{\min}$  reached 3.

Thus, the cutoff time is chosen as the value of  $t$ , when  $k_p = \frac{8}{5} k_{\min}$ . The dominant mode

$k_p$  at any time is determined by an autocorrelation procedure described below. The values of  $\alpha_b$  and  $\beta_b$ , and other quantities are then obtained by averaging for  $t_k \leq t \leq t_{mc}$ .

Table 6.3 is a list of the mode-coupling transition times from the calculation.

The ratio  $h_s/h_b \sim 1.25$  observed here at late time is consistent with experimental observations for  $A \sim 0.5$  (Dimonte & Schneider 2000). We also plot the integral mix width defined as (Andrews & Spalding 1990)

Simulation	Nonlinear transition time, $A_t g t_k^2$
1	0.584
2	1.81
3	0.224
4	0.872
5	0.414
6	0.604
7	1.25
8	2.89
9	0.628
10	1.15
11	0.232
12	1.14

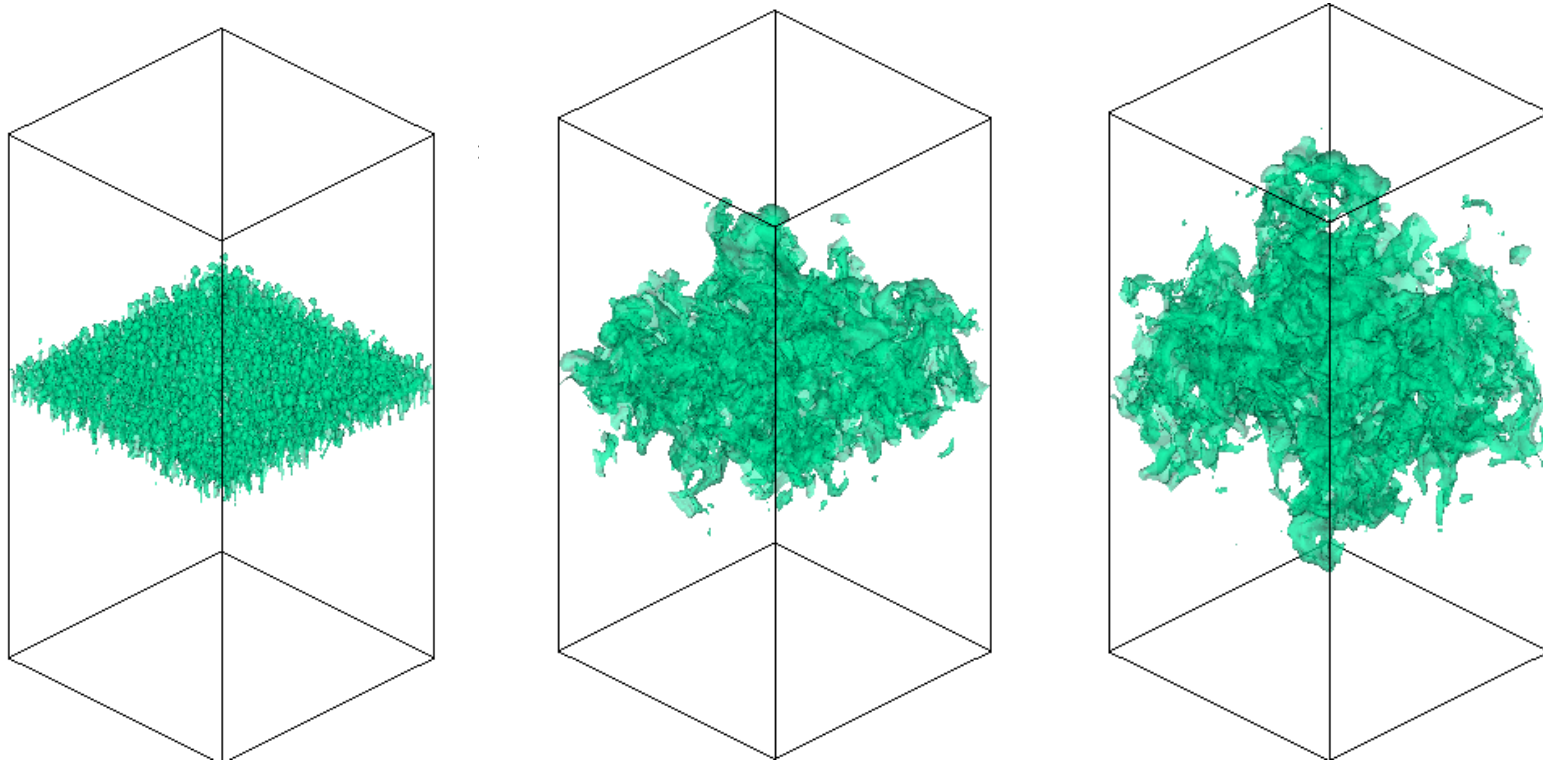
Table 6.2. The nonlinear transition time  $A_t g t_k^2$  for the 12 simulations.

Simulation	Mode-coupling onset time, $A_t g t_{mc}^2$
1	8
2	18
3	6
4	14
5	7.7
6	15
7	20
8	33
9	16
10	18
11	-
12	-

Table 6.3. Times at which mode-coupling begins for the 12 simulations.

$$W = \int \langle f_1 \rangle \langle f_2 \rangle dz. \quad (6.2.6)$$

For small Atwood numbers  $h_b \sim h_s$ , and assuming a linear profile for the volume fractions,  $h \sim 3W$  consistent with figure 6.3 ( $h \sim 3.2W$  if the effects of numerical diffusion are considered). It is not clear, why a second weak transition in the  $h_b$  and  $h_s$  time traces is observed around  $A_i g t^2 \sim 5$ . Originally, we thought this might be due to the emergence of products of mode-coupling around that time. However, from our analysis of the bubble-front images (discussed below), it was determined that mode-coupling does not occur in these simulations until after the transition observed here. Another reason for this behavior may be the lack of a sufficient number of bubbles/spikes required for averaging.  $h_s$  and  $h_b$  were also computed from the  $x$ -intercept of a linear fit to the volume fraction profiles. Since the results of this method (which is less affected by statistical fluctuations) agreed with the plots in figure 6.3, the 1% and 99% threshold has been used throughout this paper.



(a)

(b)

(c)

Figure 6.4 Iso-surfaces of 1% of volume-fraction  $f_l$  from simulation 11 at  $A_t g t^2 = 1$  (a), 10 (b), and 19 (c).

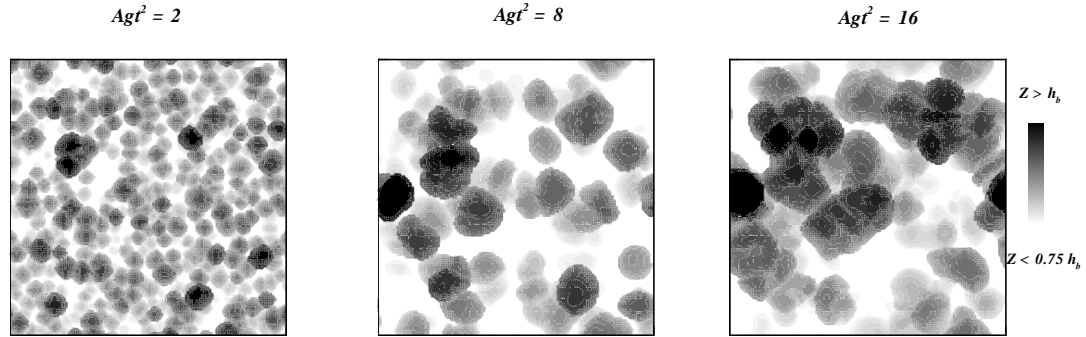


Figure 6.5. Bubble fronts  $Z_b(x,z)$  from simulation 6 at early-, mid- and late times ( $A_t g t^2 = 2, 8,$  and  $16$ ).

The 1% iso-surfaces of the volume fraction  $f_l$  are shown in figure 6.4 for  $A_t g t^2 = 1, 10,$  and  $19$  from simulation 11. By the end of the simulation, there are 1 – 2 leading bubbles dominating the flow. Figure 6.5 shows the evolution of bubble fronts  $Z_b(x,z)$  (defined as iso-surfaces of  $f_l = 0.01$ ) at three stages of the R-T evolution for simulation 6 ( $A_t g t^2 = 2, 8,$  and  $16$ ). Only the bubble fronts with  $Z_b > 0.75 h_b$  are shown in figure 6.5. There are  $\sim 120$  bubbles at  $A_t g t^2 = 2$ , which coalesce to  $\sim 9$  large bubbles by the end of the calculation. It is evident that even at  $A_t g t^2 = 16$ , the bubbles do not approach  $L = 1$  cm, the box dimension. Thus, we may assume that the flow is not affected by the boundary conditions right up to the end of the calculation. The radial autospectra  $E_{Z_b}(k)$  of the bubble front function  $Z_b(x,z)$  may be defined as

$$\int_0^{\infty} E_{Z_b}(k) dk = \langle Z_b^2 \rangle - \langle Z_b \rangle^2, \quad (6.2.7)$$

where  $\langle \bullet \rangle$  denotes averaging over the  $x$ - $z$  plane. The radial autospectra was obtained by averaging the 2D power spectra of  $Z_b(x,z)$  rotated through 15 angles. The results are

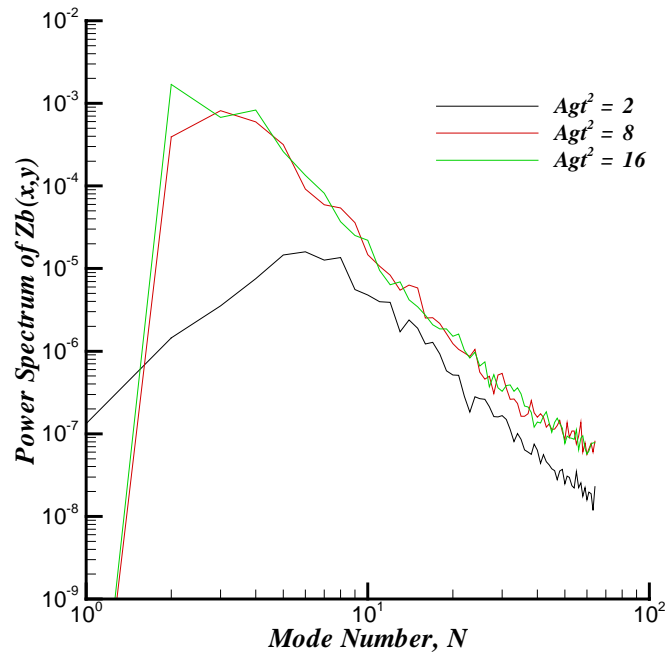


Figure 6.6. Azimuthally averaged power spectra of bubble fronts  $Z_b(x,z)$  from simulation 6 at early-, mid-, and late times ( $A_t g t^2 = 2, 8, \text{ and } 16$ ).

plotted in figure 6.6 for  $A_t g t^2 = 2, 8, \text{ and } 16$ . There is no dissipative range in these spectra due to the absence of small-scale information in the definition of  $Z_b(x,z)$ . Consistent with the emergence of large-scale structures at late-time, the spectral peak shows movement towards lower wavenumbers. However, at  $A_t g t^2 \sim 2$  for instance, the spectral peak is at  $N \sim 4$  which is higher than the imposed value of  $N_{min} = 2$  for this case. This is caused by modulation effects due to the presence of bubbles of different sizes. To determine

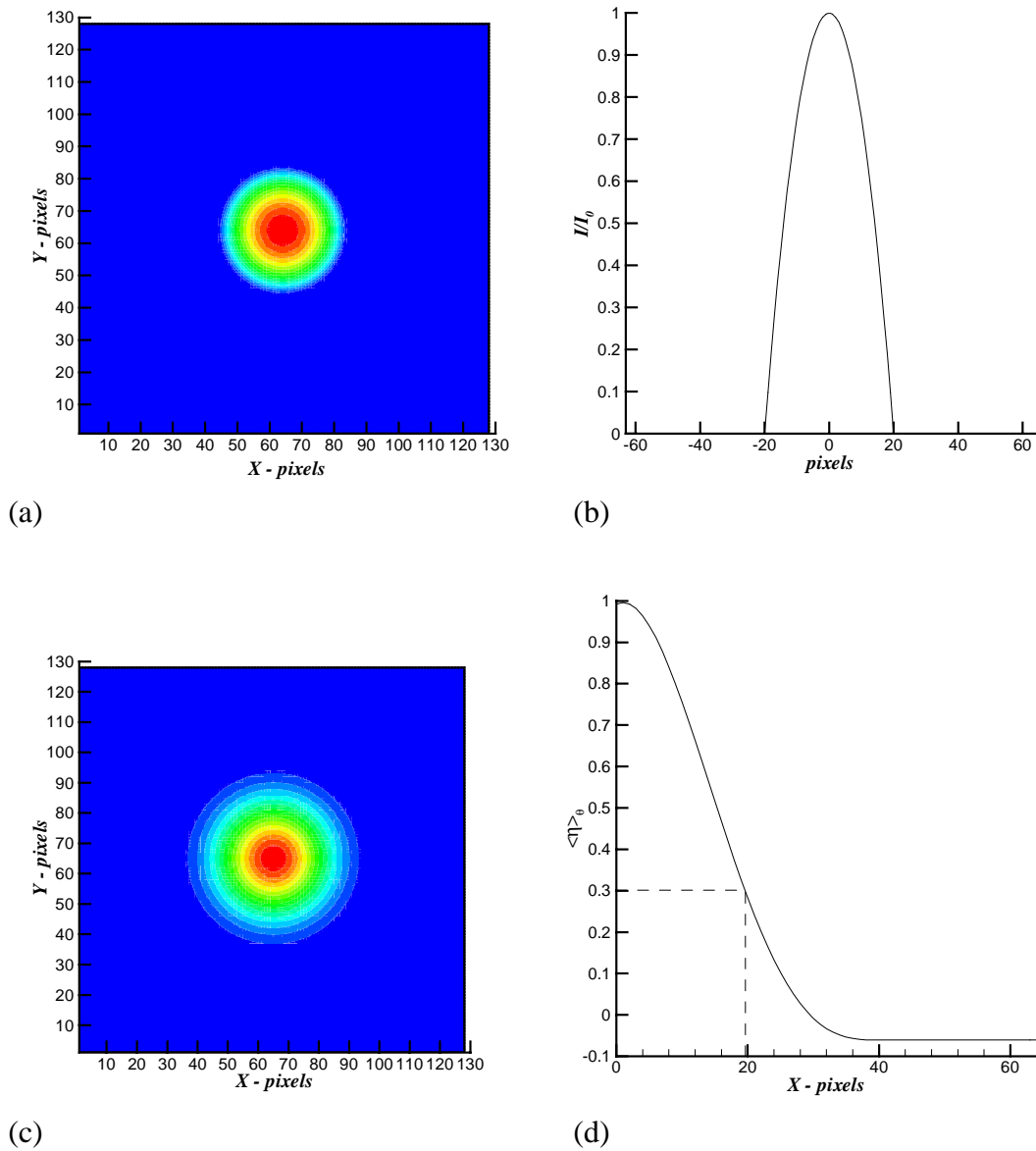


Figure 6.7. (a) Test image of radius 20 pixels with a parabolic (b) intensity profile. (c) Autocorrelation contours of test image from (a) and the azimuthally averaged radial profile (d) showing a radius of 20 pixels.

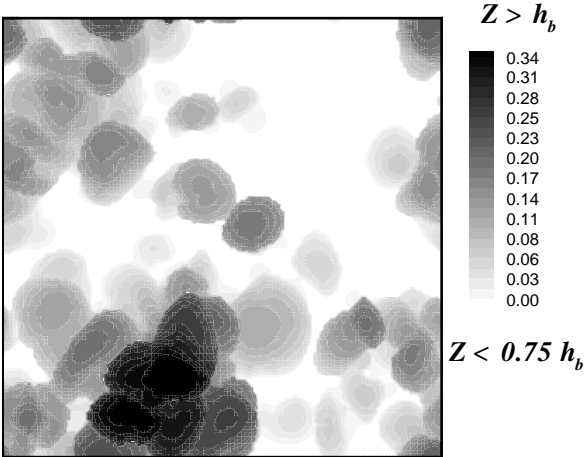


quantities such as the Froude number and the self-similar parameter  $\beta_b$ , it is essential to estimate the average diameters of the R-T bubbles without such modulation effects. We thus use an autocorrelation-based technique (developed in Dimonte *et al.* 2003) to determine the average bubble diameters for different  $A_1 g t^2$ .

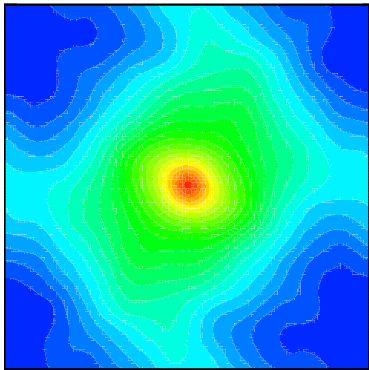
The 2D non-dimensional, autocorrelation function  $\eta(x, z)$  of  $Z_b(x, z)$  is defined as

$$\eta(x, z) = \frac{\sum (Z_b(x', z') - \langle Z_b \rangle)(Z_b(x' + x, z' + z) - \langle Z_b \rangle)}{\sum (Z_b(x', z') - \langle Z_b \rangle)^2}. \quad (6.2.8)$$

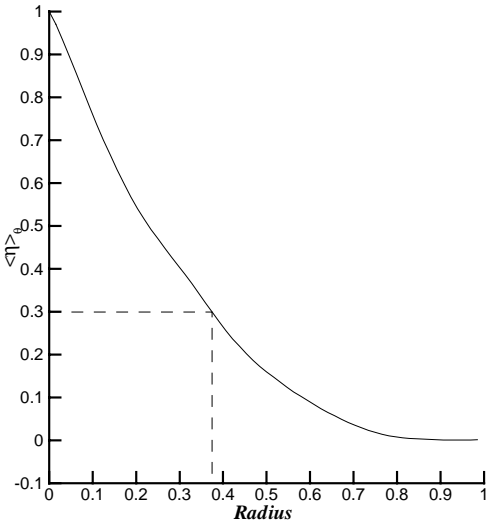
The azimuthal average of  $\langle \eta \rangle_\theta$  is then obtained by averaging  $\eta(x, z)$  rotated through 24 angles. This technique was applied to test images with objects of known diameters, and it was found that the radial location where  $\langle \eta \rangle_\theta$  dropped to a value of 0.3 approximately corresponded to the mean radius of the test objects. Figure 6.7 (a) and (b) show the test object and the radial profile of intensity (along the dashed line) respectively. A parabolic intensity profile was chosen for the test image to reproduce the observed profiles of the bubble fronts. The autocorrelation function  $\eta(x, z)$  and its azimuthal average  $\langle \eta \rangle_\theta$  are shown in figures 6.7 (c) and (d) respectively. The threshold value of 0.3 captures the radius of the test object ( $\sim 20$  pixels). This procedure was repeated with test objects of different diameters, and with multiple objects in a single frame. The error using this technique for these cases was determined to be  $\sim \pm 15\%$ . A sample image of the bubble fronts from case 11 at  $A_1 g t^2 = 22$ , is shown in figure 6.8 (a). The results of the autocorrelation technique applied to this image are plotted in figures 6.8 (b) and (c) as



(a)



(b)



(c)

Figure 6.8. (a) Bubble front image  $Z_b(x,z)$  from simulation 11 at  $A_t g t^2 = 22$ . (b) Autocorrelation contours of the bubble front field from (a) and the azimuthally averaged radial profile (c).

the  $\eta(x,z)$  contours and radial profile of  $\langle \eta \rangle_\theta$  respectively. Applying the 0.3 cutoff, we determine the average bubble diameter for this image to be  $\sim 0.76$  cm.

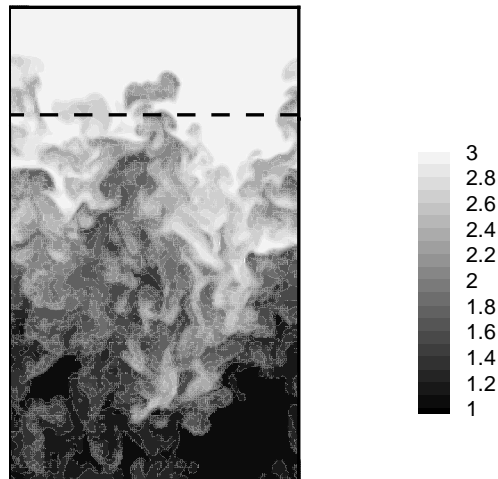


Figure 6.9. Vertical slice of density contours from simulation 6 at  $A_t g t^2 = 17$ . The average bubble density and velocities are computed within the volume enclosed by the leading bubble tip and the dashed line.

The Froude number definition from section 6.1 does not take in to account the dilution of bubble density through entrainment of heavy fluid and subsequent molecular diffusion. This process increases the effective density of the bubbles, and will have to be accounted for in the definition of the Froude number (see Dimonte *et al.* 2003). This is evident from a vertical slice of density contours from simulation 6 at  $A_t g t^2 = 17$  (figure 6.9), which shows the leading bubbles as gray rather than black. The effective bubble density is then obtained by averaging the density within a volume defined as the region

Simulation	Effective Fr #
1	$0.94 \pm 0.18$
2	$1.47 \pm 0.41$
3	$1.07 \pm 0.09$
4	$1.16 \pm 0.14$
5	$1.04 \pm 0.20$
6	$1.02 \pm 0.13$
7	$1.16 \pm 0.17$
8	$1.05 \pm 0.20$
9	$1.09 \pm 0.12$
10	$1.12 \pm 0.09$
11	$1.13 \pm 0.18$
12	$0.94 \pm 0.11$

Table 6.4 The effective Froude numbers from the simulations.

bounded by  $\max(Z_b(x,z))$ , and a radius of  $D_b/2$  (in figure 6.9, this is approximately the region between the leading bubble tip and the dashed line). The bubble velocity is similarly obtained by averaging the vertical velocities within this volume, which takes in to account the velocity of heavier fluid trapped within and co-moving with the bubble. The Froude number definition from (6.1.3) is then modified as

$$Fr_{eff} = v_b \sqrt{\frac{\rho_1}{\rho_1 - \rho_b} \frac{2}{gD_b}}, \quad (6.2.9)$$

where  $\rho_2 < \rho_b < \rho_1$ . For the density field shown in figure 6.9,  $\rho_b = 2.69$ ,  $v_b = 0.049$ ,  $Fr_0 = 0.29$ , and  $Fr_{eff} = 0.79$ . A histogram of Froude numbers from all the simulations obtained through these two methods (figure 6.10) show that the effective Froude number agrees closely with the experimentally observed values of  $\sim 1$  (Dimonte & Schneider (1996) report  $Fr \sim 0.9$  from their LEM experiments). Table 6.4 contains the effective

Froude number averaged over the self-similar time window described earlier in this section for all the simulations reported here. We will use the effective  $Fr$  number in the verification of equations (6.1.5) and (6.1.6) below.

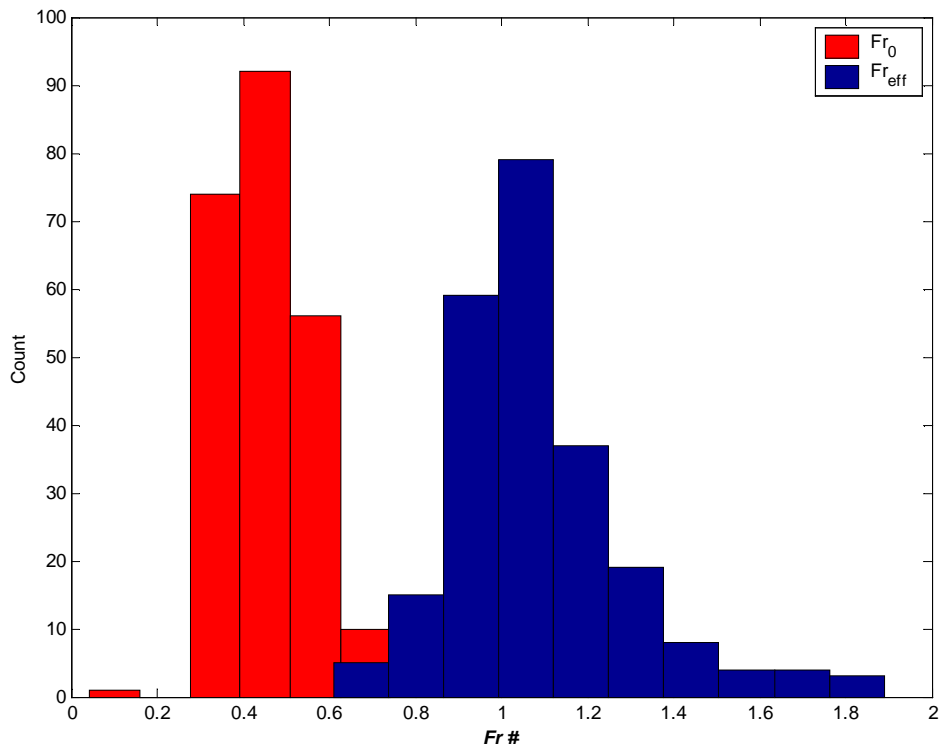
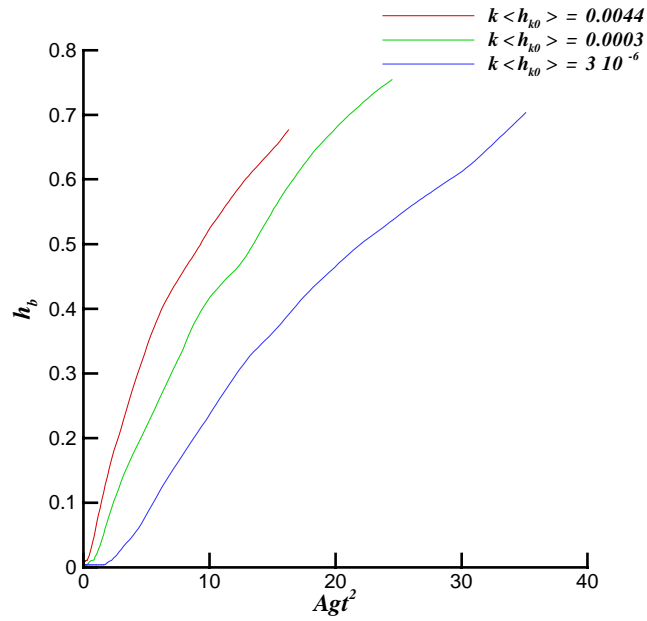
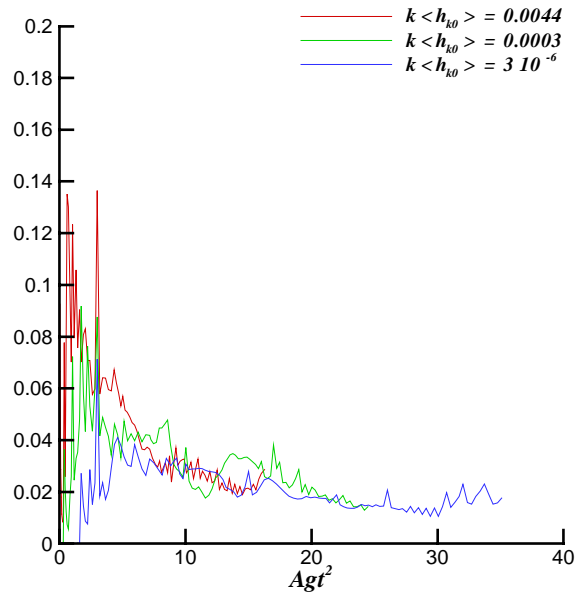


Figure 6.10. Histogram of Froude numbers from the 12 simulations.

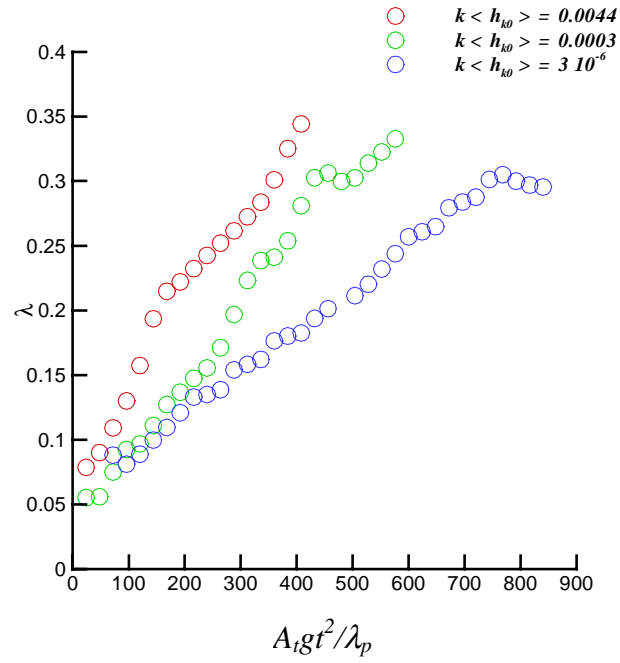


(a)

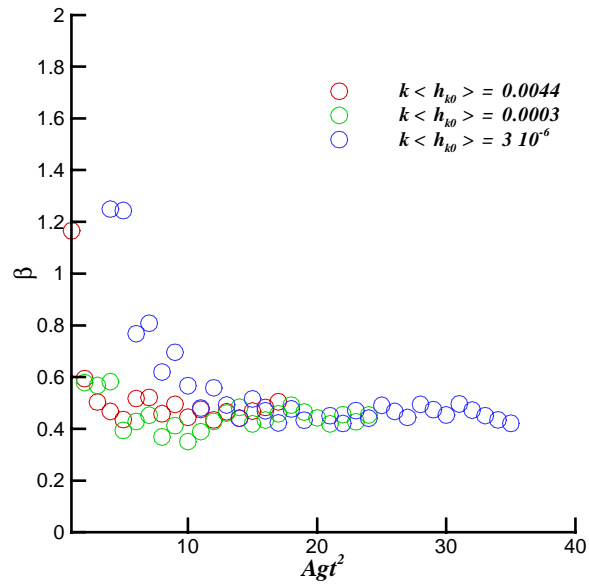


(b)

Figure 6.11. Effect of  $k \langle h_{0k} \rangle$ : (a) Evolution of bubble amplitude,  $h_b$  for cases 6,7, and 8 ( $k \langle h_{0k} \rangle = 0.0044, 0.0003, \text{ and } 3 \times 10^{-6}$ ) (b) Evolution of  $\alpha_b$  for cases 6,7, and 8 ( $k \langle h_{0k} \rangle = 0.0044, 0.0003, \text{ and } 3 \times 10^{-6}$ ).



(a)



(b)

Figure 6.12. Effect of  $k \langle h_{0k} \rangle$ : (a) Evolution of bubble wavelength,  $\lambda_b$  for cases 6,7, and 8 ( $k \langle h_{0k} \rangle = 0.0044, 0.0003, \text{ and } 3 \times 10^{-6}$ ) scaled to  $\lambda_p$ . (b) Evolution of  $\beta_b$  for cases 6,7, and 8 ( $k \langle h_{0k} \rangle = 0.0044, 0.0003, \text{ and } 3 \times 10^{-6}$ ).

### 6.3 Effect of Initial Amplitudes

Cases 1 through 8 constitute the study of the effect of initial amplitudes on self-similar bubble quantities  $\alpha_b$  and  $\beta_b$ . All of these cases had an initial spectral slope of  $k^{-2}$ , while the minimum imposed modes ranged from 1 to 3. To isolate the effect of the initial amplitudes, Figure 6.11 (a) shows the evolution of bubble amplitudes for cases 6,7, and 8 which all had the same values of  $N_{min} = 2$ . Simulation 6, which had,  $k\langle h_{0k} \rangle = 0.0044$  grew the fastest, while the bubble amplitude from simulation 8 with  $k\langle h_{0k} \rangle = 3 \times 10^{-6}$  took up to  $A_1 g t^2 \sim 35$  to reach 0.7cm. The corresponding growth constant  $\alpha_b$  was determined as the derivative of  $h_b$  with respect to  $A_1 g t^2$ , and is plotted in figure 6.11 (b). In the self-similar regime ( $t_k \leq t \leq t_{mc}$ ),  $\alpha_b$  is nearly constant for the three cases, but the different values indicate a dependence on the initial amplitudes. This dependence will be quantified later in this section. Using the bubble diameters determined from the autocorrelation technique, the bubble wavelengths  $\lambda_b$  can be obtained from Daly's parametrization (discussed in section 1.2) as,

$$\lambda_b \approx D_b \frac{\rho_1 + \rho_2}{\rho_1}. \quad (6.3.1)$$

$\lambda_b$  for the three cases are shown in figure 6.12 (a) as a function of the non-dimensional parameter  $A_1 g t^2 / \lambda_p$ . Here,  $\lambda_p$  is the peak wavelength from (6.2.3). For instance, by  $t = t_k$  for case 6,  $h_b \sim 0.4 \lambda_p$  which indicates that this mode is near saturation. It is clear that at  $A_1 g t^2 = A_1 g t_{mc}^2 \sim 15$ ,  $\lambda_p \sim 0.32$ , or  $\lambda_{min} \sim 0.5$  indicating the onset of mode coupling. The self-similar parameter  $\beta_b = \lambda_b / h_b$  is plotted in figure 6.12 (b) and shows a near-constant



Simulation	$\alpha_b$	$\beta_b$
1	$0.058 \pm 0.012$	$0.64 \pm 0.09$
2	$0.028 \pm 0.009$	$0.40 \pm 0.12$
3	$0.088 \pm 0.031$	$0.54 \pm 0.09$
4	$0.048 \pm 0.017$	$0.51 \pm 0.06$
5	$0.086 \pm 0.026$	$0.73 \pm 0.08$
6	$0.046 \pm 0.023$	$0.53 \pm 0.12$
7	$0.036 \pm 0.011$	$0.45 \pm 0.06$
8	$0.024 \pm 0.012$	$0.53 \pm 0.1$
9	$0.041 \pm 0.016$	$0.43 \pm 0.05$
10	$0.037 \pm 0.016$	$0.45 \pm 0.03$
11	$0.034 \pm 0.019$	$0.47 \pm 0.09$
12	$0.030 \pm 0.013$	$0.44 \pm 0.05$

Table 6.5. Self-similar parameters  $\alpha_b$ , and  $\beta_b$  from the simulations.

value of  $\sim 0.4$  for  $t > t_k$ .  $\beta_b$  appears far less sensitive to the initial amplitudes than  $\alpha_b$ . The linear growth of  $\lambda_b$  and the constancy of  $\beta_b$  shows that these calculations have reached self-similarity and remain so until late-time. The mean  $\alpha_b$  and  $\beta_b$  for all the simulations were obtained by averaging for  $t_k \leq t \leq t_{mc}$  and are listed in table 6.5.

In addition to the large-scale effects such as  $\alpha_b$  and  $\beta_b$ , small-scale effects such as the molecular mixing  $\Theta$  and kinetic energy dissipation were also investigated.  $\Theta$  may be computed from the volume fraction profiles as

$$\Theta = \frac{\int \langle f_1 f_2 \rangle dy}{\int \langle f_1 \rangle \langle f_2 \rangle dy}, \quad (6.3.2)$$

where  $\langle \bullet \rangle$  once again denotes averaging over the  $x$ - $z$  plane. The evolution of  $\Theta$  with  $A_t g t^2$  is shown in figure 6.13 (a) for cases 6,7, and 8.  $\Theta$  for all these cases asymptote to  $\sim 0.8$  consistent with experiments (Wilson & Andrews 2002; Ramaprabhu & Andrews 2003<sup>b</sup>), although at slightly different rates. The self-similar evolution of R-T involves the conversion of the initially available potential energy to kinetic energy as the flow develops. The ratio of the kinetic energy of the flow to the accompanying loss in potential energy is nearly constant for such flows. We use the approach outlined in Ramaprabhu and Andrews (2003)<sup>b</sup>, and Dimonte *et al.*(2003) to define this ratio: Assuming for low  $A_t$ , a linear profile of the volume fractions, and  $h_s \sim h_b = h$ , the loss in potential energy may be written as

$$\Delta P.E. = \int_{-h}^0 (\rho_2 - \langle \rho \rangle) g y dy + \int_0^h (\langle \rho \rangle - \rho_2) g y dy \approx \frac{(\rho_1 - \rho_2) g h^2}{6} \quad (6.3.3)$$

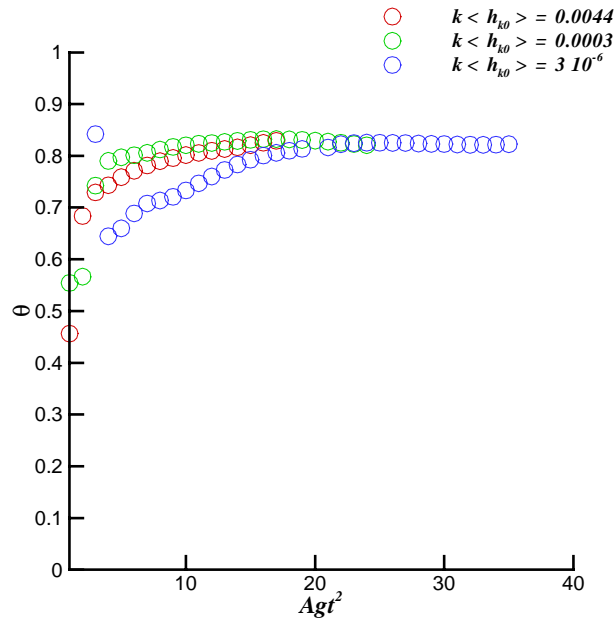
Simulation	$\Theta$	$K.E./\Delta P.E.$
1	$0.72 \pm 0.12$	$0.50 \pm 0.13$
2	$0.81 \pm 0.05$	$0.37 \pm 0.03$
3	$0.70 \pm 0.09$	$0.54 \pm 0.15$
4	$0.73 \pm 0.09$	$0.45 \pm 0.07$
5	$0.63 \pm 0.07$	$0.58 \pm 0.06$
6	$0.75 \pm 0.09$	$0.47 \pm 0.09$
7	$0.80 \pm 0.06$	$0.37 \pm 0.11$
8	$0.78 \pm 0.05$	$0.37 \pm 0.07$
9	$0.82 \pm 0.07$	$0.37 \pm 0.03$
10	$0.81 \pm 0.01$	$0.36 \pm 0.04$
11	$0.82 \pm 0.03$	$0.38 \pm 0.05$
12	$0.81 \pm 0.06$	$0.36 \pm 0.04$

Table 6.6. Molecular mixing parameter  $\Theta$  and  $K.E./\Delta P.E.$  from the simulations.

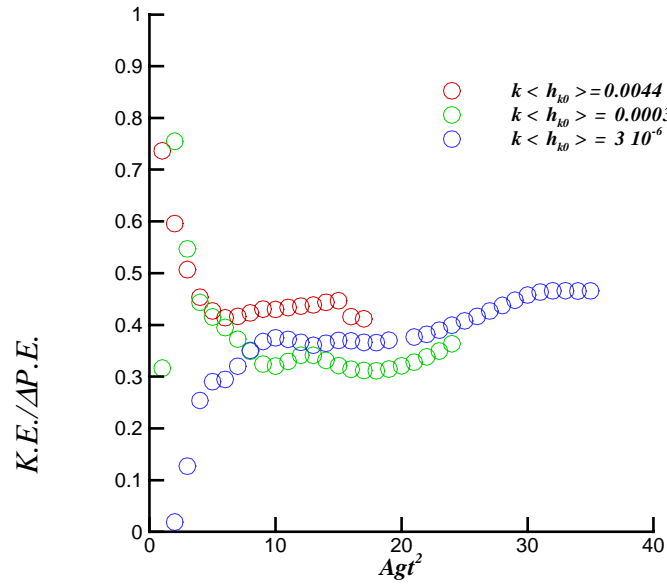
In the above, the error in assuming  $h_s \sim h_b$  results in an overall error in  $\Delta P.E.$  of  $\pm 5\%$  for these calculations. The corresponding gain in kinetic energy is then,

$$K.E. = \frac{1}{2} \int \rho (\bar{\mathbf{v}} \cdot \bar{\mathbf{v}}) dx dy dz, \quad (6.3.4)$$

where the integral is performed over the entire computational domain. The ratio  $K.E./\Delta P.E.$  is plotted for cases 6,7, and 8 in figure 6.13 (b). Note that the fraction of energy dissipated is given by  $1 - K.E./\Delta P.E.$ , and approaches a value slightly greater than 50% for these simulations. This is in good agreement with our experiments (section 4.5; Ramaprabhu & Andrews 2003<sup>b</sup>), which report a value of  $D/P.E. = 49\%$  from simultaneous measurements of density and velocity fields. The values of mixing parameter  $\Theta$  and  $K.E./\Delta P.E.$  are summarized in table 6.6 for the numerical simulations. Simulation 5, which is the most efficient in extracting kinetic energy from the initial



(a)



(b)

Figure 6.13. Effect of  $k\langle h_{0k} \rangle$ : (a) Evolution of molecular mix fraction  $\Theta$  for cases 6, 7, and 8 ( $k\langle h_{0k} \rangle = 0.0044, 0.0003, \text{ and } 3 \times 10^{-6}$ ). (b) Evolution of  $K.E./\Delta P.E.$  for cases 6, 7, and 8.

density distribution ( $K.E./\Delta P.E. \sim 0.6$ ), also has the lowest value for the mixing parameter  $\Theta$ . This simulation had  $N_{min} = 1$ , and the highest growth rate ( $\alpha_b \sim 0.07$ ), which implies the appearance of large scale structures at early times. Thus, the rate of extraction of potential energy could be much higher for this case. In summary, while  $\alpha_b$  appears sensitive to initial conditions,  $\beta_b$  the molecular mixing parameter  $\Theta$ , and  $K.E./\Delta P.E.$  all seem to have little memory of the initial spectral content. The lack of dependence of small-scale features to the initial conditions is also supported by the density fluctuation spectra, discussed in section 6.5.

#### 6.4 Mode Coupling

Simulations 11 and 12 were designed to test the effect of the initial amplitudes on  $\alpha_b$  and  $\beta_b$  in the mode-coupling limit. Both these calculations had amplitudes in modes 16-32 (figure 6.2). The values of  $k\langle h_{0k} \rangle$  were 0.047 and 0.00047 for cases 11 and 12 respectively (note that for these cases,  $k\langle h_{0k} \rangle$  is not constant since a  $k^{-2}$  spectrum was not used; the value reported here was chosen using  $k=2\pi/\lambda_p$ ). From table 6.5, it is clear that  $\alpha_b$  is insensitive to  $k\langle h_{0k} \rangle$  when the large-scales are generated purely by mode-coupling (cases 11 and 12).

These results are summarized in figure 6.14, which is a plot of  $\alpha_b$  vs.  $k\langle h_{0k} \rangle$  for all of the simulations in the initial amplitude study. The closed circles indicate cases 1 – 8

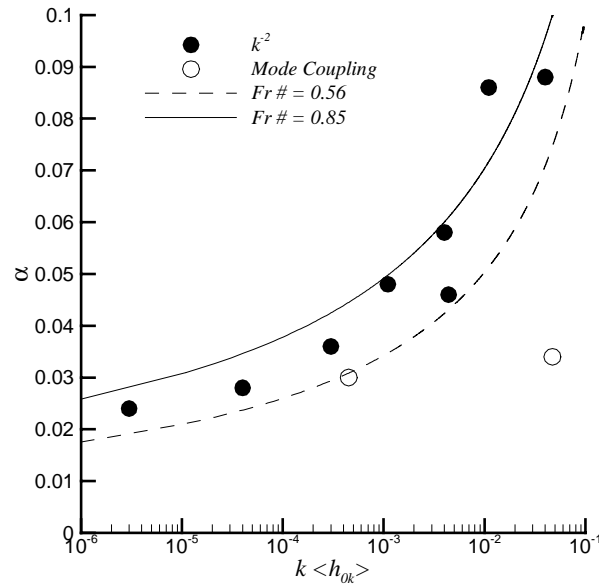


Figure 6.14. Comparison of  $\alpha_b$  from the model and DNS. Open circles show insensitivity of the mode-coupling cases to the initial amplitudes.

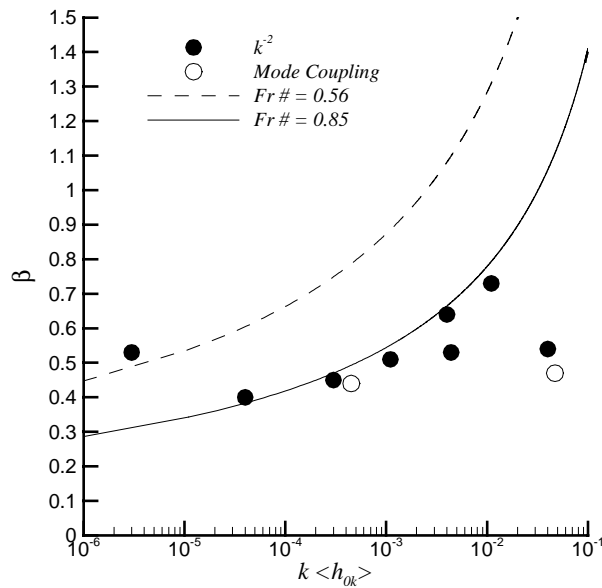


Figure 6.15. Comparison of  $\beta_b$  from the model and DNS. Open circles show insensitivity of the mode-coupling cases to the initial amplitudes.

where long wavelengths were present in the initial spectrum, while the open circles refer to the mode-coupling calculations. The lines represent the model predictions. Figures 6.15, 6.16, and 6.17 are similar plots for  $\beta_b$ ,  $\Theta$ , and  $K.E./\Delta P.E.$   $\alpha_b$  shows a logarithmic dependence on  $k\langle h_{0k} \rangle$  in agreement with equation (6.1.5) which is represented by solid ( $Fr = 0.85$ ) and dashed lines ( $Fr = 0.56$ ). The mode-coupling cases are unaffected by  $k\langle h_{0k} \rangle$ , and one may argue that they set a lower bound for  $\alpha_b$  (within the error bounds reported in table 6.5). As expected for molecular processes,  $\Theta$ , and  $K.E./\Delta P.E.$  are insensitive to initial amplitudes. These findings are further supported by density spectra, which are presented later in this section.  $\beta_b$  does not show any sensitivity to  $k\langle h_{0k} \rangle$  in figure 6.15. One would expect similar behavior for the two parameters, which are coupled in the derivation of equations (6.1.5) and (6.1.6) – Appendix D. This discrepancy may be due to the use of Daly’s formulation (6.3.1) in computing the bubble wavelength. This formulation defines a bubble wavelength as including a bubble and a spike (a crest and a trough of a wave). However, the spikes in this flow behave differently from the bubbles, as they are dependent on the density ratio while the bubbles are not. This difference has to be accounted for in computing the bubble wavelengths by excluding the influence of the spikes. Goncharov (2002) and Hecht, Alon & Shvarts (1994) suggest taking  $\lambda_b \sim D_b$ , which applied to the

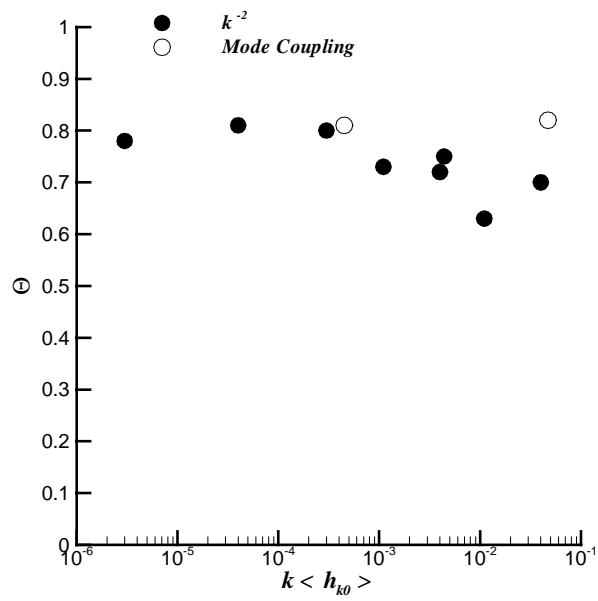


Figure 6.16 Molecular mix fraction  $\Theta$  vs.  $k \langle h_{0k} \rangle$ .

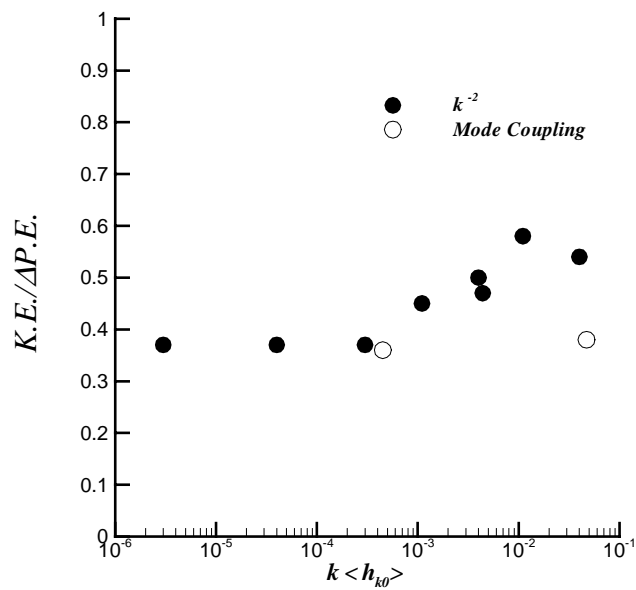


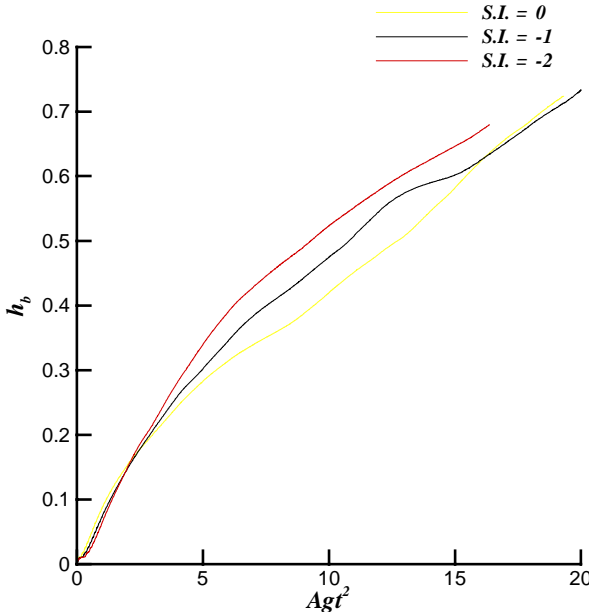
Figure 6.17 Kinetic energy as a fraction of potential energy released vs.  $k \langle h_{0k} \rangle$ .



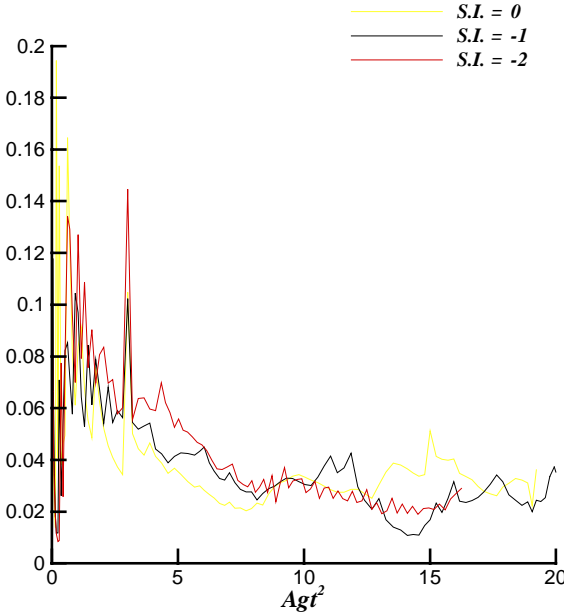
Dimonte model would give  $\beta_b$  independent of  $k\langle h_{0k} \rangle$  and a function of the Atwood number. Work is in progress to refine the model, and test the modified version of equations (6.1.5) and (6.1.6). This includes simulations at different Atwood numbers to study the dependence of  $\beta_b$  on density difference.

### 6.5 Effect of Spectral Index

Figures 6.18 (a) and (b) show the evolution of bubble amplitude  $h_b$ , and  $\alpha_b$  for cases 6, 9, and 10. All three cases had the same  $k\langle h_{0k} \rangle = 0.0044$  and  $N_{min} = 2$ , but spectral indices of  $-2$ ,  $0$  (white noise), and  $-1$  respectively. For  $p = -1$ , and  $p = 0$ ,  $k\langle h_{0k} \rangle$  is not a constant (from the definition of  $\langle h_{0k} \rangle$  from (6.2.2)) and a value based on  $k_p = 2\pi/\lambda_p$  was used. The  $p = 0$  case grows the fastest initially when the high-wavenumbers of the flat spectrum have a higher energy compared with the other cases. The growth is slowed down at late times, when the low-amplitude, low wavenumbers of this spectrum are being sampled by the flow. The corresponding bubble wavelength  $\lambda_b$ , and  $\beta_b$  are plotted in figures 6.19 (a) and (b) respectively, and do not seem to vary significantly with  $p$ . Figure 6.20 and 6.21 are plots of  $\alpha_b$  and  $\beta_b$  averaged over the self-similar time window as a function of the spectral index. The self-similar growth parameters appear to be independent of the spectral slopes of the initial conditions. Note that according to the Dimonte model, the  $p = 0$  and  $p = -1$  cases are not truly self-similar, and  $\alpha_b$  and  $\beta_b$  do not stay constant.



(a)



(b)

Figure 6.18. Effect of  $p$ : (a) Evolution of bubble amplitude,  $h_b$  for cases 6,9, and 10 ( $p = -2, 0,$  and  $-1$ ). (b) Evolution of  $\alpha_b$  for cases 6,9, and 10 ( $p = -2, 0,$  and  $-1$ ).

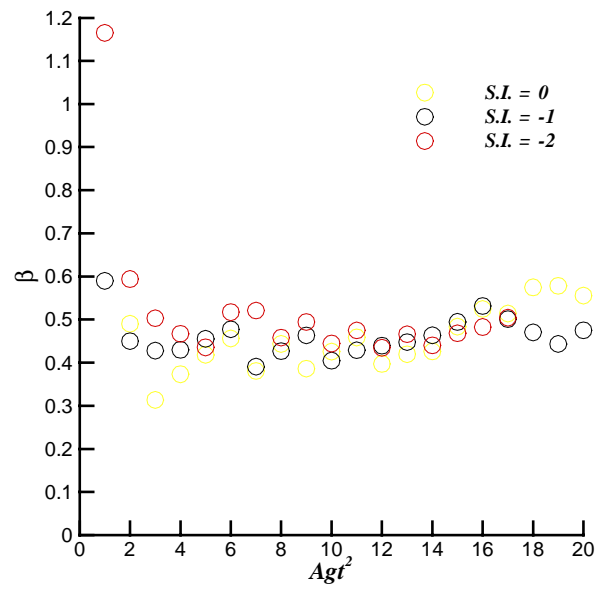
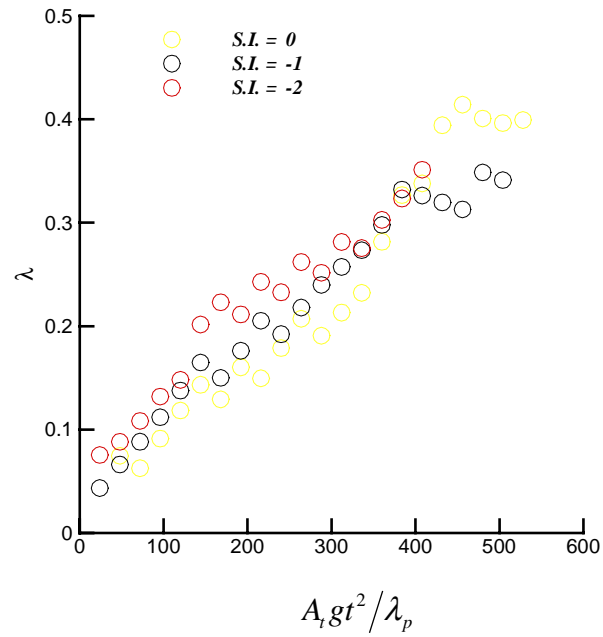


Figure 6.19. Effect of  $p$  (a) Evolution of  $\lambda_b$  for cases 6,9, and 10 ( $p = -2, 0,$  and  $-1$ ) scaled to  $\lambda_p$ . (b) Evolution of  $\beta_b$  for cases 6,9, and 10 ( $p = -2, 0,$  and  $-1$ ).

The volume fraction spectra, is computed from the  $x$ - $z$  distribution of  $f_I$  at  $y=0$  using (Dimonte *et al.* 2003),

$$E_{f_1}(n) = 2\pi n \langle f_1(n)^2 \rangle_\theta, \quad (6.5.1)$$

where  $\langle \bullet \rangle_\theta$  denotes azimuthal averaging. As before, this definition ensures that

$$\int_0^\infty E_{f_1}(k) dk = \langle f_1^2 \rangle - \langle f_1 \rangle^2.$$

Figure 6.22 (a) is a contour plot of  $f_I(x,z)$  at  $y=0$  from simulation 11 at  $A_t g t^2 = 22$ , where the large-scales are generated purely through mode-coupling. The corresponding azimuthally averaged spectra for both the mode-coupling cases are shown in figure 6.22 (b). As described earlier,  $\langle \bullet \rangle_\theta$  was obtained by averaging over 15 angles. The solid line indicates the  $-5/3$  slope, and shows the presence of a short inertial range with  $k^{-5/3}$ . The Reynolds number at  $A_t g t^2 = 22$  may be estimated from (2.3.1) as

$$\text{Re} = \sqrt{\frac{g A_t}{6}} \frac{(h_b + h_s)^{3/2}}{\nu} \approx 925, \quad (6.5.2)$$

where  $\nu$  was determined using the procedure described in section 5.2. Higher resolution simulations at higher Reynolds numbers are expected to give a broader inertial range, than observed here. The corresponding Kolmogorov length scale is

$$\eta_k = \frac{h_b + h_s}{2} \text{Re}^{-3/4}, \quad (6.5.3)$$

and is  $\sim 0.005$  cm. Thus at this late-time, the Kolmogorov scales are not resolved by the current simulations. At higher modenumbers, a dissipative region with a slope of  $-3$  is

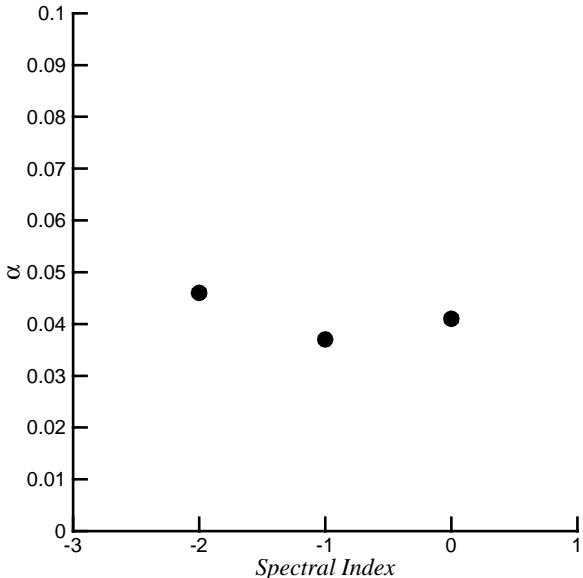


Figure 6.20.  $\alpha_b$  vs.  $p$  for cases 6,9, and 10 ( $p = -2, 0,$  and  $-1$ ).

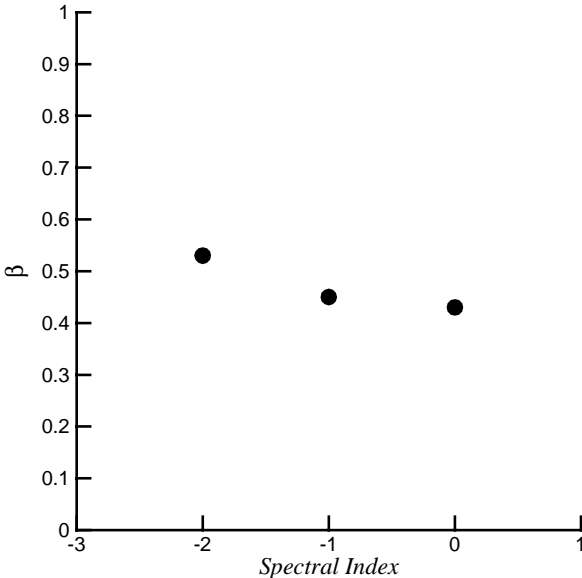
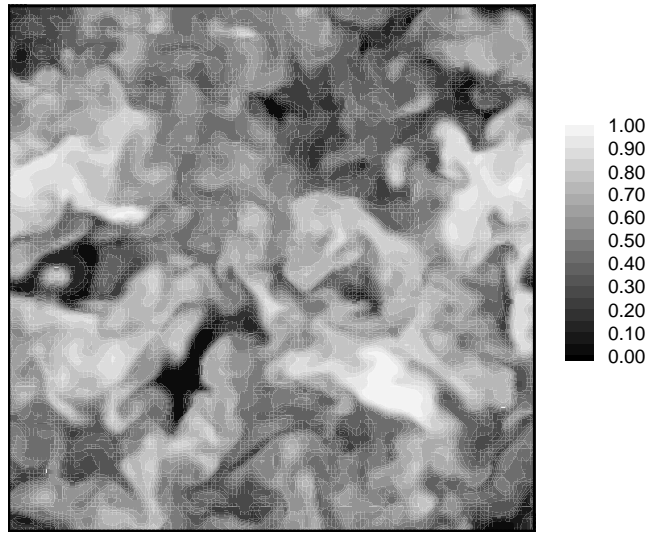


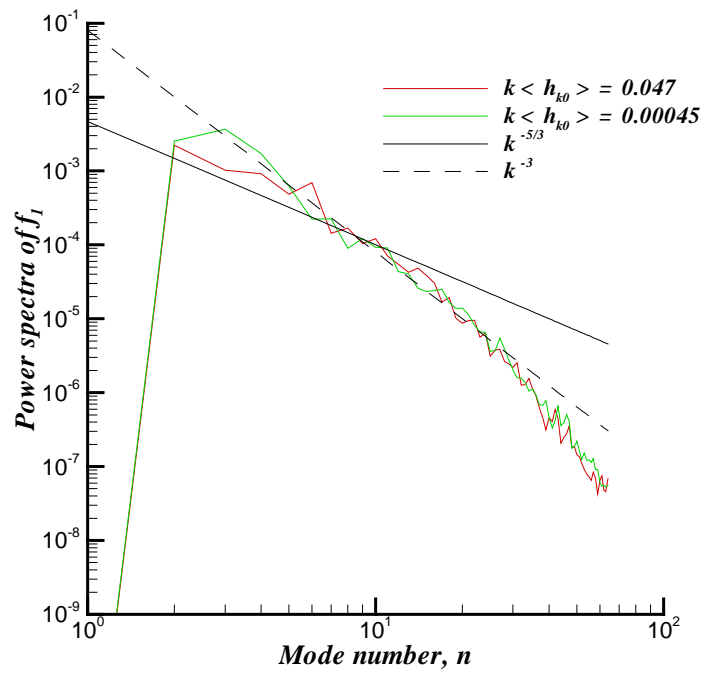
Figure 6.21.  $\beta_b$  vs.  $p$  for cases 6,9, and 10 ( $p = -2, 0,$  and  $-1$ ).

also evident. Although these two cases differed in their initial amplitudes by a factor of 100, their late-time spectra have very similar structures, even in the large-scales.

The azimuthally averaged power spectra from the initial amplitude study, and the spectral index study are shown in figures 6.23 (a) and (b) respectively. Similar to the mode-coupling cases, these spectra have a short inertial range with  $E(k) \sim k^{-5/3}$ , and a steeper dissipative range. The initial amplitude cases have dissimilar structure at the lowest wavenumbers, which is consistent with the different values of the growth constant obtained from these simulations. However, we note that these lowest wavenumbers are likely not well resolved due to the lack of sufficient bubbles/spikes required for averaging. At the higher wavenumbers, all of these calculations have nearly identical energies. This similarity is manifested in the small-scale quantities such as the molecular mixing parameter, the kinetic energy dissipation, which show very little dependence on the initial conditions.

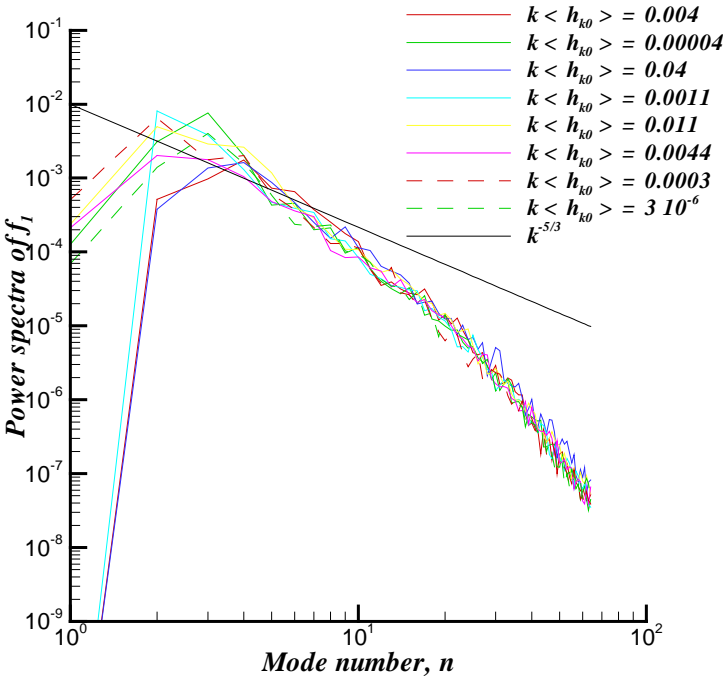


(a)

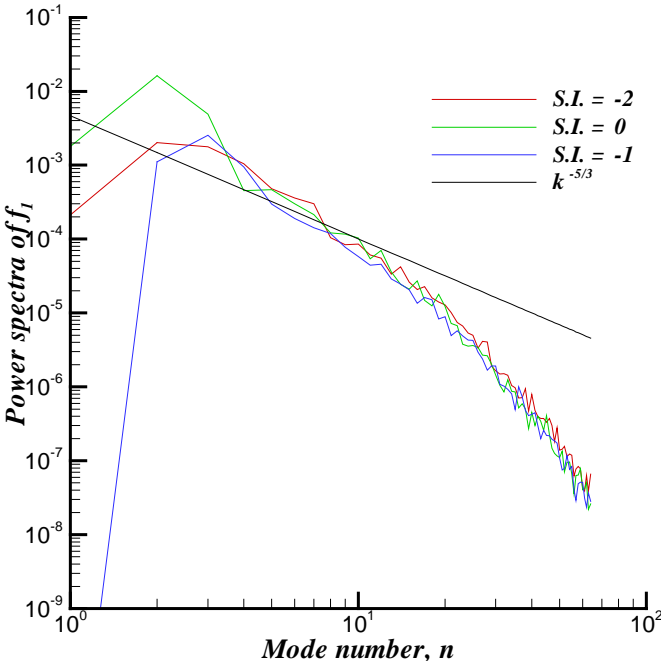


(b)

Figure 6.22 (a). Contours of volume fraction  $f_1$  on a horizontal plane at  $y=0$ . (from case 11) at  $A_1 g t^2 = 22$ . (b) Azimuthally averaged power spectra of  $f_1$  for the two mode-coupling cases 11 and 12.



(a)



(b)

Figure 6.23 Azimuthally averaged power spectra of  $f_1$  from the initial amplitude study (a) and spectral index study (b).



## 7. NUMERICAL SIMULATIONS OF WATER CHANNEL EXPERIMENTS

### 7.1 Formulation of Initial Conditions

High-resolution simulations (128x128x256) initialized with experimentally obtained initial conditions (velocity and density) are described in the following sections. The density data were obtained at  $x \sim 1$  mm, using thermocouples while the velocity data were obtained at  $x \sim 2.5$  cm from the PIV technique. These measurement techniques and the data analysis methods were described earlier in this work. Dimonte *et al.* (2003) have argued that the higher growth rate observed in experiments may be due to the presence of long wavelengths not included in most numerical simulations. In section 6.2, we have demonstrated that when initialized with long wavelengths, numerical simulations can give higher  $\alpha$  values, and exhibit sensitivity to initial conditions. It was also shown that conversely, when such long wavelengths are absent  $\alpha$  approaches a universal lower bound value of  $\sim 0.03$ . Here, we extend this argument to use longer wavelengths measured in experiments to initialize numerical simulations, with the objective of reproducing the experimental growth.

The computational box sizes were chosen to be 15cm x 15cm x 30cm for some simulations and 30cm x 30cm x 60cm for others. The smaller box size has the same depth as the water channel (30 cm), while the larger box size was used to include longer wavelengths that are present in the experiment. The light and heavy fluid densities were

Simulation	Description
Case 1	Density perturbations, with modes 1 – 16, and box size of 15cmx15cmx30cm.
Case 2	Density perturbations, with modes 1 – 16, and box size of 30cmx30cmx60cm.
Case 3	Density perturbations, with modes 1 – 32, and box size of 30cmx30cmx60cm.
Case 4	Velocity perturbations, with modes 1 – 32, and box size of 30cmx30cmx60cm.

Table 7.1 List of simulations initialized with experimental conditions.

set as  $\rho_2 = 1000 \text{ kg/m}^3$ , and  $\rho_l = 1001.5 \text{ kg/m}^3$  respectively to give the same Atwood numbers employed in the experiment ( $A_t \sim 0.00075$ ). The gravitational acceleration was set to  $9.81 \text{ m/s}^2$ . In the following sections, the results are presented entirely in dimensional units to provide a direct comparison with the experimental data – Once again, we employ the Taylor hypothesis to transform the downstream spatial distance in the experiment to time in the simulations using the mean convective velocity ( $4.4 \text{ cm/s}$ ). We note that the experiments are thus effectively two-dimensional since time and the downstream distance can be related through the Taylor hypothesis. Thus, the experiments evolve in two spatial dimensions and one temporal dimension, while the computations are three-dimensional in space.

Table 7.1 is a list of the simulations described here. Cases 1 to 3 were initialized with density perturbations, while case 4 was initialized with velocity data obtained from the PIV technique. Case 1 had a box size of 15cm x 15cm x 30cm, while the other cases had a box size of 30cm x 30cm x 60cm to capture wavelengths up to 30cm that are likely present in the experiment. The density perturbation cases 1 and 2 had energy in modes 1 – 16, while case 3 was initialized with energy in modes 1 – 32 to study the effect of the higher wavenumbers (From section 6.2, the highest resolvable mode was identified as  $n_p \sim 24$ ). We describe below the method used to transform the single-point data (velocity and density) obtained from experiments to planar data required for the simulations. From the power spectra of density fluctuations at  $x = 1\text{mm}$ , the amplitudes of the 32 (16 for case 1) longest modes were used as the approximate values for  $a_k$ ,  $b_k$ ,  $c_k$ , and  $d_k$  in (6.2.1). As  $h_\theta(x, z)$  is calculated by sweeping through the azimuth in wavenumber space, the amplitudes are randomized by multiplying with a randomly generated factor with a mean value of 1, and a standard deviation of 0.3. This value was chosen to ensure that the azimuthally averaged power spectra used in the calculations has the same energy as the single-point power spectra from the experiments:

$$\int \langle h_0(k) \rangle_\theta dk = \int h(k) |_{\text{experiment}} dk . \quad (7.1.1)$$

In the above,  $\langle \bullet \rangle_\theta$  denotes azimuthal averaging. The azimuthally averaged density spectra used in the NS, and the experimental single-point spectra are compared in figure 7.1.

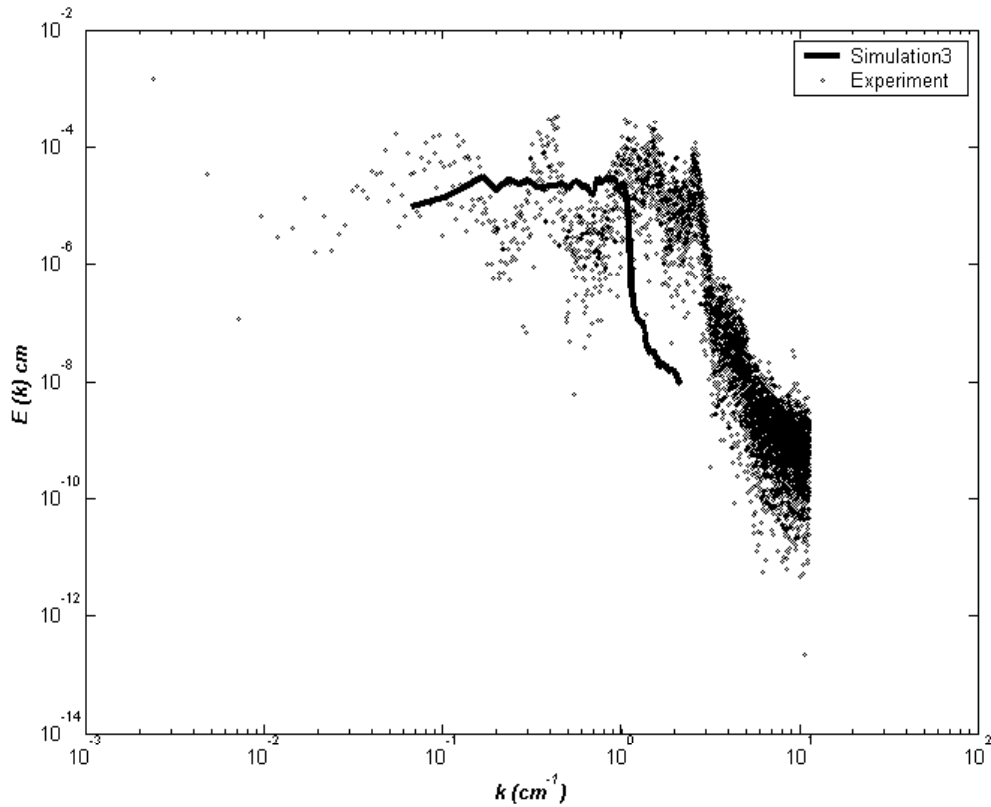


Figure 7.1 Spectra of density initial conditions from the simulations (case 3) and the experiment (thermocouple measurements).

As reported in section 4.3, we believe that the perturbations shed by the splitter plate are primarily velocity fluctuations, which in turn induce density perturbations. Furthermore, most R-T experiments have velocities for their initial perturbations (in contrast to Richtmeyer-Meshkov experiments). In our calculations, the velocity perturbations were initialized as derivatives of the velocity potential function defined as

$$\phi = a_0 \sum_{j=n}^{j=n} \sum_{i=n}^{\max} \frac{a_{ij}}{k_{ij}} \sin(k_i x) \sin(k_j z) \exp(-k_{ij} |y|). \quad (7.1.2)$$

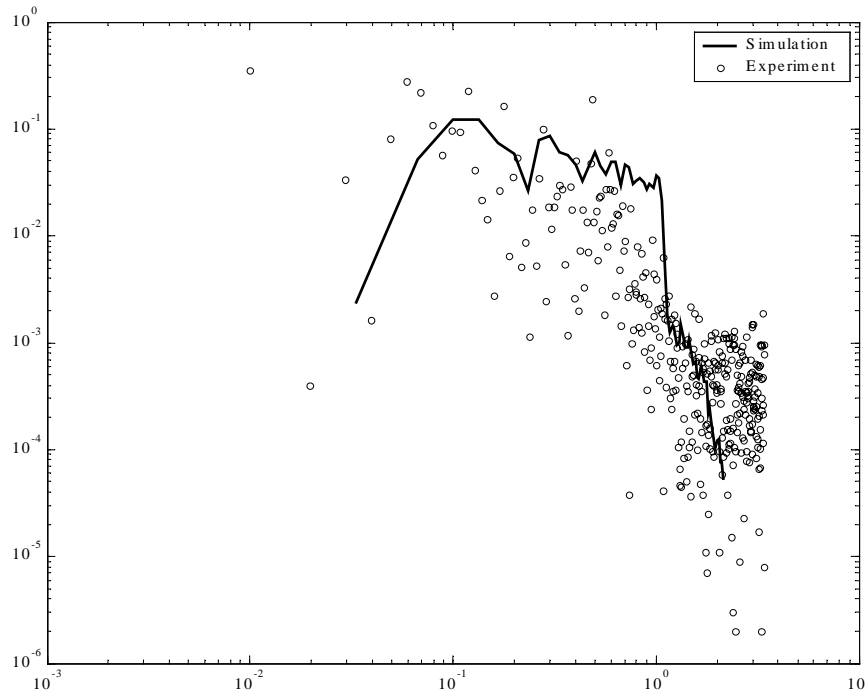
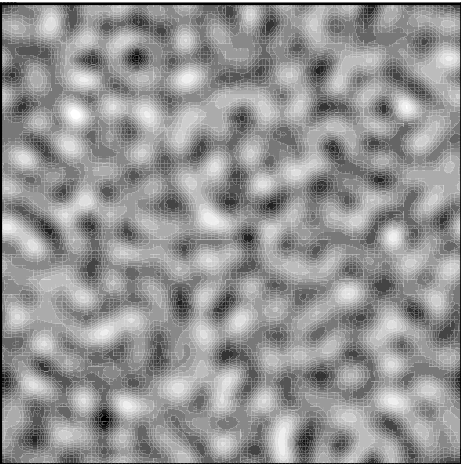
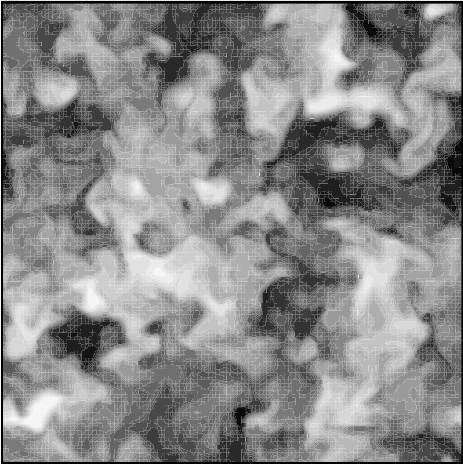


Figure 7.2 Spectra of velocity initial conditions from simulation 4 and the experiment (PIV measurements).

In (7.2.1),  $k_i = 2\pi i / L_x$ ,  $k_j = 2\pi j / L_z$ ,  $k_{ij} = \sqrt{k_i^2 + k_j^2}$ ,  $a_{ij}$  are the modal amplitudes and the velocities were computed as  $\vec{v}' = \nabla \phi(x, y, z)$ . For case 4,  $n_{min} = 1$  and  $n_{max} = 16$ . Since velocity data were collected from the experiment at  $x \sim 2.5$  cm, and not at the edge of the splitter plate ( $x = 0$ ), the values of  $a_{ij}$  were chosen so that the integral of velocity spectra from simulations and experiments agreed at  $x \sim 2.5$  cm. Figure 7.2 is a comparison of the velocity spectra at  $x = 2.5$  cm from simulation 4 and the PIV measurements.



(a)



(b)

Figure 7.3 Contours of volume fraction  $f_l$  from case 2 at  $A_t g t^2 = 0$  (a) and  $A_t g t^2 = 3$  (b) at the interface ( $y = 0$ ).

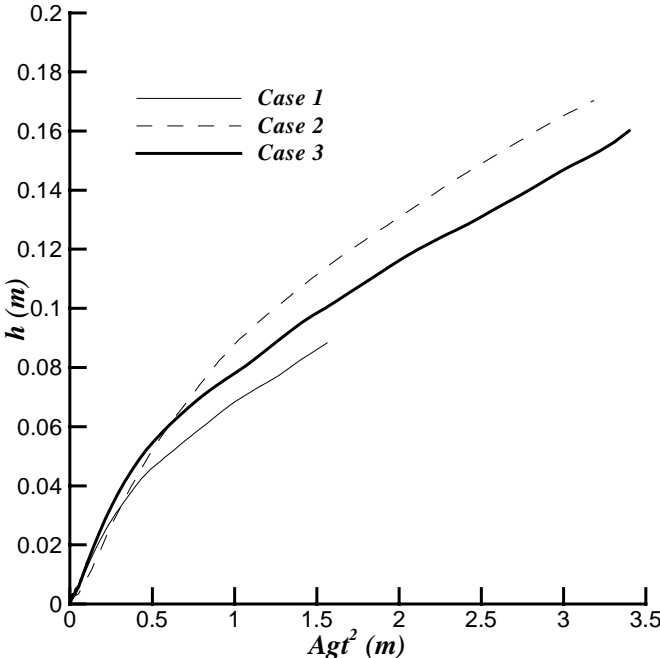


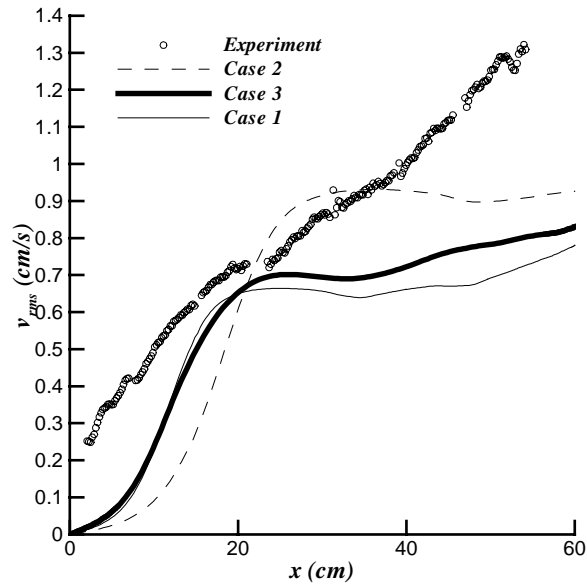
Figure 7.4 Evolution of amplitudes (of bubble) from cases 1,2, and 3.

In both the velocity and density initial spectra, only 16 (cases 1,2, and 4) – 32 (case 3) modes could be resolved. This is the reason for the difference between the spectral structures of the experimental data and the numerical simulations in figures 7.1 and 7.2. Because of the limited resolution of the numerical simulations, the modes in the numerical simulations were initialized as long wavelengths, which dominate the late-time growth.

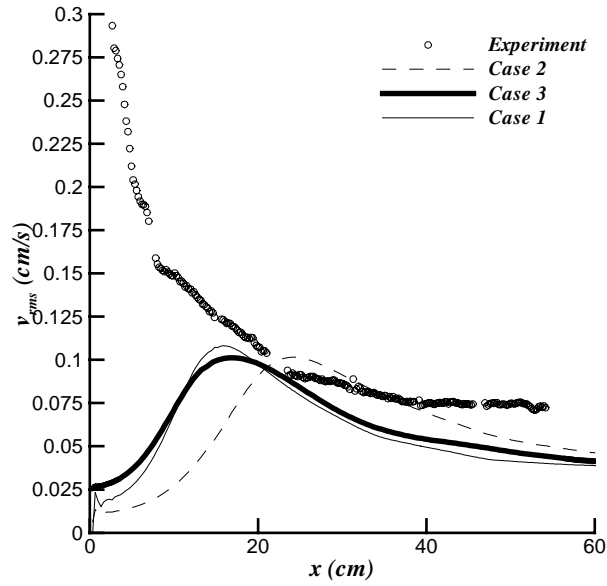
## 7.2 Density Perturbations

Figure 7.3 shows the volume fraction contours from simulation 2 at early and late times ( $A_t g t^2 = 0$  and 3 m respectively). The contour levels shown are the same as that used in figure 6.21 (a). Similar to simulations reported in section 6.2, R-T evolves through coalescence of bubbles leaving only a few bubbles at late time. The evolution of amplitudes of bubbles from cases 1 –3, which were initialized with density perturbations, are shown in figure 7.4. All three cases show a region of linear growth indicating self-similarity. At these low Atwood numbers ( $\sim 0.00075$ ), the bubble and spike amplitudes are roughly equal, and only the bubble amplitudes are shown here. Case 1, which had a box depth of 30 cm was stopped at  $A_t g t^2 \sim 1.5$  m, to minimize the effects of the top and bottom walls on the mix width evolution. Cases 2 and 3 were stopped when the mix width reached  $\sim 16$  cm. Case 3 saturates the fastest, due to the presence of higher wavenumber modes that grow faster according to  $\Gamma \sim \sqrt{A_t k g}$ . Due to the presence of longer wavelengths ( $\sim 30$  cm), simulations 2 and 3 have higher growth rates than simulation 1 which had a longest wavelength of 15 cm.





(a)



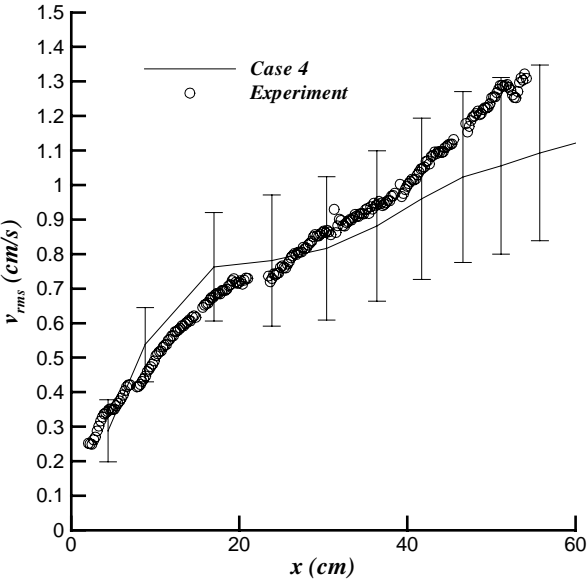
(b)

Figure 7.5 Comparison of r.m.s. of vertical velocity fluctuations (a) and the growth constant  $\alpha$  (b) from simulations initialized with density and the experiment.

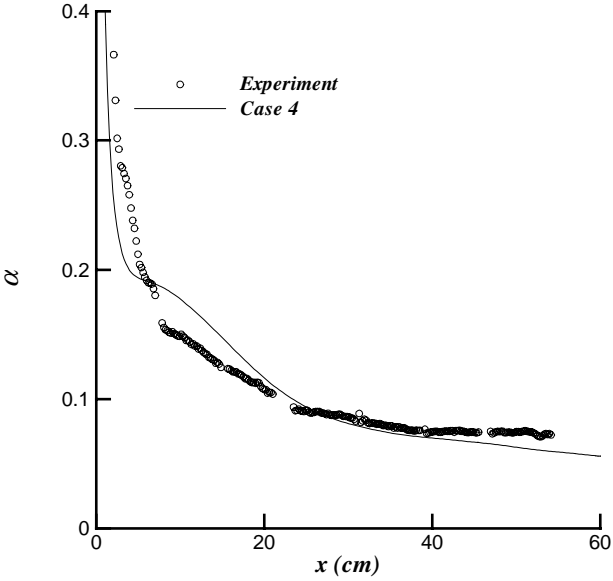
Figure 7.5 is a comparison of the r.m.s. of vertical velocity fluctuations from the simulations 1 – 3 with experimental results from PIV (section 4.2). The simulations report a slower growth rate, and a smaller growth constant  $\alpha$  than the experiments. Here,  $\alpha$  has been calculated according to equation (4.2.1) from the vertical velocity fluctuations at the centerline. The simulations lag behind the experiments in their development, as seen in figure 7.5. However, the experiments have velocity perturbations that accelerate the initial density interface through an *inertial* motion in the vertical direction. In the absence of such an inertial push, density perturbations lag behind the velocity perturbations resulting in the slower growth rate seen in figure 7.5. Note that while the theoretical formulation of an R-T instability involves density perturbations (Chandrasekhar 1961), most experiments have velocity perturbations or a combination of velocity and density modes.

### 7.3 Velocity Perturbations

Simulation 4 was initialized with velocity perturbations given by the gradient of (7.1.2) in modes 1 - 32. The amplitudes were chosen by a trial and error method so that the integral of the velocity spectra at  $x \sim 2.5$  cm agreed with the experimental data reported in section 4.3. The results are compared in figure 7.6 (a) and (b), and show better agreement with the experiments than the density cases. The growth rate  $\alpha$  is not constant due to the structure of the initial spectrum ( $\sim k^0$ ) and approaches 0.06 at late time. At early time, the  $v_{rms}$  amplitudes exceed the experimental value. We attribute this to the



(a)



(b)

Figure 7.6 Comparison of r.m.s. of vertical velocity fluctuations (a) and the growth constant  $\alpha$  (b) from simulation 4 and the experiment.

presence of high-amplitude short wavelengths in the simulations that saturate early. Conversely at late time, when the long-wavelengths dominate, the experimental values for  $v_{rms}$  and  $\alpha$  exceed the simulations. This is due to the higher amplitudes of long-wavelengths in the experiment (figure 7.2). We expect that a  $k^{-2}$  initial spectrum will resolve both these issues. Such simulations are currently underway. In addition, experimental data at the edge of the splitter plate is required to better match the initial conditions. In these simulations, the initial perturbations are two-dimensional (circular in wavenumber space), while we believe the experiments do not have a perturbation field that is statistically isotropic in the horizontal plane (section 4.3). Thus, additional PIV experiments that measure velocity components in the vertical and horizontal planes near the splitter plate are required to accurately model the initial conditions. Finally, another reason for the disagreement between experimental and numerical centerline  $v_{rms}$  values may be the higher uncertainty associated with the numerical simulations. The simulations have only 8 – 10 large-scale structures at late-time, which could result in greater uncertainties of ensemble averages. To quantify this, the standard deviation of

$v_{rms}$  was computed as  $\sqrt{\frac{[\overline{v^4} - (\overline{v^2})^2]}{4\overline{v^2}}}$  (Benedict & Gould 1996), and plotted in figure

7.6 (a). The interfacial horizontal plane was divided in to smaller zones and the uncertainty computed over each of the smaller zones. Then, the true uncertainty is given by the mean of all the sample uncertainties. Zone sizes of 8 x 8 and 16 x 16 were used to test the effect of sample sizes which were found to be negligible. From figure 7.6 (a), it

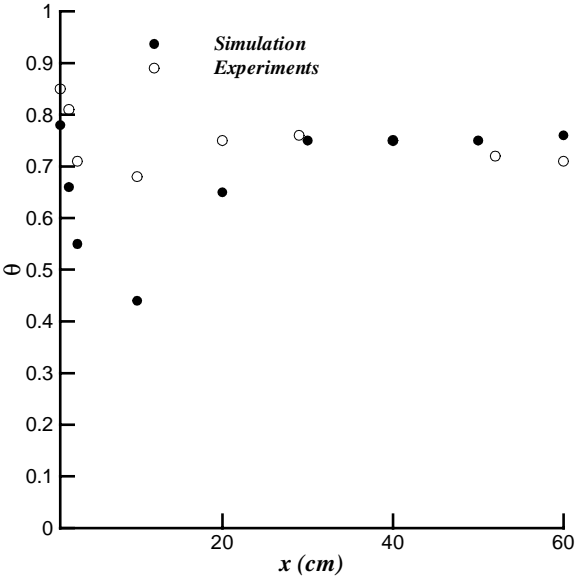


Figure 7.7 Comparison of molecular mix fraction  $\theta$  from simulation 4 and thermocouple measurements.

appears that the discrepancy between the experiments and simulations is within the numerical uncertainty at late-times.

Figure 7.7 is a comparison of the molecular mix fraction parameter  $\theta$  from the thermocouple measurements (section 4.1) and simulation 4. Consistent with the results of section 6.3, the molecular mix fractions are in good agreement, although the large-scale evolutions are different. However at intermediate times,  $\theta$  from the simulation approaches much lower values than the experiments. This difference may be two complementary reasons. The presence of the remnants of the diffuse layer shed from the splitter plate in the experiment contributes to the higher values of  $\theta$  seen here at the early

stages of the downstream evolution. The simulations on the other hand, lack small-scales in their initial conditions due to resolution limitations – the highest mode number imposed was  $n = 32$ . At late-time however, both simulation and experiments approach the same value showing that the MILES technique accurately reproduces the molecular mixing measured in experiments.

## 8. CONCLUSIONS

The evolution of Rayleigh-Taylor (R-T) mixing into self-similar turbulence has been studied using experiments and numerical simulations. The experiments involved high-resolution temperature and velocity measurements of the fully-developed self-similar mix. The velocity measurements were obtained from the Particle Image Velocimetry technique, while temperature measurements were made using a rake of E-type thermocouples placed across the mix. In addition, using the novel PIV-S technique, simultaneous measurements of velocity and density fields have been obtained. The velocity and simultaneous velocity-density measurements reported in this work constitute a first for R-T flows. The spectra and statistical correlations obtained from these measurements should do much to calibrate and refine existing R-T models. In addition, this data may also be used to validate high-resolution Direct Numerical Simulations of such flows. The significant conclusions of this work are summarized below.

- In this experiment, the R-T mix is initialized with a spectrum of velocity perturbations that, after a stage of linear growth, evolve through mode-interactions and successive wavelength saturation. The fully-developed mix grows quadratically in time, with a self-similar structure.

- The self-similarity is evident here through velocity and density frequency spectra that evolve in a shape-preserving manner. The velocity profiles also collapse onto a single curve when normalized by suitable similarity variables.
- Characterization of the mix width development was done using centerline vertical velocity fluctuations, rather than the mix width itself. The quadratic growth rate constant  $\alpha$  was measured at 0.07, which is in good agreement with previous measurements from the experiment using the mix width based on the 5% and 95% threshold for the volume fractions. This verifies observations, and results from velocity and density spectra, that large-scale structures dominate the mixing and contain most of the kinetic energy of the mix. It also implies that relatively simple models, based on driven centerline velocity fluctuations and density fluctuations, would suffice to capture the overall development of the mix.
- The internal structure of the self-similar mix is anisotropic with vertical velocity fluctuations dominating the horizontal (streamwise and transverse) components. The ratio of  $v'/u'$  is  $\sim 2$ , and appears to be constant across the mix, as the mushroom-shaped structures are convected up and down the mix without much change in shape.
- This significant cross-stream (vertical) flux limits the intermittency factor (based on a vorticity threshold) to a maximum of 0.5 at the center of the mix, as opposed to a value of 1 for shear layers. A more natural definition for intermittency for buoyancy-driven turbulence is suggested here based on the two-fluid density fluctuation  $B_2$  and takes a value of 0.5 at the centerline.



- The anisotropy of fluctuating velocity components extends to the Taylor scales, which also exhibit a preferential straining in the direction of gravity. It might be expected that at scales smaller than this, as we approach the Kolmogorov dimensions, the turbulence would be far more isotropic. However, this cannot be directly verified here due to the limitation on spatial resolution of our PIV system. The velocity spectra show a tendency toward convergence at high wavenumbers. This trend is also seen in the strain rate spectrum, which shows that under the influence of an imposed strain field the highest wavenumbers take the least time to return to an isotropic configuration.
- The R-T flow may be viewed as a mixing process for miscible/immiscible fluids of different densities. From an energy budget analysis, it was shown that there is considerable kinetic energy dissipation (~50% of the potential energy loss), which indicates the presence of highly three-dimensional structures necessary for mixing to occur.
- The molecular mix fraction, a local mix parameter, was determined to be  $\sim 0.75$  in the self-similar region. The global mixing efficiency parameter was computed and determined to be  $\sim 0.8$ , a value much higher than that reported from previous experimental work. From assuming a linear density profile, we have shown that for R-T flows, in the self-similar regime, the value of 0.8 indeed can be obtained theoretically.

- The spectral and statistical data presented here may be used to validate direct numerical simulations and turbulence models such as the Reynolds stress models, spectral transport model, and two-fluid models of R-T mixing.

Numerical simulations to investigate the effect of initial conditions on the self-similar evolution of R-T, and the growth constant  $\alpha_b$  in particular were performed. The simulations were designed to verify a model that predicts a logarithmic dependence of  $\alpha_b$  and the self-similar parameter  $\beta_b$  on the non-dimensional initial amplitude  $k\langle h_{0k} \rangle$ . The results from this study are reviewed below.

- $\alpha_b$  was found to vary logarithmically with  $k\langle h_{0k} \rangle$  in agreement with the model for the Froude numbers reported here. In contrast,  $\beta_b$  was found insensitive to  $k\langle h_{0k} \rangle$  contradicting the model predictions. An explanation for this behavior of  $\beta_b$  was provided.
- In the opposite mode-coupling limit where long wavelengths are purely generated by the nonlinear interaction of shorter wavelengths,  $\alpha_b$  and  $\beta_b$  were found independent of  $k\langle h_{0k} \rangle$ . In this limit,  $\alpha_b$  took up a lower bound value of 0.03.
- Numerical simulations to test other effects such as the spectral slopes were also conducted. Three different slopes ( $k^0$ ,  $k^{-1}$ , and  $k^{-2}$ ) were used and the self-similar parameters were found insensitive to changes in the spectral slopes.

- Small-scale effects such as the molecular mix fraction  $\theta$ , and the net kinetic energy dissipation were found to be independent of the initial amplitudes and spectral slopes. This is also reflected in the late-time density spectra from the simulations which show good agreement for all the cases.

Finally, numerical simulations initialized with experimentally obtained initial conditions were performed, and the results were compared with the PIV and thermocouple data. Three simulations were initialized with density perturbations whose amplitudes matched values obtained using a thermocouple at a distance of 1mm from the splitter plate in the experiment. A fourth simulation was initialized with velocity perturbations that had approximately the same amplitudes as those obtained from PIV data at  $x \sim 2.5$  cm. The conclusions from this comparative study are listed below.

- The case with velocity perturbation was found to be in better agreement with the experiments than the density cases. This improvement is believed to be due to the presence of velocity modes that are present in this R-T experiment, that inertially push the density interface at early time, accelerating their growth.
- The late-time growth constant  $\alpha$  approaches 0.06 for this case, a value close to that obtained from the experiments. However, to exactly reproduce the experimental evolution, velocity data in the two vertical planes parallel and perpendicular to the direction of the flow is needed. Such experiments are currently being planned for this experimental facility.

## REFERENCES

Adrian, R.J. 1991 Particle-imaging techniques for experimental fluid mechanics. *Ann. Rev. Fluid Mech.* **23**, 261-304.

Adrian, R. J. 1997 Dynamic ranges of velocity and spatial resolution of particle image velocimetry. *Meas. Sci. Technol.* **8**, 1393 – 1398.

Adrian, R.J., Ferreira, R.T.D.S., & Boberg, T. 1986 Turbulent thermal convection in wide horizontal fluid layers. *Expts. Fluids* **4**, 121-141.

Alahyari, A., & Longmire, E.K. 1994 Particle image velocimetry in a variable density flow: application to a dynamically evolving microburst. *Expts. Fluids* **17**, 434-440.

Alon, U., Hecht, J., Ofer, D., & Schvarts, D. 1995 Power laws and similarity of Rayleigh-Taylor and Richtmeyer-Meshkov mixing fronts at all density ratios. *Phys. Rev. Lett.* **74**, 534 - 537.

Andrews, M.J. 1986 Turbulent mixing by Rayleigh-Taylor instability. Ph.D. thesis, Imperial College, London.

Andrews, M.J. 1995 Accurate computation of convective transport in transient two-phase flow. *Intl. J. Num. Meth. Fluids* **21**, 205 - 222.

Andrews, M.J. 2001 On the effect of molecular mixing on Rayleigh-Taylor mix growth rates. Personal communication.

Andrews, M. J. & Spalding D. B. 1990 A simple experiment to investigate two-dimensional mixing by Rayleigh-Taylor instability. *Phys. Fluids A* **2**, 922-927.

Beale, J.C., & Reitz, R.D. 1999 Modeling spray atomization with Kelvin-Helmholtz/Rayleigh-Taylor hybrid model. *Atomization and Sprays* **9**(6), 623-650.

Benedict, L.H., & Gould, R.D. 1996 Towards better uncertainty estimates for turbulence statistics. *Expts. Fluids* **22**, 129 – 136.

Besnard, D., Harlow, F.H., Rauenzahn, R., & Zemach, C. 1990 Spectral transport model for turbulence. Los Alamos National Laboratory report LA-11821.

Besnard, D., Harlow, F.H., Rauenzahn, R., & Zemach, C. 1992 Turbulence transport equations for variable density turbulence, and a relationship to two-fluid models. Los Alamos National Laboratory report LA-11303.

Birkhoff, G. 1955 Taylor instability and laminar mixing. University of California report No. LA-1862.

Chandrasekhar, S. 1961 *Hydrodynamic and hydromagnetic stability*. Clarendon.

Cherfils, C., & Mikaelian, K.O. 1996 Simple model for the turbulent mixing width at an ablating surface. *Phys. Fluids* **8**(2), 522 - 535.

Collins, R. 1967 The effect of a containing cylindrical boundary on the velocity of a large gas bubble in a liquid. *J. Fluid Mech.* **28**, 97 - 111.

Cook A.W., & Dimotakis, P.E. 2001 Transition stages of Rayleigh-Taylor instability between miscible fluids. *J. Fluid Mech.* **443**, 69 – 99.

Corrsin, S. 1951 On the spectrum of isotropic temperature fluctuations in an isotropic turbulence. *J. Appl. Phys.* **22** (4), 469 – 473.

Dabiri, D., & Gharib, M. 1991 Digital particle image thermometry: the method and implementation. *Expts. Fluids* **11**, 77-86.

Daly, B.J. 1967 Numerical study of two fluid Rayleigh-Taylor instability. *Phys. Fluids* **10**(2), 297-307.

Dalziel, S.B., 1993 Rayleigh-Taylor instability: experiments with image analysis. *Dyn. Atmos. Oceans* **20**, 127-153.

Dalziel, S.B., Linden, P.F., & Youngs, D.L. 1999 Self-similarity and internal structure of turbulence induced by Rayleigh-Taylor instability. *J. Fluid Mech.* **399**, 1 – 48.

Dankwerts, P.V. 1952 The definition and measurement of some characteristics of mixtures. *Appl. Sci. Res.* **3** (A), 279 – 296.

Davies, R.M. & Taylor, G.I. 1950 The mechanics of large bubbles rising through extended liquids and through liquids in tubes. *Proc. R. Soc. London Ser. A* **200**, 375 - 390.

Dimonte, G. 2003 Dependence of turbulent Rayleigh-Taylor (RT) instability on initial conditions. Submitted to *Phys. Rev. E*.

Dimonte, G., & Schneider, M. 1996 Turbulent Rayleigh-Taylor instability experiments with variable acceleration. *Phys. Rev. E* **54** (4), 3740-3743.

Dimonte, G., & Schneider, M. 2000 Density ratio dependence of Rayleigh-Taylor mixing for sustained and impulsive acceleration histories. *Phys. Fluids* **12**(2), 304-321.

Dimonte, G., Youngs, D.L., Dimits, A., Weber, S., Marinak, M., Calder, A.C., Fryxell, B., Biello, J., Dursi, L., MacNiece, P., Olson, K., Ricker, P., Rosner, R., Timmes, F., Tufo, H., Young, Y-N., Zingale, M., Wunsch, S., Garasai, C., Robison, A., Andrews, M.J., & Ramaprabhu, P. 2003 A comparative study of the turbulent Rayleigh-Taylor (RT) instability using high-resolution 3D numerical simulations: The Alpha-group collaboration. Submitted to *Phys. Fluids*.

Dimotakis, P.E. 2000 The mixing transition in turbulent flows. *J. Fluid Mech.* **409**, 69-98.

Emmons, H.W., Chang, C.T., & Watson, B.C. 1960 Taylor instability of finite surface waves. *J. Fluid Mech.* **7**, 177-193.

Gebhart, B., Jaluria, Y., Mahajan, R., & Sammakia, B. 1988 *Buoyancy-induced flows and transport*. Hemisphere Publishing Corporation.

Glimm, J., Grove, J.W., Li, X.L., Oh, W., & Sharp, D.H. 2001 A critical analysis of Rayleigh-Taylor growth rates. *J. Comp. Phys.* **169**, 652-677.

Glimm, J., Li, X.L., Menikoff, R., Sharp, D.H., & Zhang, Q. 1990 A numerical study of bubble interactions in Rayleigh-Taylor instability for compressible fluids. *Phys. Fluids A* **2**(11) 2046 - 2054.

Goncharov, V.N. 2002 Analytical model of nonlinear, single-mode, classical Rayleigh-Taylor instability at arbitrary Atwood numbers. *Phys. Rev. Lett.* **88**(13), Art. No. 134502.

Grue, J., Jensen, A., Rusas, P., & Sveen, J.K. 2000 Breaking and broadening of internal solitary waves. *J. Fluid Mech.* **413**, 181 – 217.

Gull, S.F. 1975 The X-ray, optical and radio properties of young supernova remnants. *Monthly Notices of the Royal Astr. Soc.* **171**, 263-278.

Haan, S.W. 1989 Onset of nonlinear saturation for Rayleigh-Taylor growth in the presence of a full-spectrum of modes. *Phys. Rev. A* **39**(11), 5812 - 5825.

Haan, S.W. 1991 Weakly nonlinear hydrodynamic instabilities in inertial fusion. *Phys. Fluids B* **3**(8), 2349 - 2355.

Hecht, J., Alon, U., & Shvarts, D. 1994 Potential flow models of Rayleigh-Taylor and Richtmeyer-Meshkov bubble fronts. *Phys. Fluids* **6**(12), 4019 – 4030.

Jaffe, N.A., Okamura, T.T., & Smith, M.O. 1970 Determination of spatial amplification factors and their application to predicting transition. *AIAA J.* **8**(2), 301-308.

Jevons, W.S. 1857 On the cirrus formation of cloud. *Philosophical Magazine.* **14**(90), 22 – 35.

Kukulka, D.J. 1981 Thermodynamic and transport properties of pure and saline water. M.S. thesis, State University of New York at Buffalo.



LaRue, J.C., Libby, P.A. 1976 Statistical properties of the interface in the turbulent wake of a heated cylinder. *Phys. Fluids* **19**, 1864-1975.

Lawrence, G.A., Browand, F.K., & Redekopp, L.G. 1991 The stability of a sheared density interface. *Phys. Fluids. A* **3**(10), 2360–2370.

Layzer, D. 1955 On the instability of superposed fluids in a gravitational field. *Astrophys. J.* **122**(1), 1 – 12.

Lewis, D.J. 1950. The instability of liquid surfaces when accelerated in a direction perpendicular to their planes II. *Proc. R. Soc. London A* **202**, 81-96.

Linden, P.F. & Redondo, J.M. 1991 Molecular mixing in Rayleigh-Taylor instability. Part I: Global mixing. *Phys. Fluids. A* **3**(5), 1269-1277.

Linden, P.F., Redondo, J.M. & Youngs, D.I. 1994 Molecular mixing in Rayleigh-Taylor instability. *J. Fluid Mech.* **265**, 97-124.

Lindl, J.D. 1998 *Inertial confinement fusion: The quest for ignition and energy gain using indirect drive*. AIP Press.

Mandel, J. 1964 *The statistical analysis of experimental data*. Dover.

Nelder, J. A., & Mead, R. 1965 A Simplex method for function minimization. *Comput. J.* **7**, 308-313.

Oboukhov, A.M. 1949 Structure of the temperature field in turbulent flows. *Izvestiya Akademii Nauk SSSR, Geogr., and Geophys. Ser.* **13**, 58-69.

Park, H.G., Dabiri, D., & Gharib, M. 2001 Digital particle image velocimetry/thermometry and application to the wake of a heated circular cylinder. *Expts. Fluids* **30**, 327-338.

Pope, S. B. 2000 *Turbulent flows*. Cambridge University Press.

Prestridge, K., Rightley, P.M., Vorobieff, P., Benjamin, R.F., & Kurnit, N.A. 2000 Simultaneous density-field visualization and PIV of a shock-accelerated gas curtain. *Expts. Fluids* **29**, 339-347.

Ramaprabhu, P., & Andrews, M.J. 2003a Simultaneous measurements of velocity and density in buoyancy-driven mixing. *Expts. Fluids* **34**, 98-106.

Ramaprabhu, P. & Andrews, M.J. 2003b Experimental investigation of Rayleigh-Taylor mixing at small Atwood numbers. To appear in *J. Fluid Mech.*

Ratafia, M. 1973 Experimental investigation of Rayleigh-Taylor instability. *Phys. Fluids* **16**(8), 1207-1210.

Read, K.I. 1984 Experimental investigation of turbulent mixing by Rayleigh-Taylor instability. *Physica D* **12**, 45-58.

Ristorcelli, J.R. 2001 Personal Communication, Technical staff member, Los Alamos National Laboratory.

Sakakibara, S., & Adrian, R.J. 1999 Whole field measurement of temperature in water using two-color laser induced fluorescence. *Expts. Fluids* **26**, 7-15.

Scarano, F. & Riethmuller, M.L. 1999 Iterative multigrid approach in PIV image processing with discrete window offset. *Expts. Fluids* **26**, 513-523.

Scorer, R.S. 1957 Experiments on convection of isolated masses of buoyant fluid. *J. Fluid Mech.* **2**, 583 - 594.

Simoens, S., Ayrault, M., Primon, R., & Verduzio, G. 1996 Simultaneous velocity and concentration measurements using Mie scattering and particle image velocimetry in a turbulent jet. *Optical Methods and Data Processing in Heat and Fluid Flow*, Mechanical Engineering Publications **1996-3**, 301 – 308.

Snider, D.M., & Andrews, M.J. 1994 Rayleigh-Taylor and shear driven mixing with an unstable thermal stratification. *Phys. Fluids A* **6**(10), 3324-3334.

Snider, D.M., & Andrews, M.J. 1996 The simulation of mixing layers driven by compound buoyancy and shear. *J. Fluids Engr.* **118**(2), 370–376.

Steinkamp, M.J. 1995 Spectral analysis of the turbulent mixing of two-fluids. Ph.D. thesis, University of Illinois at Urbana-Champaign.

Steinkamp, M.J., Clark, T., & Harlow, F.H. 1995 Stochastic interpenetration of fluids. Los Alamos National Laboratory report LA-131016.

Steinkamp, M.J., Clark, T.T., & Harlow, F.H. 1999 Two-point description of two-fluid turbulent mixing – I. Model formation. *Int. J. Multiphase Flow* **25**, 599-637.

Stewart, R.W. 1968 Turbulence (videotape). Encyclopaedia Britannica, Chicago.

Tennekes, H. & Lumley, J.L. 1972 *A first course in turbulence*. MIT Press.

Turner, J.S. 1980 *Buoyancy effects in fluids*. Cambridge University Press.

Waddell, J.T., Niederhaus, C.E., & Jacobs, J.W. 2001 Experimental study of Rayleigh-Taylor instability: Low Atwood number liquid systems with single-mode initial perturbations. *Phys. Fluids* **13**(5), 1263-1273.

Wilson, P.N. 2003 A study of buoyancy and shear driven turbulence within a closed water channel. Ph.D. dissertation, Texas A&M University.

Wilson, P.N. & Andrews, M.J. 2002 Spectral measurements of Rayleigh-Taylor mixing at low-Atwood number. *Phys. Fluids A* **14**(3), 938-945.

Wilson, P., Andrews, M., & Harlow F. 1999 Spectral nonequilibrium in a turbulent mixing layer. *Phys. Fluids A* **11**(8), 2425-2433.

Van Leer, B. 1977 Towards the ultimate conservative difference scheme. IV. A new approach to numerical convection. *J. Comp. Phys.* **23**, 276 - 299.

Young, Y.N., Tufo, H., Dubey, A., & Rosner, R. 2001 On the miscible Rayleigh-Taylor instability: two and three dimensions. *J. Fluid Mech.* **447**, 377-408.

Youngs, D.L. 1984 Numerical simulation of turbulent mixing by Rayleigh-Taylor instability. *Physica D* **12**, 32-44.

Youngs, D.L. 1989 Modelling turbulent mixing by Rayleigh-Taylor instability. *Physica D* **37**, 270-287.

Youngs, D.L. 1991 Three-dimensional numerical simulation of turbulent mixing by Rayleigh-Taylor instability. *Phys. Fluids A* **3**(5), 1312 - 1320.

Youngs, D.L. 1994 Numerical simulation of Rayleigh-Taylor and Richtmeyer-Meshkov instabilities. *Lasers and Particle Beams* **12**, 725-750.

Youngs, D.L. 2003 Application of MILES to Rayleigh-Taylor and Richtmeyer-Meshkov mixing. *16<sup>th</sup> AIAA Computational Fluid Dynamics Conference* 23-26 June 2003 Orlando, Florida. AIAA 2003-4102.

Zhou, Y., 2001 A scaling analysis of turbulent flows driven by Rayleigh-Taylor and Richtmeyer-Meshkov instabilities. *Phys. Fluids* **13**(2), 538 – 543.

## APPENDIX A

### EFFECT OF TURBULENT FLUCTUATIONS OF REFRACTIVE INDEX ON

#### PIV\*

In the following, we discuss and quantify the effect of local refractive index changes on our PIV/PIV-S results. In buoyancy-driven flows, the refractive index changes as a function of the density difference between the two fluids and the distance traveled by the laser beam in the fluid along the line of sight. Optical diagnostic techniques such as PIV, or LDV are susceptible to local changes in refractive index that arise due to changes in the turbulent density field. However, changes in the refractive index were found insignificant in the experiments reported in this work. We substantiate this claim with the following:

1. The density difference in these experiments was very small. While most papers that address the issue of refractive index effects deal with density differences of the order of 3-5% of the mean density (Alahyari & Longmire 1994), in our experiments this value was maintained around 0.1%.
2. The beam travel length of the laser beam was also small in comparison with Alahyari & Longmire (1994), due to the design of the channel, and was 8 cm.
3. Local changes in refractive index would result directly in the blurring of seed particles due to localized bending of light along the line of sight (figure 4 (a), Alahyari & Longmire 1994). Figure A.1 is a comparison of the PIV images with and

---

\* Parts of this section including figures A.1 (a), A.1 (b), A.2 (a) and A.2 (b) have been reprinted with permission from *Expts. Fluids* **34**, 98–106, Ramaprabhu, P., & Andrews, M.J., 2003 Simultaneous measurements of velocity and density in buoyancy-driven mixing. Copyright Springer-Verlag.

without the 5° temperature difference in a *stably* stratified mixing layer. There is no discernible difference in the quality of these images, as opposed to the sharp contrast seen in the figures of Alahyari & Longmire.

4. Furthermore, a quantitative test similar to the one suggested by R.J. Adrian *et al.* (1986) was performed. In this test, a known velocity ( $= 0$  cm/s) was introduced in to the *unstably* stratified mix, in the form of a stationary target (a cylindrical object in this case, figure A.2 (a)).

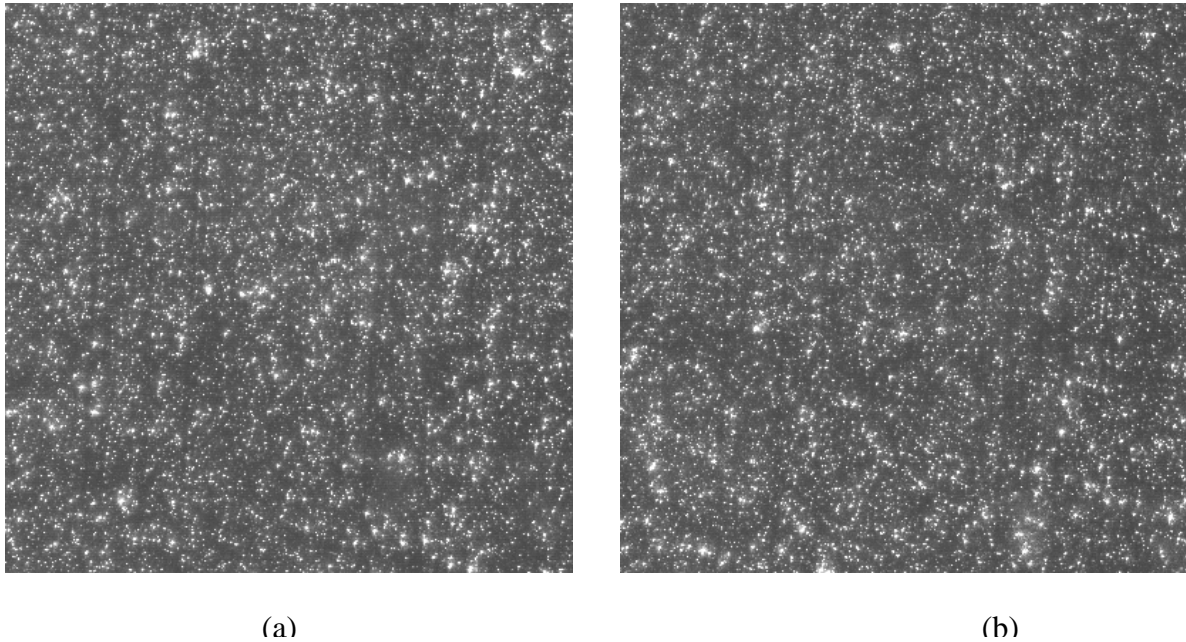
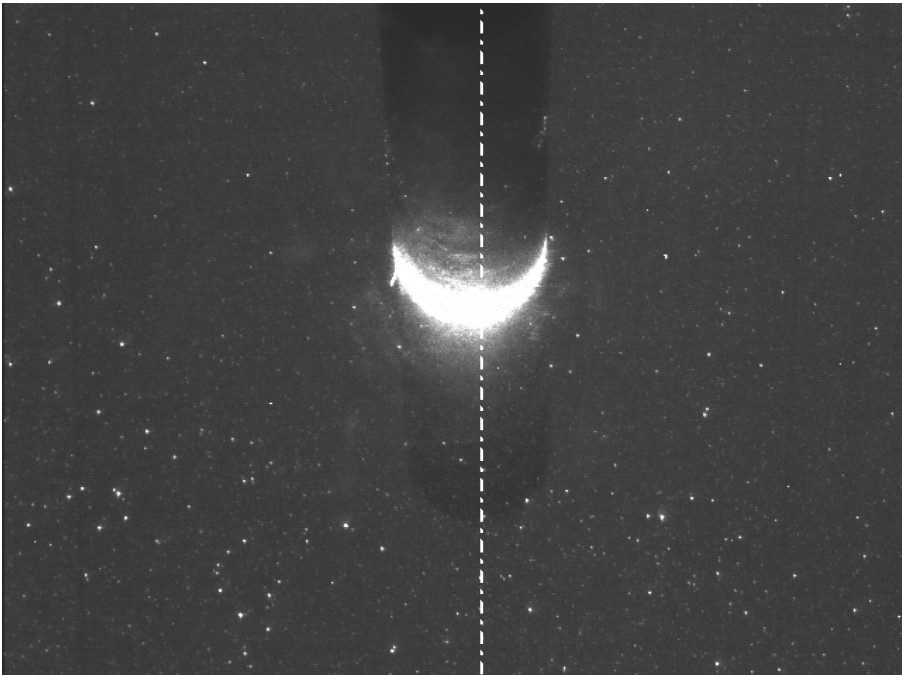


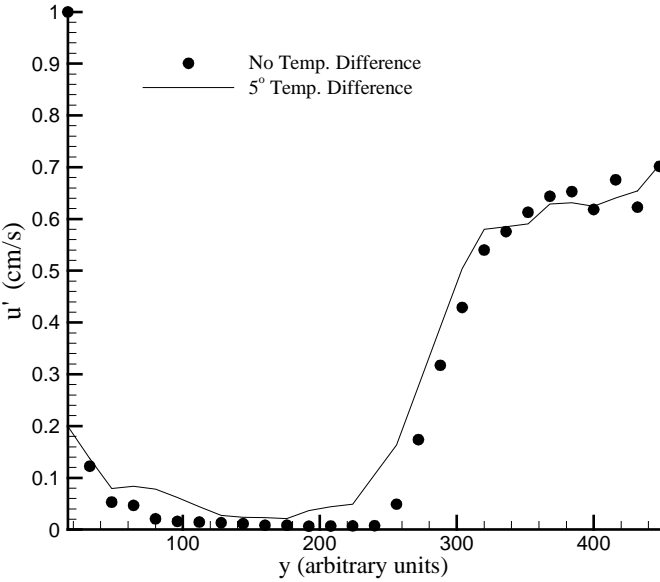
Figure A.1 (a) PIV image with no temperature difference and (b) PIV image with a  $5^\circ$  temperature difference.

In the region occupied by the object, and on its boundaries, we expect to find non-zero r.m.s. velocities if the intensity field is indeed distorted by fluctuations of the refractive index. Figure A.2 (b) is a plot of the  $u'$  velocity profile (along the dotted line in figure A.2 (a), and plotted from the top) computed from the above experiment with and without a  $5^\circ$  temperature difference. As can be seen from figure A.2 (b), there is good agreement between the two cases suggesting that the effects of refractive index changes are minimal.





(a)



(b)

Figure A.2 (a) Stationary object illuminated by laser sheet in an unstably stratified mixing layer. (b) Profiles of  $u'$  along the dotted line in (a).

## APPENDIX B

### $k - \varepsilon$ MODEL VALIDATION

#### *B.1 Preliminaries*

The velocity-density data described in section 3.4 was used to evaluate the buoyancy constant  $C_{\varepsilon 3}$ , of the generic  $k - \varepsilon$  turbulence model. The model uses an eddy-viscosity equation to compute the turbulent transport, while closure is achieved through the  $k - \varepsilon$  equations,

$$\begin{aligned}\frac{\partial \rho}{\partial t} &= \frac{\partial}{\partial y} \left( \frac{\nu_t}{\sigma_t} \frac{\partial \rho}{\partial y} \right) \\ \frac{\partial k}{\partial t} &= \frac{\partial}{\partial y} \left( \frac{\nu_t}{\sigma_k} \frac{\partial k}{\partial y} \right) + G_b + \varepsilon \\ \frac{\partial \varepsilon}{\partial t} &= \frac{\partial}{\partial y} \left( \frac{\nu_t}{\sigma_\varepsilon} \frac{\partial \varepsilon}{\partial y} \right) + C_{\varepsilon 3} \frac{\varepsilon}{k} G_b - C_{\varepsilon 2} \frac{\varepsilon^2}{k}\end{aligned}\tag{B.1.1}$$

where  $k$  is the turbulent kinetic energy,  $\varepsilon$  is the dissipation,  $G_b$  is the buoyancy production term (the shear production term,  $G_s$  has been set to zero),  $\nu_t$  is the turbulent kinematic viscosity, and  $\sigma_t$ ,  $\sigma_\varepsilon$ , and  $\sigma_k$  are the Prandtl numbers.  $C_{\varepsilon 3}$ , the buoyancy coefficient can be determined by transforming the variables in to similarity functions, and solving the transformed equations (Snider & Andrews 1996). The solution of these equations is detailed in the next section.

Using the experimentally obtained kinetic energy and density profiles to fit those obtained from the similarity solution of the above equations,  $C_{\varepsilon 3}$  was found to be  $\sim 0.83$ .

Snider & Andrews (1996) report a value of 0.88 from their similarity solution, and a value of 0.91 from 2D numerical simulations based on the  $k$ - $\varepsilon$  model. Published values of  $C_{\varepsilon 3}$  range from 0.8 to 1.4 depending on the growth rate of the mixing layer  $\alpha$ , with  $C_{\varepsilon 3}$  decreasing with increasing  $\alpha$  - the theoretical value of 0.88 corresponds to  $\alpha \sim 0.07$ . The mix region in the current experiments had a growth rate of  $\sim 0.07$ .

### B.2 Evaluation of $C_{\varepsilon 3}$

The value of  $C_{\varepsilon 3}$  may be determined by transforming the set of equations (B.1.1) in to similarity coordinates, and integrating the resulting equations using approximate profiles of  $k$ ,  $\varepsilon$ , and  $\rho$  (Snider & Andrews 1996). First, the appropriate initial and boundary conditions are imposed.

Initial Conditions:

$$\text{at } t = 0 \text{ for } y \geq 0 : \rho = \rho_1, k = 0, \varepsilon = 0$$

$$\text{at } t=0 \text{ for } y < 0 : \rho = \rho_2, k = 0, \varepsilon = 0$$

Boundary Conditions:

(B.2.1)

$$\text{for } y > h : \rho = \rho_1, k = 0, \varepsilon = 0$$

$$\text{for } y < -h : \rho = \rho_2, k = 0, \varepsilon = 0.$$

The above equations along with (B.1.1) admit a self-similar solution with similarity variables of the form,  $\eta = \frac{y}{t^2}$ ,  $k(t, y) = t^2 \tilde{k}(\eta)$ ,  $\varepsilon(t, y) = t \tilde{\varepsilon}(\eta)$ , and  $\rho(t, y) = \tilde{\rho}(\eta)$ .

Introducing these variables in to (B.1.1), we get

$$\begin{aligned}
-2\eta \frac{d\tilde{\rho}}{d\eta} &= \frac{C_\mu}{\sigma_t} \frac{d}{d\eta} \left( \frac{\tilde{k}^2 d\tilde{\rho}}{\tilde{\varepsilon} d\eta} \right) \\
2\tilde{k} - 2\eta \frac{d\tilde{k}}{d\eta} &= \frac{C_\mu}{\sigma_k} \frac{d}{d\eta} \left( \frac{\tilde{k}^2 d\tilde{k}}{\tilde{\varepsilon} d\eta} \right) + \frac{C_\mu \tilde{k}^2}{\sigma_t \tilde{\varepsilon}} \frac{g}{\rho_0} \frac{d\tilde{\rho}}{d\eta} - \tilde{\varepsilon} \quad (\text{B.2.2}) \\
\tilde{\varepsilon} - 2\eta \frac{d\tilde{\varepsilon}}{d\eta} &= \frac{C_\mu}{\sigma_\varepsilon} \frac{d}{d\eta} \left( \frac{\tilde{k}^2 d\tilde{\varepsilon}}{\tilde{\varepsilon} d\eta} \right) + C_{\varepsilon 3} \tilde{k} \frac{g}{\rho_0} \frac{d\tilde{\rho}}{d\eta} - C_{\varepsilon 2} \frac{\tilde{\varepsilon}^2}{\tilde{k}}
\end{aligned}$$

The self-similar kinetic energy and dissipation profiles are assumed parabolic, while the density profile is assumed to be a linear function of  $\eta$ .

$$\tilde{k} = C_k(1 - \tilde{\eta}^2) \quad \tilde{\varepsilon} = C_\varepsilon(1 - \tilde{\eta}^2) \quad \tilde{\rho} = C_\rho \tilde{\eta} + \tilde{\rho}_2 \quad (\text{B.2.3})$$

where  $C_k$  and  $C_\varepsilon$  are constants, and  $\eta$  has been normalized by a self-similar length scale  $C_w = h/t^2$ ,

$$\tilde{\eta} = \frac{y}{h} \quad (\text{B.2.4})$$

For a linear density profile,  $C_\rho = (\rho_1 - \rho_2)/2$ . Substituting for  $\tilde{k}$ ,  $\tilde{\varepsilon}$ , and  $\tilde{\rho}$  in to (B.2.2) and integrating the resulting equations for  $-1 < \tilde{\eta} < 1$ , the following expressions for the constants can be obtained:

$$\begin{aligned}
C_k &= \frac{B^2 C_\rho^2 (C_{\varepsilon 2} - C_{\varepsilon 3})^3}{(4C_{\varepsilon 2} - 3)^2 (4C_{\varepsilon 3} - 3) C_\mu} \frac{\sigma_t}{C_\mu} & C_\varepsilon &= \frac{(4C_{\varepsilon 3} - 3)}{(C_{\varepsilon 2} - C_{\varepsilon 3})} C_k & B &= -\frac{C_\mu g}{\sigma_t \rho_0} \\
C_w &= \frac{C_\mu (4C_{\varepsilon 2} - 3)}{B C_\rho \sigma_t (C_{\varepsilon 2} - C_{\varepsilon 3})} C_k \quad (\text{B.2.5})
\end{aligned}$$

Solving the above equations with the standard values for the  $k$ - $\varepsilon$  constants ( $C_\mu = 0.09$ ,  $C_{\varepsilon 2} = 1.92$ ,  $\sigma_t = 0.6$ ),  $C_{\varepsilon 3}$  was determined to be 0.88 (Snider & Andrews 1996).

An empirical value for  $C_{\varepsilon 3}$  can be determined by fitting the experimentally obtained kinetic energy and density profiles to match the variables in (B.2.3) and then evaluating the coefficients  $C_k$  and  $C_\rho$  (figures B.1 and B.2). The resulting values are then substituted in to the equation for  $C_w$  (B.2.5), which is then solved for  $C_{\varepsilon 3}$ . This approach yielded a value of 0.83 for  $C_{\varepsilon 3}$ .

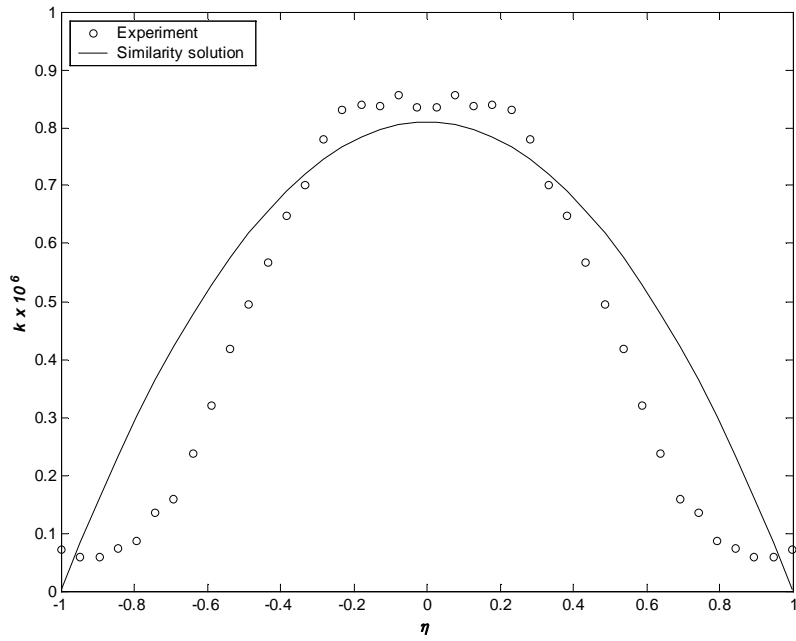


Figure B.1. Comparison of  $k$  - profiles from experiment and similarity analysis.

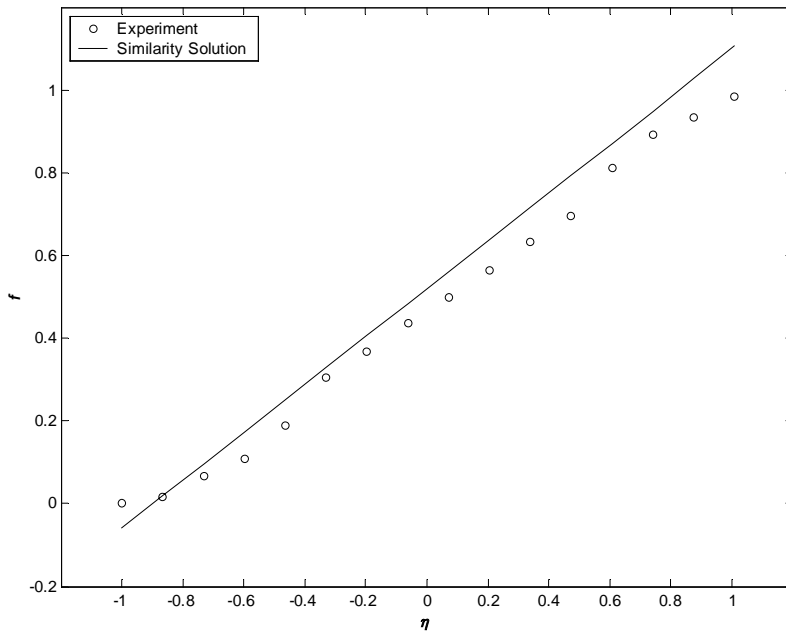


Figure B.2. Comparison of volume fraction profiles from experiment and similarity analysis.

## APPENDIX C

### THE ALPHA-GROUP STUDY

#### *C.1 Comparison of RTI-3D with Benchmark Codes*

In this section, we summarize the results from a comparative study (Dimonte *et al.* 2003) of several benchmark codes commonly used in numerical simulations of R-T including *RTI-3D*. All of the codes were initialized with the same initial conditions, and the results

RT code	Description
TURMOIL 3D	Compressible Eulerian code, 3 <sup>rd</sup> order Van Leer method, staggered Cartesian grid, and 2 <sup>nd</sup> order time integration..
FLASH	Adaptive mesh, compressible Eulerian code, uses a Piecewise Parabolic Method which uses parabolas to interpolate between nodes.
WP/PPM	Also uses PPM, but with a higher-order scheme. Solves the Euler equations, and can handle shocks and discontinuities.
NAV/STK	Solves the Navier-Stokes equation where the viscosity is specified explicitly.
HYDRA	Eulerian code with capability to handle radiation, and with an artificial viscosity to handle shocks and mix the fluids, but an Interface Reconstruction approach can be invoked to keep the fluids separate. Also uses the Van Leer method.
ALEGRA	Can perform in both Eulerian and Lagrangian modes. Capable of Interface Reconstruction.
RTI-3D	A 3 <sup>rd</sup> order Eulerian code, with Van Leer flux limiters. Uses artificial numerical viscosity. Detailed description provided in section 5.1.

Table C.1 List of RTI codes.

were compared. The initial conditions were the same as used for simulation 11 in section 6.4 (one of the mode-coupling cases), with energies in modes 16-32. Table C.1 provides a short description of the codes used in this study. With the exception of ALEGRA and HYDRA, all of these of codes use an artificial (Euler) or a physical (Navier-Stokes) viscosity to mix the fluids. ALEGRA and HYDRA have Interface Reconstruction (IR) which keeps the fluids separate without mixing, thus simulating the two-fluid problem.

The numerical viscosities from the seven codes are given in table C.2. The viscosity from the RTI-3D code is the lowest of all the simulations, thus giving a growth rate closest to the analytical solution for the single mode calculations presented in section 5.2. Figure C.1 is a plot of the integral mix width (6.2.6) from the simulations as a function of the self-similar length scale  $A_i g t^2$  (a), and  $A_i g t^2 / \lambda_p$  (b). The solid lines indicate high-resolution 256x256x512 simulations, while the dashed lines represent the lower resolution 128x128x256 cases. The simulations with RTI-3D were at a resolution of 128x128x256. The filled circles are the results from the LEM experiments (Dimonte & Schneider 2000), and show a higher growth rate possibly due to the presence of long wavelengths in the experiments. In C.1 (b), when normalized by  $\lambda_p$ , the growth from the experiments is much higher since the LEM experiments probably had a much smaller dominant wavelength not resolved by the simulations. The transition to quadratic growth for the simulations occurs around  $A_i g t^2 / \lambda_p \sim 50$ . The highest growth rates among the



R-T Code	Numerical viscosity
TURMOIL 3D	0.23
FLASH	
WP/PPM	0.28
NAV/STK	0.53
RTI-3D	0.22
ALEGRA (without IR)	0.50
HYDRA (without IR)	0.31

Table C.2 Viscosities of the RT codes.

numerical simulations were for the cases with IR (ALEGRA and HYDRA), since they had no specified viscosity. The corresponding bubble amplitudes are shown in figures C.2 (a) and (b) plotted against  $A_t g t^2$  and  $A_t g t^2 / \lambda_p$  respectively. The growth constant  $\alpha_b$  is determined by differentiating  $h_b$  with respect to  $A_t g t^2$ , and is shown in figures C.3 (a) and (b) and show a region of nearly constant  $\alpha_b$  for all the simulations indicating self-similarity. The bubble growth constants from the simulations are given in table C.3 and show good agreement between all the simulations.

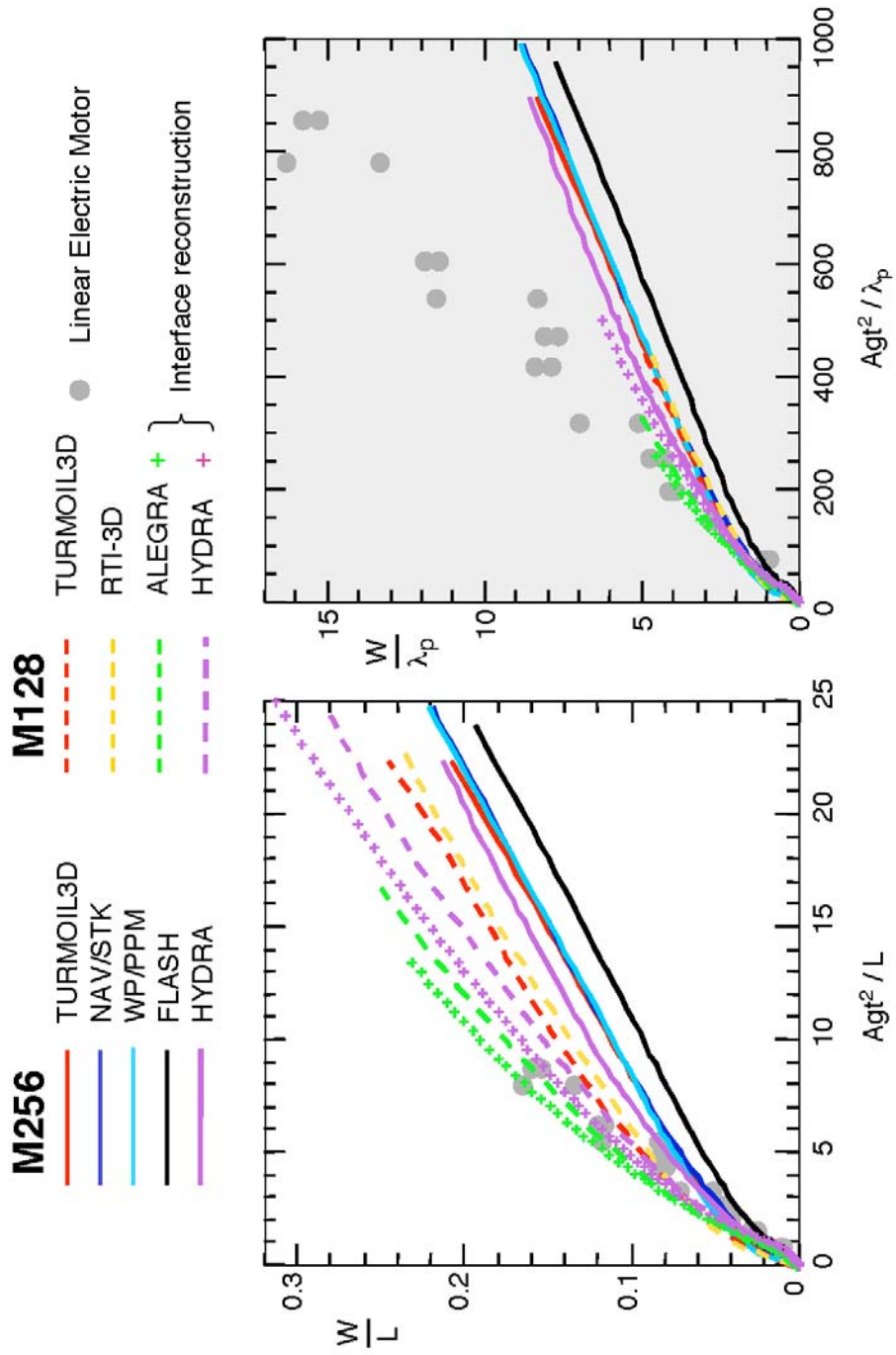


Figure C.1. Evolution of the integral mix-width  $W$  from the numerical simulations as a function of (a)  $Agt^2$ , and (b)  $Agt^2/\lambda_p$ .

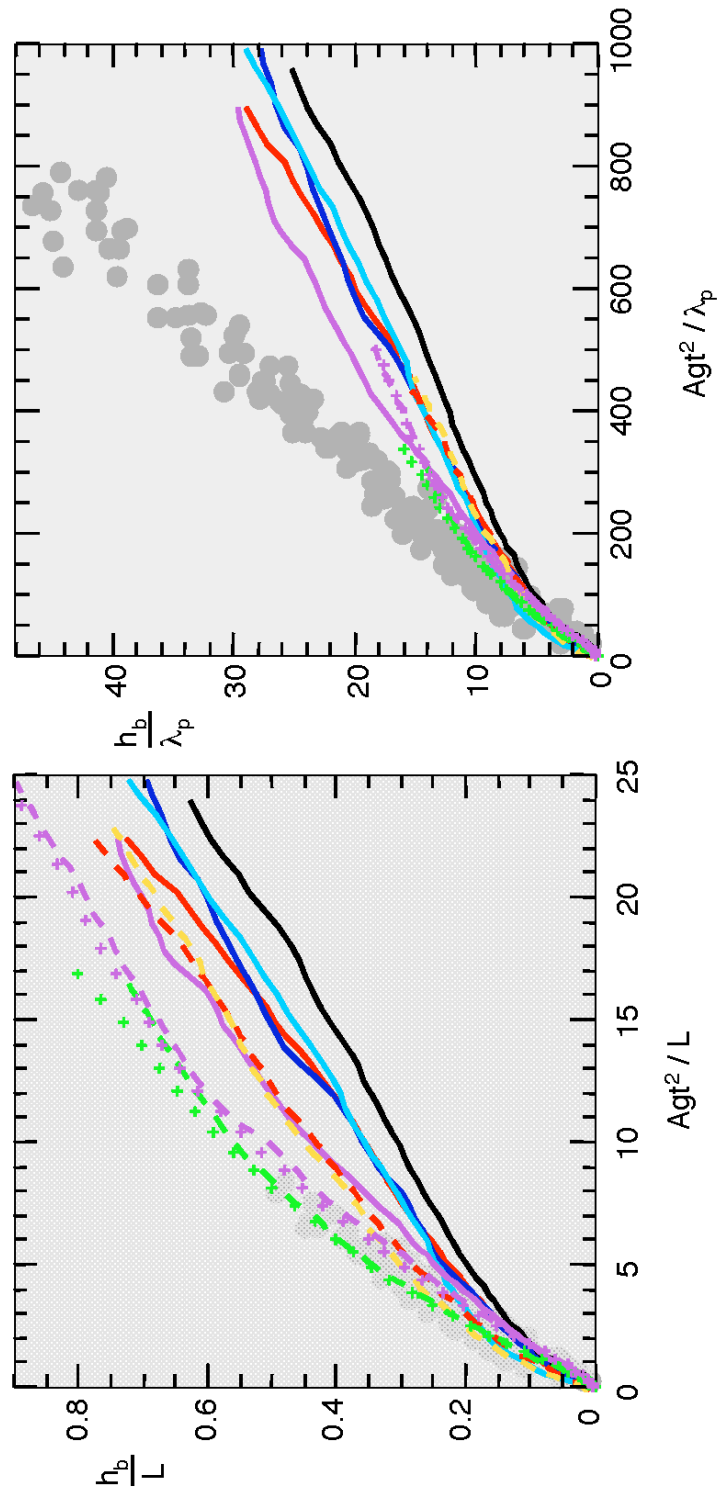


Figure C.2. Evolution of the bubble amplitude  $h_b$  from the numerical simulations as a function of (a)  $Agt^2$ , and (b)  $Agt^2/\lambda_p$ .

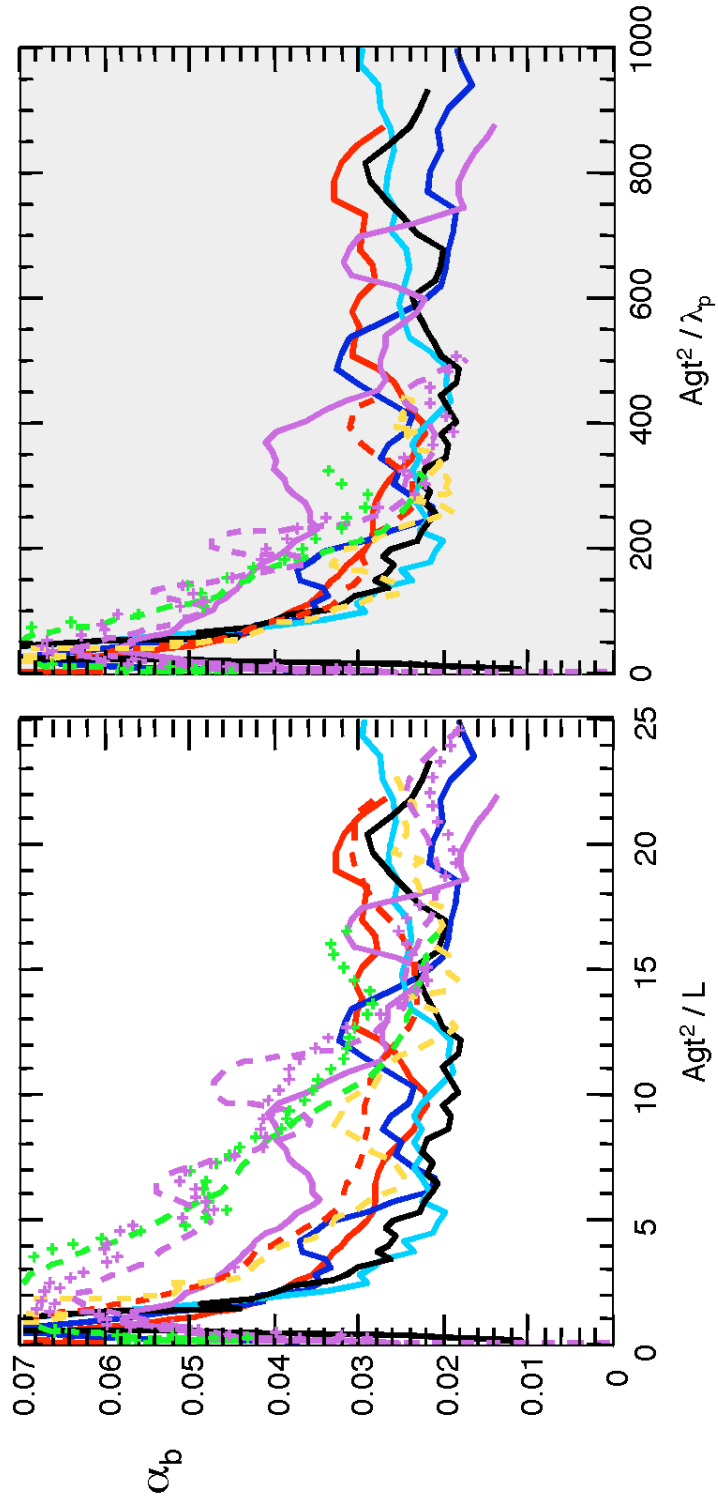


Figure C.3. Evolution of the growth constant  $\alpha_b$  from the numerical simulations as a function of (a)  $Agt^2$ , and (b)  $Agt^2/\lambda_p$ .

R-T Code	Growth constant $\alpha_b$
TURMOIL 3D (256x256x512)	0.028
FLASH(256x256x512)	0.022
WP/PPM(256x256x512)	0.024
HYDRA(256x256x512) (without IR)	0.029
NAV/STK(256x256x512)	0.022
RTI-3D(128x128x256)	0.03
ALEGRA(128x128x256) (without IR)	0.024
HYDRA(128x128x256) (without IR)	0.024
ALEGRA(128x128x256) (with IR)	0.030
HYDRA(128x128x256) (with IR)	0.024

Table C.3. Bubble growth constant  $\alpha_b$  from the simulations.

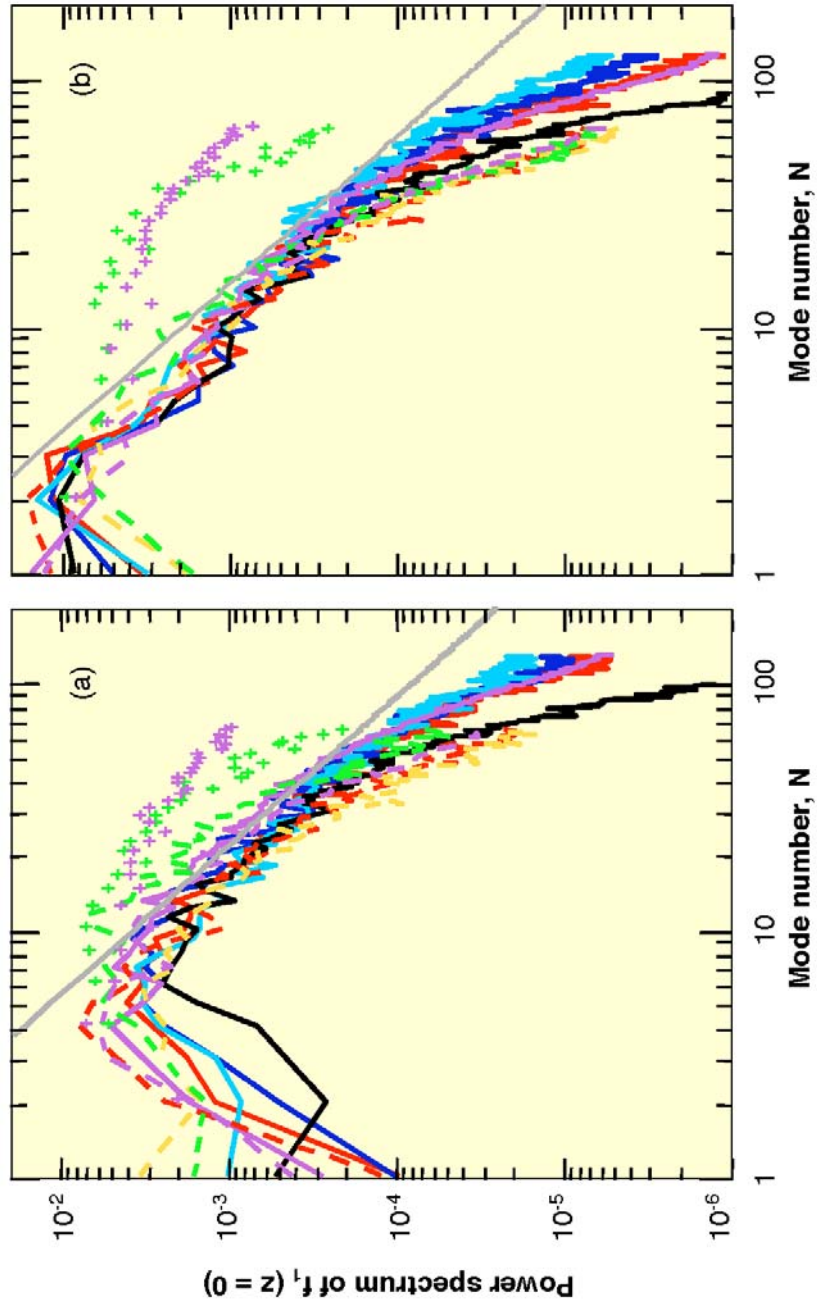


Figure C.4. Power spectra of density fluctuations from the numerical simulations at (a)  $Ag\tau^2 = 5$ , and (b)  $Ag\tau^2 = 22$ .

The azimuthally averaged density spectra were computed according to (6.5.1) for all the numerical simulations and are shown in figure C.4 (a) and (b) for  $A_i g t^2 / L = 5$  and 22 respectively. The solid gray line indicates the  $k^{-5/3}$  slope associated with an inertial range. Interestingly, the calculations with IR do not exhibit a significant inertial range. This could be due to the lack of dissipation in these calculations that would otherwise act as a sink for the kinetic energy produced by buoyancy. Therefore, as the flow evolves from (a) to (b), there is a visible filling in of energy at all scale due to the production term. The calculations without IR show a dissipative region seen here as the drop-off at high wavenumbers. The peak of the spectra shift from  $n = 4 - 10$  to  $n = 2 - 3$  at late time, consistent with the emergence of the large-scale structures.

## APPENDIX D

### DIMONTE'S MODEL FOR THE EFFECT OF INITIAL AMPLITUDES ON $\alpha_b$

#### *D.1 Model Formulation*

A synopsis of the model describing the role of initial conditions on  $\alpha_b$ , and  $\beta_b$  is provided here. A detailed description is provided in Dimonte (2003). In the linear regime, the R-T growth rate is given by  $\Gamma = \sqrt{A_r k g}$ . In the presence of viscosity, this is modified to give (5.2.2). Thus, the exponential growth of bubble amplitude of a wavenumber  $k$  is (Chandrasekhar 1961)

$$h_k = h_{0k} \cosh(\sqrt{A_r k g t}), \quad (\text{D.1.1})$$

where  $h_{0k}$  is the initial amplitude of wavenumber  $k$ . The transition to nonlinearity occurs when

$$k h_k \sim 1, \quad (\text{D.1.2})$$

with the linear velocity  $\sim \Gamma h_k$  approaching the nonlinear velocity  $\sim \sqrt{A_r g/k}$  - this is referred to as the Fermi transition (Layzer 1955). Haan (1989) considered the interaction of neighboring modes of similar phases that can interfere constructively, triggering transition much earlier. In this scenario, the modes in a wavepacket of width  $\delta k$  transition when their r.m.s. amplitude

$$\langle h_k \rangle = \left( \frac{L^2}{2\pi} \int_{k-\delta k}^{k+\delta k} h_k^2 k' dk' \right)^{1/2} \quad (\text{D.1.3})$$



exceeds the nonlinear threshold. Dimonte (2003) defines the width of the wavepacket  $\delta k \sim \frac{3}{8}k$ , where  $k$  is the central wavenumber of a wavepacket. In this picture, the central wavenumber is the bubble wavenumber  $k_b$ , and the width of the wavepacket is  $\delta k = \frac{k_b - k_s}{2}$ , where  $k_s$  is the wavenumber of the mode that has just reached its saturation amplitude. An  $e^{-2}$  distribution is assumed for the energy distribution of the wavepacket with the peak at  $k_b$ . Thus for 2D perturbations, transition occurs before the individual modal amplitudes are large enough to satisfy (D.1.2) (Haan 1989). We can represent a wavepacket by its central wavenumber, since for  $k \gg \delta k$ , all the modes in a wavepacket have similar  $k$ . If we take  $h_b$  to be the leading bubble amplitude (i.e. the central mode), then the variance of amplitudes range from 0 to  $h_b^2$ , and the mean of these fluctuations is  $\langle h_k \rangle^2 \sim h_b^2 / 2$  (Haan 1989). Then, applying the Fermi transition ( $\Gamma h_b = Fr \sqrt{\pi A_t g / k_b}$ ) to the bubble in a wavepacket, we get

$$k \langle h_k \rangle \sim Fr \sqrt{\pi / 2}. \quad (\text{D.1.4})$$

The evolution of  $\langle h_k \rangle$  in the nonlinear regime can be written as

$$\langle h_k \rangle = \frac{Fr}{k} \sqrt{\frac{\pi}{2}} + Fr \sqrt{\frac{A_t g \pi}{2k}} (t - t_k), \quad (\text{D.1.5})$$

where  $t_k$  is the time at which transition occurs. Here,  $t_k$  is obtained by inverting (D.1.1) and using (D.1.4):

$$t_k \sim \frac{1}{\sqrt{A_t k g}} \cosh^{-1} \left[ \frac{Fr \sqrt{\pi / 2}}{k \langle h_{0k} \rangle} \right]. \quad (\text{D.1.6})$$

Thus, the self-similar bubble amplitude has been expressed as a function of the initial r.m.s. amplitude  $\langle h_{0k} \rangle$  and the Froude number  $Fr$ . Combining (D.1.6) with (1.2.1), and the definition for  $\beta_b$ , we get two equations describing the dependence of  $\alpha_b$  and  $\beta_b$  on  $k\langle h_{0k} \rangle$ :

$$\alpha_b = \frac{Fr\sqrt{\pi}}{4} \left[ \cosh^{-1} \left( \frac{Fr\sqrt{\pi/2}}{k\langle h_{0k} \rangle} \right) - 1 \right]^{-1} \quad (\text{D.1.7})$$

$$\beta_b = \frac{2\sqrt{\pi}}{Fr} \left[ \cosh^{-1} \left( \frac{Fr\sqrt{\pi/2}}{k\langle h_{0k} \rangle} \right) - 1 \right]^{-1} \quad (\text{D.1.8})$$

Note that in the derivation of the above equations,  $\alpha_b$  and  $\beta_b$  are coupled through

$$\alpha_b = \frac{Fr^2}{8} \beta_b. \quad (\text{D.1.9})$$

Thus according to this model, both  $\alpha_b$  and  $\beta_b$  depend logarithmically on  $k\langle h_{0k} \rangle$  (qualitatively similar to Birkhoff's model (1955)). For self-similarity (constant  $\alpha_b$  and  $\beta_b$ ), (D.1.3), (D.1.7), and (D.1.8) require that  $h_k \sim k^{-2}$ .

## APPENDIX E

### A TWO-FLUID FORMULATION FOR THE TRANSPORT OF ENSTROPY

#### *E.1 Formulation of Two-fluid Vorticity Measure*

In this section, a molecular mix fraction for enstrophy is defined in a manner analogous to (and consistent with) the definition for thermal fluctuations in a 2-phase fluid (section 3.2). Let  $\omega(y,t)$  represent the vorticity at a location  $y$  across the mix, and at time  $t$ . We define the enstrophy volume fractions as

$$f_{1,\omega} = \frac{N}{N+M}, \quad f_{2,\omega} = \frac{M}{N+M}, \quad (\text{E.1.1})$$

where  $N$  and  $M$  are the number of counts of rotational and irrotational fluid respectively (thus  $1 \rightarrow$  rotational fluid,  $2 \rightarrow$  irrotational fluid). The 2-fluid measure for enstrophy defined similar to  $B_2$  for thermal fluctuations, is

$$\Omega_2 = \left( \sum_1^N (|\omega_1| - \overline{|\omega|})^2 + \sum_1^M (|\omega_2| - \overline{|\omega|})^2 \right) / (M+N). \quad (\text{E.1.2})$$

$|\omega_2| \neq 0$ , giving  $\Omega_2 = \left( \sum_1^N (|\omega_1| - \overline{|\omega|})^2 + \sum_1^M (\overline{|\omega|})^2 \right) / (M+N)$ . Simplifying (E.1.2)

using (E.1.1), and  $f_{1,\omega} + f_{2,\omega} = 1$ , we get

$$\Omega_2 = \overline{|\omega|} \left( |\omega_1| - \overline{|\omega|} \right). \quad (\text{E.1.3})$$

In the above,  $|\omega_1|$  and  $|\omega_2|$  are the maximum and minimum enstrophies in the flow.  $|\omega_1|$ , the maximum value can be expected to occur along the centerline of the mix, and can be determined from the measured values here. However, experimental measures of

the intermittency factor based on a vorticity threshold reveal a value of 0.5 at the centerline that implies that both rotational and irrotational fluid occur in equal probability there (see figure 4.3 (a)).

Thus, the volume fractions defined above will have to take values of 0.5 at the centerline. Then, the average enstrophy at the centerline is

$$\overline{|\omega|} = f_{1,\omega} |\omega_1| + f_{2,\omega} |\omega_2|. \quad (\text{E.1.4})$$

Since  $|\omega_2| = 0$ , and  $f_{1,\omega} = f_{2,\omega} = 0.5$  at the centerline,

$$|\omega_1| = 2\overline{|\omega_{centerline}|}. \quad (\text{E.1.5})$$

The advantage of using  $2\overline{|\omega|}$  over  $|\omega_1|$  in (E.1.3) is that there is lesser uncertainty in measuring the average enstrophy value than the maximum value at a point. Now to compare with molecular mix of thermal fluctuations,  $\frac{\Omega_2}{\Delta\omega^2}$  will have to take a value of 0.25 at the centerline. This is demonstrated below.

The non-dimensional two-fluid enstrophy fluctuation is given by

$$\frac{\Omega_2}{\Delta\omega^2} = \overline{|\omega|} \frac{2\overline{|\omega_{centerline}|} - \overline{|\omega|}}{4\overline{|\omega_{centerline}|}^2}, \quad (\text{E.1.6})$$

where we take  $\Delta\omega = |\omega_1| = 2\overline{|\omega_{centerline}|}$ . Using  $f_{1,\omega} = \overline{|\omega|} / 2\overline{|\omega_{centerline}|}$ , (E.1.6) then

reduces to

$$\frac{\Omega_2}{\Delta\omega^2} = f_{1,\omega} f_{2,\omega}. \quad (\text{E.1.7})$$

Unlike volume fractions of fluids of different densities,  $f_I$  never reaches a value of one anywhere in the flow, since even at the centerline both irrotational and rotational fluids are present. This is in contrast to shear flows such as jets, where after an initial region where a potential core may be present, there is always vorticity along the centerline.

The turbulent enstrophy fluctuations  $\overline{\Omega_0'^2}$  can be defined, in a manner similar to  $\overline{\rho_0'^2}$ .

Thus,

$$\overline{\Omega_0'^2} = \sum_I^{N+M} (\omega_I / -|\overline{\omega}|)^2 / (N + M), \quad (\text{E.1.8})$$

and the molecular mix of enstrophy will be given by

$$\theta_\omega = 1 - \frac{\overline{\Omega_0'^2}}{\overline{\Omega_2'^2}}. \quad (\text{E.1.9})$$

$\theta_\omega$  computed from experimental vorticity data approaches 0.3, much lesser than the molecular mix values for density fluctuations reported earlier in this work. Given the higher diffusivity of velocity/vorticity fluctuations, one would expect a greater value for  $\theta_\omega$ . The lower values for  $\theta_\omega$  could be due to our choice of the threshold for  $|\omega_I| = 2|\overline{\omega}|$ . For instance, using a threshold value of  $|\omega_I| = 3|\overline{\omega}|$  gave higher values of  $\theta_\omega \sim 0.6 - 0.7$ . Thus, the above model may have to be modified to accommodate this refined threshold value.

**VITA**

Name: Praveen Kumar Ramaprabhu

Date and place of birth: May 20, 1975  
Chennai, Tamil Nadu  
India

Permanent address: 7 Link Road, Kotturgardens  
Chennai, Tamil Nadu  
India 600085

Education: B.S. (Mechanical Engineering), May 1996  
Anna University, Chennai, India

M.S. (Mechanical Engineering), May 2000  
University of Houston, Houston, Texas

Ph.D. (Mechanical Engineering), December 2003  
Texas A&M University, College Station, Texas